ANNUAL REPORT 2015

CENTER FOR EXPERIMENTAL NUCLEAR PHYSICS AND ASTROPHYSICS

UNIVERSITY OF WASHINGTON

CENPA

Center for Experimental Nuclear Physics and Astrophysics

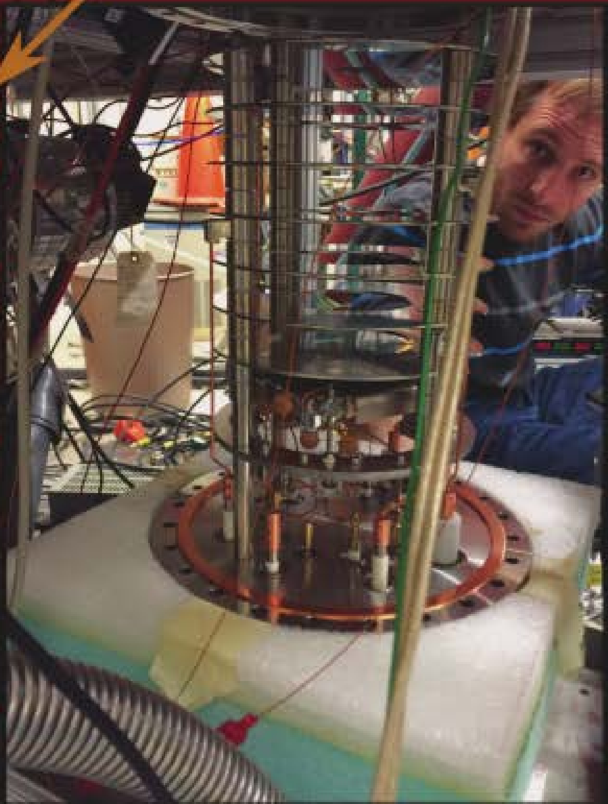

Annual Report 2015

University of Washington

ANNUAL REPORT

Center for Experimental Nuclear Physics and Astrophysics
University of Washington
April, 2015

Sponsored in part by the United States Department of Energy
under Grant #DE-FG02-97ER41020.

Cover design by Gary Holman. The background design on the front and back cover is a rendering of a $g-2$ silicon photo-multiplier (SiPM) (Sec. 4.7). In the top left photo, Arnaud Leredde inspects part of the detection system for the ^{6}He experiment (Sec. 3.1). The top right photo depicts graduate student John Lee repairing the apparatus for the short range spin-coupled force experiment (Sec. 2.5). In the bottom left photo, graduate student Rachel Ryan is assembling the MuSun time-projection chamber in preparation of the 2014 data run at the Paul Scherrer Institute (Sec. 4.20). In the bottom right photo, postdoc Luiz de Viveiros (UC Santa Barbara) working on the Project 8 (Sec. 1.8) superconducting magnet in the basement of the UW Physics-Astronomy Building.

INTRODUCTION

The Center for Experimental Nuclear Physics and Astrophysics, CENPA, was established in 1998 at the University of Washington as the institutional home for a broad program of research in nuclear physics and related fields. Research activities are conducted locally and at remote sites. The research program emphasis is fundamental symmetries and neutrinos. In neutrino physics, CENPA is the lead US institution in the KATRIN tritium beta decay experiment, the site for experimental work on Project 8, and a collaborating institution in the MAJORANA ^{76}Ge and the SNO+ ^{130}Te double beta decay experiments. The Muon Physics group is running the MuSun experiment to measure muon capture in deuterium at the Paul Scherrer Institute in Switzerland. The group has a leadership role in the new project to measure the anomalous magnetic moment of the muon at Fermilab to even higher precision than it is presently known from the collaboration's previous work at Brookhaven. The fundamental symmetries program also includes "in-house" research using the local tandem Van de Graaff accelerator with an experiment to measure the electron-neutrino correlation and Fierz interference in ^{6}He decay.

In addition to the research directly supported by DOE's Office of Nuclear Physics through the CENPA core grant, other important programs are located in CENPA, forming a broader intellectual center with valuable synergies. The 'Gravity' group, as it is known, carries out with both DOE and NSF support studies of the weak and strong Equivalence Principles, fundamental precepts of General Relativity, as well as searches for non-Newtonian weak forces such as are predicted by theories with extra dimensions. The DOE Office of High Energy Physics supports a unique experiment, the ADMX axion search, now in an extended data-taking phase. These unique CENPA activities have generated an unusual spinoff, a successful program on nanopore DNA sequencing, led by Jens Gundlach and supported by NIH.

The past year has marked another exciting one in accomplishment and recognition. Assistant Professor Jason Detwiler received the Physics Department Mentoring Award. Senior Research Scientist Erik Swanson received a Fermilab Intensity Frontier Fellowship, given to outstanding researchers in neutrino and muon physics. Todd Wagner successfully defended his thesis in December. Dmitry Lyapustin and Jared Kofron defended theirs, both on St. Patrick's day in 2015, and we congratulate them all.

Postdoctoral Fellow Diana Parno was appointed Acting Assistant Professor and Associate Director of CENPA, and has in a few short months made many improvements as well as taking on much of the day-to-day operation of CENPA. Diana takes over from Associate Director and technical guru Greg Harper, who retired in August, but lives in Seattle and has not disconnected his phone. Nomie Torres joined us in December from the University of Alaska in Fairbanks. Nomie is a Fiscal Specialist 2 with our Administrator Victoria Clarkson in the front office, and has contributed greatly to the operations side of CENPA. Hannah LeTourneau signed on in August as a Research Engineer to manage the new ADMX helium liquefier.

It has also been a time of transition. Tom Trainor retired in December and is now Research Professor Emeritus. This brings to a close our long and noteworthy program on relativistic heavy-ion physics. Assistant Professor Nikolai Tolich resigned his position this year and

Postdoctoral Fellow Joulien Tatar, who joined us in March 2014 to work on SNO+ with Nikolai, is now at UC Berkeley pursuing his outstanding research on Cherenkov radiation from ice in Antarctica. Muon group postdoc Jason Crnkovic departed in April and Pete Alonzi departed in September. Jason is a Research Associate at Brookhaven, and Pete is now Senior Research Data Scientist in the University of Virginia Library System. ADMX group postdoc Michael Hotz departed in December to join Nion, Inc., and Andrew Wagner departed in January for Raytheon, Inc.

Ana Malagon arrived in September to join the ADMX Group as a postdoc. In March, 2015, Kim Siang Khaw arrived to join the Muon Group as a postdoc. Kim Siang follows in the footsteps of Andreas Knecht and Martin Fertl, the third graduate of Klaus Kirch's group at ETH to come to CENPA continuing a wonderful 'pipeline' of exceptional physicists for us.

Our aging buildings decided they weren't going to take it anymore and showered much of the Gravity Group's electronics with rainwater on two stormy weekends. This was evidently collateral damage from a seemingly endless University re-roofing project that turned CENPA into a construction zone for a year. A steam line (fortunately low pressure) blew on a Tuesday evening turning much of the Cyclotron wing into a steam bath, soaking carpets, walls, keyboards, and papers with warm sticky water. Old PCB-filled 2400-volt transformers were extracted in a carefully choreographed super-crane operation that required several one-day shutdowns of electrical power. The State of Washington required significant upgrades to our pressurized gas storage for the tandem, to meet new regulations. Our unflappable and capable Senior Engineer Doug Will led us through this gauntlet with his good humor.

In September, DOE convened a review panel to come to Seattle and review the CENPA proposal for the next 3-year renewal. The review went well, and the DOE Office of Nuclear Physics renewed our grant DE-FG02-97ER41020 for FY15-17. The continued support of CENPA by the Office of Nuclear Physics is greatly appreciated.

In the following we record some of the highlights of our past year in research.

- Construction and commissioning continues apace for the KATRIN neutrino mass experiment. The detector system, in conjunction with the suite of analysis tools, successfully completed a 135-day spectrometer commissioning campaign. The arrival of the tritium source and beam-line components in 2015 will further exercise the detector system as tritium operations approach in late 2016.

- Following the first round of extensive KATRIN Detector-Spectrometer commissioning measurements in 2013, the second round of measurements was carried out from October 2014 to March 2015, with improved detector alignment, an upgraded electron gun with pitch-angle control, fully functional Rn-trapping baffles, newly implemented active background removal methods using magnetic pulses and electric-dipole pulses, and a new detector wafer with 100% working pixels. This time the backgrounds from cosmogenic secondaries and stored electrons from Rn decays were fully understood and also confirmed to be under control, which allowed the collaboration to learn of new background source(s). The data are currently being analyzed extensively to plan the next round of measurements.

- The KATRIN data-analysis tools provided by the UW group were used for the second-round measurements as KATRIN's standard analysis platform. The tools were designed to be universal for offline, real-time and near-time analyses, and owing to that, a number of sophisticated offline analysis programs developed after the first-round measurements were used for the second round in the real-time and near-time regimes, providing immediate feedback for measurement planning. The tools were extended for simulation-driven analysis in order to facilitate *scenario* testing on measured phenomena.

- In July the Department of Energy, Office of Nuclear Physics undertook a comprehensive assessment of the KATRIN project's plans. The five-member external peer panel found the physics to be compelling and construction progress impressive but that the path to tritium will be challenging.

- A long paper on the tritium molecular final states by Laura Bodine, Diana Parno, and Hamish Robertson is published in Phys. Rev. C as an Editors' Suggestion. The paper describing the KATRIN detector system was completed under the leadership of Diana Parno and published in NIM.

- Project 8, an experiment that uses cyclotron radiation emitted by mildly relativistic electrons spiraling in a magnetic field to measure their energy, successfully demonstrated the principle of the method in June 2014, and is now moving toward a micro-scale tritium experiment. The paper reporting the success is in press in Phys. Rev. Lett. as an Editors' Highlight.

- The Majorana Demonstrator neutrinoless double-beta decay experiment commissioned and took data with a prototype array of natural HPGe detectors and began commissioning the first module of enriched germanium detectors. UW personnel participated in detector construction activities and are leading the data analysis effort. First results are expected in 2016.

- The g-2 Storage Ring has been rebuilt in its newly constructed custom building on the Fermilab campus. It is expected to be cooled down and powered on in May, 2015. The field shimming operation commences soon afterwards, with new NMR probes, electronics, and data acquisition provided by the UW team.

- The g-2 calorimeter development continues to progress on track. More than 1300 PbF_2 crystals and silicon photomultipliers have been ordered. This follows a highly successful SLAC test-beam run, which proved the technical concept of a prototype detector. The results are published in NIM.

- The MuSun experiment at PSI has completed 40% of its data taking on muon capture on the deuteron. The new UW-designed TPC and its critical electronics worked flawlessly, permitting the efficient collection of a very high-quality data set in 2014. Two papers about muon capture on the proton (MuCap experiment) and another about the MuSun cryogenic preamplifiers developed at UW are published.

- A new torsion-balance/rotating-attractor instrument with 20-pole magnet test-bodies has achieved attoNewton-meter sensitivity to the spin-dependent interactions mediated by Goldstone boson exchange with masses up to 0.1 meV. The null result is sensitive to new hidden symmetries broken at energy scales up to 100 TeV, about 5 times higher than the best prior constraint from the ALPS experiment at DESY.

- ADMX received the nod from DOE, following a very positive recommendation from the P5 Panel, to go ahead with the 'Gen-2' version of the experiment. ADMX will explore higher frequencies and do it much faster thanks to low-noise SQUID electronics cooled with a new dilution refrigerator.

- The relativistic heavy-ion group found that the *nonjet* cylindrical quadrupole component of 2D angular correlations from high-energy heavy ion collisions, conventionally measured by parameter v_2 and interpreted to represent elliptic flow of a quark-gluon plasma or "perfect liquid," exhibits several characteristics incompatible with a hydrodynamic interpretation. We have extracted a quadrupole-source boost distribution and m_t spectrum that reveal the quadrupole source as an expanding thin shell with fixed boost (radial speed) value independent of the collision system and a cold spectrum quite different from that manifested by most final-state hadrons. We have also measured nonzero quadrupole amplitudes in 200 GeV p-p collisions increasing approximately as the cube of the charge multiplicity (whereas dijet production in p-p collisions increases as the square of the multiplicity). Those and other aspects of nonjet v_2 data suggest that the quadrupole component is a novel QCD phenomenon unrelated to hydrodynamic flows in a dense medium.

- We have continued to apply a two-component (soft + hard) model (TCM) of hadron production in high-energy nuclear collisions to data from the LHC. Previously we described hadron yields and mean-transverse momentum trends from several LHC collision systems accurately with a TCM featuring a strong dijet component. We have now accomplished the same for event-wise mean-p_t fluctuation data from the same systems. A dominant role for dijet production is clearly established, whereas Monte Carlo models relying on extensive particle rescattering (expected for thermalization and hydro phenomena) are falsified by the LHC data.

- Our setup for trapping ^{6}He and searching for tensor currents has come together and we have gotten our first data set. Over about 1 day of data taking yielded statistics for a determination of "little a" at the 4% level. We are still working on many improvements and expect to triple our trapping efficiency and get a determination to $\sim 1\%$ before the end of 2015.

- The project testing for the possibility of nonlocal signaling using interference-pattern switching with momentum entangled photons, which has been pursued since 2007, has concluded with a publication that identifies the mechanism within quantum mechanics that blocks such signals.

As always, we encourage outside applications for the use of our facilities. As a convenient reference for potential users, the table on the following page lists the capabilities of our accelerators. For further information, please contact Diana Parno, Associate Director (dparno@uw.edu) or Eric Smith, Research Engineer (esmith66@u.washington.edu), CENPA, Box 354290, University of Washington, Seattle, WA 98195; (206) 543 4080. Further information is also available on our web page: `http://www.npl.washington.edu`.

We close this introduction with a reminder that the articles in this report describe work in progress and are not to be regarded as publications nor to be quoted without permission of the authors. In each article the names of the investigators are listed alphabetically, with the primary author underlined in the case of multiple authors, to whom inquiries should be addressed.

Hamish Robertson, Director	Diana Parno, Associate Director, Editor
Gary Holman, Technical Editor	Victoria Clarkson, Assistant Editor

TANDEM VAN DE GRAAFF ACCELERATOR

Our tandem accelerator facility is centered around a High Voltage Engineering Corporation Model FN purchased in 1966 with NSF funds, with operation funded primarily by the U.S. Department of Energy. See W. G. Weitkamp and F. H. Schmidt, "The University of Washington Three Stage Van de Graaff Accelerator," *Nucl. Instrum. Methods* **122**, 65 (1974). The tandem was adapted in 1996 to an (optional) terminal ion source and a non-inclined tube #3, which enables the accelerator to produce high intensity beams of hydrogen and helium isotopes at energies from 100 keV to 7.5 MeV.

Some Available Energy Analyzed Beams

Ion	Max. Current (particle μA)	Max. Energy (MeV)	Ion Source
^{1}H or ^{2}H	50	18	DEIS or 860
^{3}He or ^{4}He	2	27	Double Charge-Exchange Source
^{3}He or ^{4}He	30	7.5	Tandem Terminal Source
^{6}Li or ^{7}Li	1	36	860
^{11}B	5	54	860
^{12}C or ^{13}C	10	63	860
*^{14}N	1	63	DEIS or 860
^{16}O or ^{18}O	10	72	DEIS or 860
F	10	72	DEIS or 860
*Ca	0.5	99	860
Ni	0.2	99	860
I	0.001	108	860

*Negative ion is the hydride, dihydride, or trihydride.

Several additional ion species are available including the following: Mg, Al, Si, P, S, Cl, Fe, Cu, Ge, Se, Br and Ag. Less common isotopes are generated from enriched material. We recently have been producing the positive ion beams of the noble gases He, Ne, Ar, and Kr at ion source energies from 10 keV to 100 keV for implantation, in particular the rare isotopes ^{21}Ne and ^{36}Ar. We have also produced a separated beam of 15-MeV ^{8}B at 6 particles/second.

Contents

1 Neutrino Research

KATRIN

1.1 KATRIN status and plans

J. F. Amsbaugh, J. Barrett*, A. Beglarian†, T. Bergmann†, L. I. Bodine, T. H. Burritt, P. J. Doe, S. Enomoto, J. A. Formaggio*, F. M. Fränkle†, F. Harms†, A. Kopmann†, E. L. Martin, A. Müller†, N. S. Oblath*, D. S. Parno, D. A. Peterson, L. Petzold†, A. W. P. Poon‡, R. G. H. Robertson, M. Steidl†, J. Schwarz†, D. Tcherniakhovski†, T. D. Van Wechel, K. J. Wierman§, J. F. Wilkerson§, and S. Wüstling†

The layout of the KATRIN hardware is given in Fig. 1.1-1. Following the formation of the KATRIN collaboration in 2001, the first hardware for the experiment, the prespectrometer, appeared in 2005. This proved to be a workhorse in understanding and refining the design features of the main spectrometer, which was delivered in 2006. In 2011 the US institutes supplied the Focal Plane Detector (FPD) system and the data acquisition software. These, in conjunction with the suite of near-time/real-time analysis tools, have proved vital to the commissioning of the main spectrometer and understanding of the background sources.

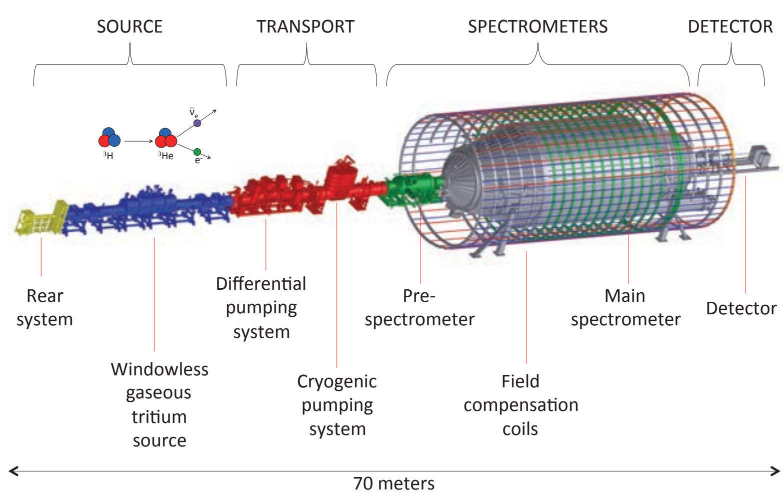

Figure 1.1-1. The layout of the main components of the KATRIN experiment.

The next two years will be exciting, but very challenging, times for KATRIN. The final components of the experiment, the Windowless Gaseous Tritium Source (WGTS), the Differential Pumping System (DPS) and the Cryogenic Pumping System (CPS), will all appear at KIT in 2015. These components must be installed, commissioned and integrated into the

*Massachusetts Institute of Technology, Cambridge, MA.
†Karlsruhe Institute of Technology, Karlsruhe, Germany.
‡Lawrence Berkeley National Laboratory, Berkeley, CA.
§University of North Carolina, Chapel Hill, NC.

Tritium Laboratory Karlsruhe (TLK) before tritium operation can begin as scheduled in late 2016.

Commissioning of this hardware will begin in early 2016 and will put great demands on the FPD system. A goal of the US institutes will be to ensure that the FPD system and the analysis tools are in optimal shape to meet the commissioning demands.

The status of this hardware and the plans for the FPD are outlined below, starting at the source and continuing down the beam line to the detector. Two additional UW-based activities are also overviewed, TRIMS and Time of Flight, both of which may impact future KATRIN activities.

- **Hardware and software status:**

  - *The tritium source:*

    At 2×10^{11} Bq, the WGTS is a sufficiently bright source to satisfy KATRIN's statistical requirements. In order to meet the systematic requirements, the tritium gas must be maintained at a well-defined and stable density. This is achieved by maintaining the source at 30 ± 0.01 K. These demanding conditions were successfully met in the WGTS demonstrator, a 10-meter-long by 90-mm-diameter tube whose temperature is maintained by boiling neon. Research Instruments Inc. is installing the demonstrator into the train of seven superconducting magnets necessary to constrain the electrons resulting from the tritium decay. The work is proceeding well and delivery to KIT is expected in August 2015.

    Preparation to receive this hardware is one of the major logistical challenges facing the KATRIN collaboration. The auxiliary systems include cryogenics supply/recovery lines, many hundreds of channels of slow controls instrumentation, and magnet safety systems. The installation is expected to be complete and commissioning to begin in late December 2015. The WGTS is expected to be operationally ready in May 2016.

    Monitoring the physical parameters of the WGTS is critical to the control and understanding of sources of systematic error. This is achieved in part by the Rear System that is attached to the upstream (rear) end of the WGTS and includes a steerable electron gun used to probe the gas column. This gun and associated vacuum assembly was delivered to KIT by UCSB in February 2015. The superconducting magnet that will link the Rear System to the WGTS passed its site acceptance tests in March 2015. The entire rear system is expected to achieve operational readiness in April 2016, in time for completing the commissioning of the WGTS.

  - *The transport system:*

    Once the electrons have been produced in the WGTS it is necessary to adiabatically transport them to the main spectrometer while at the same time excluding the tritium molecules from entering and contaminating the main spectrometer. This is a technical challenge, since the source is at a pressure of 10^{-3} mbar and the spectrometer is at a pressure of 10^{-11} mbar, and the two regions are connected by an open-ended beam pipe. The Differential Pumping System (DPS) and the Cryogenic Pumping System (CPS) provide the solution, together reducing the tritium level by a factor of 10^{14} while allowing the free passage of electrons.

The DPS consists of a chicane of five superconducting magnets separated by turbomolecular pumps. The chicane prevents line-of-sight passage of the neutral tritium molecules while the magnets guide the electrons through the chicane. The turbomolecular pumps return the tritium gas back to the source, resulting in a 10^7 tritium reduction factor at the output of the DPS. The original DPS was abandoned soon after delivery to KIT due to unresolvable problems with the magnet protection diodes. The system was subsequently redesigned using five, free-standing magnets. These magnets are installed on the support structure and have passed their site acceptance tests in March 2015. The chicane beam pipe and tritium secondary enclosure is nearing completion. Manufacture of the turbomolecular pump ports is complete and site acceptance testing of the beam tube assembly will be complete in July 2015.

The CPS traps the tritium molecules that escape the DPS. This system again consists of a chicane beam pipe, but instead of turbomolecular pumps, the tritium is captured on argon frost that lines the walls of the chicane, resulting in a further factor-of-10^7 reduction in the tritium entering the spectrometers. Between data-taking cycles the argon is sublimated and any captured tritium is removed.

The CPS is being built by ASG Superconductors in Genoa, Italy. Assembly is almost complete and delivery to KIT is expected in June 2015. After installation in the summer and commissioning with argon in the fall, the CPS will be ready for tritium in June 2016.

– *The spectrometers:*

The KATRIN experiment includes three spectrometers: the pre-spectrometer, used to reduce the flux of electrons entering the main spectrometer; the main spectrometer, where the electron energy is analyzed with a resolution of 0.94 eV; and the monitor spectrometer, used as an independent monitor of the spectrometer voltage stability.

The prespectrometer was used to guide the design of the internal electrodes of the main spectrometer and to understand sources of background. In mid-2015 it will be located in its final position at the entrance of the main spectrometer where it will reduce the flux of electrons by a factor of $\sim 10^7$, allowing only high-energy electrons to enter the main spectrometer.

The main spectrometer was delivered to KIT in 2006, and installation of the field-shaping and background-reducing inner wire electrodes was completed in 2013. The spectrometer has since undergone two $\sim$ 4-month commissioning periods, which have demonstrated that the spectrometer meets the design energy resolution. Unexpected sources of background have also been identified. ^{210}Pb from radon in the air is plated onto the wall of the spectrometer. This background may be reduced by use of the wire planes. An additional source of Rn is the 3 km of

NEG strips used to pump hydrogen emanating from the steel spectrometer walls. It has been demonstrated that the liquid-nitrogen-cooled baffles capture the Rn, effectively reducing the Rn entering the spectrometer to an insignificant amount. The background associated with the spectrometer is currently ~ 400 mHz, compared to the goal of 10 mHz. The dominant background is uniformly distributed throughout the volume of the spectrometer. It was measured during a commissioning run with a high residual gas pressure, since the spectrometer was not fully baked out beforehand. A brief data-taking run is scheduled for June 2015 to measure the background with a properly baked system.

The monitor spectrometer, consisting of the refurbished Mainz spectrometer, shares the same high-voltage retarding potential as the main spectrometer and, by monitoring the lines from a ^{83}Kr source, monitors the stability of the retarding potential of the main spectrometer. The monitor spectrometer is fully operational and ready for KATRIN tritium operation.

– *The detector system:*

The detector system passed its operational readiness review in March 2013 and has been used extensively for commissioning the spectrometer. Detector operation has revealed areas in which improvements can be made. An example is the replacement of the detector cosmic ray veto system that is currently underway (Sec. 1.3). The new veto is expected to provide excellent signal-to-noise and will be simple and robust, requiring little attention from the user. Installation and commissioning of the new veto is expected to be complete in September 2015. Another example is the development of wafer characterization methods for the focal-plane detector itself (Sec. 1.2).

In 2013 the pinch magnet began to fail, becoming unable to reach the nominal 6T field without quenching. The DOE and KIT rapidly responded by making funding available to secure a replacement pinch magnet. The new magnet was delivered to KIT in March 2015 and is currently undergoing site acceptance testing. The new pinch magnet incorporates many of the design features and lessons learned in the production of the DPS magnets and is expected to be robust and reliable. The detector system is expected to be fully operational by the time of the June background studies, and the final upgrades to the veto and electronics should be completed in time for the third round of commissioning in mid-2016.

– *Data acquisition and analysis tools:*

Data acquisition is controlled by the Object-oriented Real-time Acquisition and Control system (ORCA). This system is developed and maintained by UNC and is also used for the high-speed DAQ requirements of the monitor spectrometer and rear system. ORCA supports automation of data-taking sequences, enabling remote operation of routine activities such as calibration and repetitive data acquisition cycles.

In 2010 development began of a suite of real-time/near-time analysis tools[1]. Pri-

[1] CENPA Annual Report, University of Washington (2014) p. 5.

marily for use in commissioning the detector system, it includes tools to simulate and compare the detector performance. This has now evolved into the de facto analysis system for KATRIN (Sec. 1.4). Analysis routines are simply constructed by drag-and-drop from an extensive library of analysis tools, allowing the physicist to focus in the physics rather than the coding. Analysis routines can also be automated allowing a real-time check on the quality of the data. The system provides a robust foundation that may be built upon to accommodate the evolving needs of the KATRIN experiment.

– *Other activities:* In probing the neutrino mass, KATRIN examines the last 20 eV of the spectrum in order to avoid the electronic excited states of the T_2 decay. Within the 20 eV window there exist vibrational and rotational excited states which are thought to be calculable to the necessary precision (Sec. 1.5). However, there is significant disagreement between theory and experiment. At the UW, the Tritium Recoil Ion Measurement Spectrometer (TRIMS) will provide data that makes fundamental tests of the theoretical model, either supporting or refuting its use by KATRIN (Sec. 1.6).

  The spectrometer operates in the retarding-potential mode, integrating all events above the retarding potential of the spectrometer. The spectral shape is determined by operating the spectrometer at a number of different retarding potentials. It is also possible to operate the spectrometer in the Time-of-Flight (ToF) mode, in which the energies of all electrons above the retarding potential can be measured with a comparable resolution. Operating in the ToF mode will offer additional ways of suppressing backgrounds while drastically reducing the time to maximum neutrino mass sensitivity (Sec. 1.7).

• **Future plans:**

Exercising the detector system has provided insights into desirable improvements. As a result, upgrades are being implemented to the veto (Sec. 1.3) and electronics systems. The study of spectrometer backgrounds will be briefly revisited in June 2015 but the bulk of the commissioning activity will begin in mid-2016 when the source and transport systems are commissioned and brought online. By mid-2016, the detector system and its support team must be functioning like a well-oiled machine in order to meet the demands of commissioning and data-taking that will extended into 2021.

A new Memorandum of Understanding has been drawn up and approved by the DOE Office of Nuclear Science. The MoU runs until 2019, well into the tritium operations phase. The primary US responsibility remains the maintenance and operations oversight of the detector system. The detector system is complex and experience has taught us that a permanent on-site presence is required to maintain the knowledge base, ensure regular maintenance and respond to the unexpected. To this end we have identified a senior KIT scientist to fill the role.

Regular tritium operations will likely consist of three, three-month run periods, interspaced by one-month maintenance periods, per year. Since the experiment can be monitored and controlled remotely, the US institutes are positioned to remotely monitor data taking operations outside of the normal European working day. 24/7 operation of the tritium source requires a constant presence at the TLK. Support for the necessary staff is being sought by the KIT management.

The US institutes will continue to support the activities for which they are primarily responsible, namely the maintenance and development of the DAQ (UNC) and simulations software (MIT, UNC). The UW will continue to play a leading role in the maintenance, development and integration of the real-time analysis tools into the overall analysis framework.

A result from the TRIMS experiment is expected within a year and will be of interest outside the neutrino-mass community as well. Should the principle be proven for single-electron detection for ToF (Sec. 1.7), we will actively seek ways of incorporating it into the KATRIN experimental program to speed progress to the 200-meV neutrino mass sensitivity.

1.2 Wafer characterization and noise investigation

S. Enomoto, E. L. Martin, D. A. Peterson, R. G. H. Robertson, and T. D. Van Wechel

When a wafer from the 2014 batch of KATRIN focal plane detector wafers was installed as the KATRIN detector, the detector resolution went from 1.5 keV FWHM to 2.0 keV FWHM. Another wafer from the same batch was tested in an attempt to determine what might be the cause of the decreased performance. Three wafer properties were measured: inter-pixel resistance, sheet resistance, and bulk resistivity.

Each wafer is a PIN diode detector with a heavily doped entrance window to apply bias to each pixel, and a downstream readout side segmented into 148 pixels surrounded by a guard ring surrounded by a bias ring, each coated in titanium nitride. The bias-ring coating wraps around the edges of the wafer, connecting the upstream side of the wafer to bias.

Wafer inter-pixel resistance was measured by applying a fixed bias to a single pixel, and adjusting the bias on all surrounding pixels. The current on the single-pixel connection was measured. The measured current vs the inter-pixel voltage difference was fit to a model of two back-to-back diodes in parallel with an ohmic resistance and a fixed leakage current. The measured resistance was over 100 GΩ, too high to explain the noise. The measured leakage current was thought to be dominated by light leaks, yet still measured only 3.7 pA with a 100 V bias at -11 $^\circ$C, too low to explain the noise.

Sheet resistance was determined by applying a current on opposite pins of the guard ring or bias ring, and measuring the voltage on the other pins. The measurements were compared to a numerical model to determine the sheet resistance. For the bias ring the relative sheet resistance of the TiN-coated region and uncoated region was determined from the relative voltage distribution around the bias pins, and then the absolute sheet resistance was determined. The sheet resistance of the pixels was assumed to be the same as that of the guard ring.

The guard-ring sheet resistance for the new wafer measured 0.79 Ω/sq, compared to 48.7 Ω/sq for a wafer from the previous batch. The bias sheet resistance measured 4.0 Ω/sq for the TiN-coated region and 28.2 Ω/sq for the uncoated region, compared to 1580 Ω/sq and 35 Ω/sq for the wafer from the previous batch. The lower sheet resistance should result in less noise for the new wafer.

Bulk resistivity was measured by applying a forward bias to a pixel, and measuring the current. This was fit to a model of a diode in series with an ohmic resistance and the contribution from sheet resistance and pin contact resistance was accounted for. Bulk resistivity came out to 93 Ω·cm for the new wafer and 41 Ω·cm for the wafer from the previous batch. The higher bulk resistivity for the new wafer indicates lower impurity concentration, which would be expected to result in improved resolution.

As of yet no explanation for the reduction in detector resolution has been identified. All properties measured so far indicate the new wafer should actually be superior to the wafer from a previous batch. Further investigation is planned.

1.3 Progress on veto upgrade

T. H. Burritt, P. J. Doe, S. Enomoto, D. A. Peterson, and T. D. Van Wechel

The cosmic-muon veto for the detector wafer is being upgraded to take advantages of new silicon photomultiplier (SiPM) models and recent technical advancements developed by other experiments. The current KATRIN veto yields two to three detected photons per cosmic muon per SiPM, while other experiments typically report much higher numbers such as 20 detected photons per muon per SiPM, even with similar detector construction. Due to the high dark rate of SiPM's at ∼100 kHz, 99% of our recorded data is currently dominated by accidental coincidences of the dark noise, even with precise control of SiPM temperature with Peltier coolers in a box with carefully regulated dry nitrogen flow. An upgrade to a high light-yield system will not only reduce the data size by 99% but also will improve the robustness and stability of the system, ease operation, and reduce the systematic effects associated with the instability.

Cosmic-muon detectors of this type typically consist of plastic scintillator panels, wavelength-shifting (WLS) fibers inserted into the panels to collect photons and to bring them out of the panels, and SiPM photon detectors attached to the WLS fiber in some way. The scintillator panels are often wrapped with reflective material to improve photon collection efficiency. Sometimes SiPMs are attached to both ends of a WLS fiber, sometimes one end is treated to be reflective without a SiPM, and sometimes one end is just left unconnected and untreated, presumably due to the limited benefits of using both ends because of the short light attenuation length of the WLS fiber which is typically only a few meters.

After some literature review, the system developed by the T2K experiment seemed to have the best overall performance[1]. With considerable assistance from the T2K group, we utilized

[1] P.-A. Amaudruz et al., The T2K Fine-Grained Detectors, Nucl. Inst. Meth. **A 696**, 1 (2012).

the T2K SiPM holders to directly attach the SiPMs to the WLS fibers, which eliminate our lossy clear-fiber connections between the WLS fibers and SiPMs. The new Hamamatsu SiPMs (product name MPPC) with 1.3 mm $\times$ 1.3 mm sensitive area are used instead of our old 1.0 mm $\times$ 1.0 mm MPPCs. Also copying the T2K design, the WLS fibers are replaced with 1-mm-diameter Kuraray Y11 from Bicron BCF-91A. The scintillator panel thickness is doubled to 20 mm to further increase the photon yield.

With these improvements, the photon yield was expected to be large enough to allow the use of part of the "photon budget" to improve robustness, as done by T2K. The WLS fibers are replaceable if damaged (damage has already occurred to our current non-replaceable system) by making the fiber grooves sufficiently loose, the preamplifiers are placed away from the SiPMs using coaxial cables to an accessible location, and the SiPM coolers and associated dry nitrogen flow are all eliminated.

The readout electronics were redesigned and a prototype board was produced by CENPA. All the potentiometers are replaced with digital-to-analog converters (DAC) for full automated control. The bias supply circuitry was modified to reduce power consumption which is necessary for use without cooling fans under strong magnetic fields. A control board for DAC programming with temperature readout, based on a field-programmable gate array (FPGA), was designed and produced by CENPA. A set of software tools to operate the electronics was also developed.

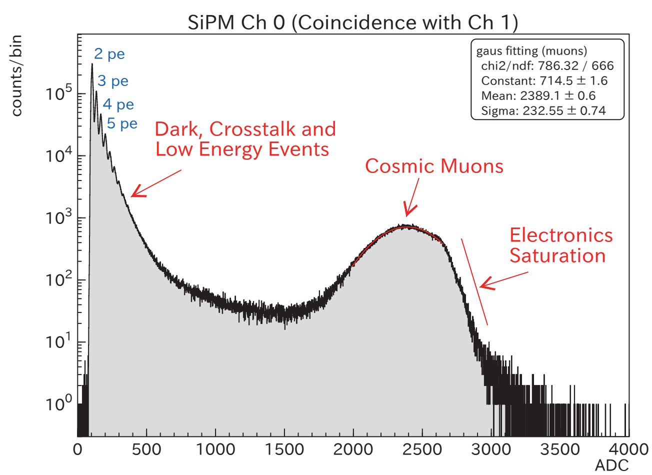

Figure 1.3-1. Performance of prototype veto system. The ADC scale is calibrated using the separated pe peaks at ADC $\sim$ 100, resulting in 32 ADC/photo-electron. The photon yield for cosmic muons is then calculated to be 75 photons per muon per SiPM. The electronics are saturated at the higher end of the muon peak (ADC $>\sim$ 2200) due to unexpectedly high light yield. The figure was created with the Koffein software tool (Sec. 1.4).

The performance of the new design was evaluated with a small test scintillator panel of 275 mm x 210 mm dimension. Fig. 1.3-1 shows measured photon yield with a test DAQ system using NIM trigger logic and VME readout, controlled with KiNOKO software. The acquired data is automatically processed and managed by KAFFEE (Sec. 1.4). Although the short WLS fiber length makes the photon yield higher than in the final design, the muon signals are far above the SiPM dark rate and crosstalk. The peak position is estimated to be ∼75 photons per muon per SiPM, which is to be compared with the current veto system light yield of 2 to 3 photons per muon per SiPM.

Based on this prototype test, two scintillator panels were produced and are currently being tested. The new veto will be installed on the detector system at KIT in September 2015.

1.4 Analysis tools: status and development plan

S. Enomoto

For the first round of commissioning measurements of the KATRIN Spectrometer - Detector Section (SDS) carried out in 2013, UW provided a suite of analysis tools which is based on the toolkit originally developed for the detector commissioning analysis in 2011-2012. The analysis tools were also used for the second round of SDS commissioning measurements (SDS-II) in 2014 with extensive improvements as described below:

The tools were originally developed for real-time and near-time applications, and were extended for used for offline analysis in the first round of the SDS commissioning measurements (SDS-I). Owing to the toolkit's feature of online and offline unification, the set of sophisticated offline analysis programs developed for SDS-I data after SDS-I concluded, were used for SDS-II real-time and near-time analyses without modifications, providing immediate final results during and/or just after every run.

For offline analysis use, the core tool for analysis logic (BEANS) was integrated with the KATRIN simulation tool, Kassiopeia. BEANS had been designed to be flexible for various analysis needs without having any pre-defined event data structure, and its dynamically-developing data model was found to be a good fit to the simulation's trait of attaching various pieces of information arbitrarily.

The analysis automation and run catalog tool (KAFFEE) was also extended for offline analysis and simulation. With a new MongoDB backend, KAFFEE maintains every analysis details as well as run conditions and simulation configurations, and enables to searches for specific runs and analysis results. In order to promote analysis sharing over remote locations, KAFFEE equips a convenient file uploader, Dripbox, allowing any files to be managed by KAFFEE. To facilitate interactive quick analysis on the data catalog, KAFFEE now contains a new web-based tool, Koffein, which can interactively draw histograms and graphs, read coordinates, count entries, compare histograms, fit any functions to histograms, and produce presentation-grade figures (see example in Fig. 1.3-1).

The UW-provided tools are now used as the defacto standard analysis tools for KATRIN SDS. It is expected that the tools will be further extended for use in the KATRIN Source and Transport Section (STS), where the data basically consists of time series of slow-control readings, very different from the event-based data from the detector system. Some extensive modifications to the tools are being investigated towards this end.

1.5 Molecular effects and the KATRIN experiment

L. I. Bodine, D. S. Parno, and R. G. H. Robertson

The ongoing construction of the Karlsruhe Tritium Neutrino experiment (KATRIN) has renewed interest in the molecular final-state distribution (FSD) populated by T_2 beta decay[1]. An understanding of the molecular effects at the percent level is necessary for KATRIN to reach the ultimate sensitivity of 0.2 eV. While modern calculations[2,3] claim accuracy on that level the interplay between experimental uncertainty and uncertainty on the theoretical FSD for KATRIN has largely been ignored. We re-examined the impact of molecular effects on KATRIN, quantifying the impact of molecular effects on KATRIN[4], as summarized below.

We showed that the general features of the FSD can be reproduced quantitatively from considerations of kinematics and zero-point motion, developing a semiclassical model of the molecule as a simple harmonic oscillator. The variance of the FSD arising from zero-point motion agrees well with the variances from the full quantum mechanical calculations. From this expression for the variances we were able to derive the impact on the systematic errors on the neutrino mass-squared. Table 1.5-1 shows the resulting systematic uncertainty on the neutrino mass-squared owing to the identified molecular effects.

Source of systematic shift	Target accuracy	$\sigma_{\rm syst}(m_\nu^2)[10^{-3}{\rm eV}^2]$
FSD theoretical calculations	$\lvert\Delta\sigma_{\rm FSD}/\sigma_{\rm FSD}\rvert \leqslant 1\%$	6
temperature calibration	$\lvert\Delta T/T\rvert \leqslant 0.005$	
- translational		0.05
- FSD		0.06
temperature fluctuations	$\lvert\Delta T/T\rvert \leqslant 0.001$	
- translational		0.009
- FSD		0.01
ortho-para ratio	$\lvert\Delta\lambda/\lambda\rvert \leqslant 0.03$	0.44
isotopic impurities		
- tritium purity	$\lvert\Delta\epsilon_{\rm T}/\epsilon_{\rm T}\rvert \leqslant 0.03$	2.9
- ratio of HT to DT	$\lvert\Delta\kappa/\kappa\rvert \leqslant 0.1$	0.03
higher rotational states	$\lvert\Delta T/T\rvert_{\rm rotational} \leqslant 0.1$	1

Table 1.5-1. Summary of molecular-related sources of systematic shift in extracted neutrino mass-squared, the projected accuracy on the experimental parameters and the individual effect on m_ν^2 for the nominal KATRIN parameters.

In addition to the impact on KATRIN we found that when the LANL and LLNL neutrino-mass experiments performed in the 1980s with gaseous tritium are re-evaluated using the modern FSD calculations[2], the extracted neutrino mass-squared values are consistent with

[1] E. W. Otten and C. Weinheimer, Rep. Prog. Phys. **71**, 086201 (2008).
[2] A. Saenz, S. Jonsell and P. Froelich, Phys. Rev. Lett. **84**, 242 (2000).
[3] N. Doss, J. Tennyson, A. Saenz and S. Jonsell, Phys. Rev. C **73**, 025502 (2006).
[4] L. I. Bodine, D. S Parno and R. G. H. Robertson, Phys. Rev. C **91** 035505 (2015).

zero instead of being significantly negative. This result highlights the importance of using the correct FSD to analyze molecular-tritium beta-decay neutrino-mass experiments.

Fig. 1.5-1 shows the FSD calculations of Saenz[1] compared to those of Fackler[2], which were available at the time of the original LANL and LLNL analyses.

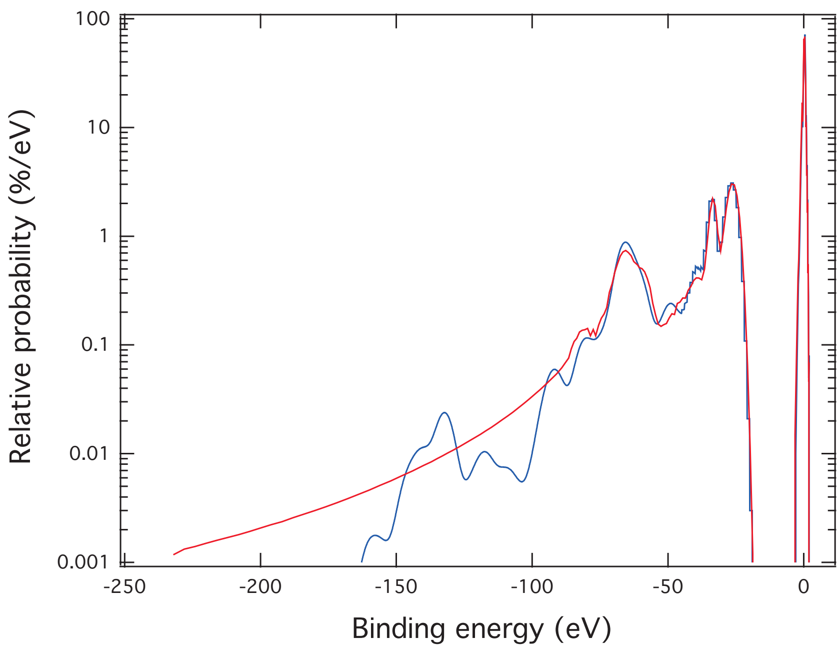

Figure 1.5-1. Molecular spectrum excited in the beta decay of T_2 ($J = 0$) as calculated by Saenz (solid red curve) and by Fackler *et al.*[2] (dotted blue curve). For the purposes of display and comparison, discrete states in the latter spectrum have been given a Gaussian profile with a standard deviation of 3 eV.

1.6 Update on the Tritium Recoil-Ion Mass Spectrometer

L. I. Bodine, T. Lin, D. S. Parno, and R. G. H. Robertson

The Tritium Recoil-Ion Mass Spectrometer, TRIMS[3], is an experiment designed to measure the probability that beta decay within a T_2 molecule will result in a bound $^3HeT^+$ molecule, testing an observable related to the molecular final-state distribution relevant to KATRIN (Sec. 1.5). The beta electron will be detected in coincidence with a $^3He^+$, T^+, or $^3HeT^+$ ion, using a pair of silicon detectors at either end of a glass decay chamber. The charged particles will be accelerated toward the detectors using a 60-kV potential difference, and will be guided by a 2-kG magnetic field. The experiment is presently under construction with the goal of commissioning in late spring and summer of 2015.

[1] A. Saenz, S. Jonsell and P. Froelich, Phys. Rev. Lett. **84**, 242 (2000).
[2] O. Fackler, B. Jeziorski, W. Kołos, H. J. Monkhorst and K. Szalewicz, Phys. Rev. Lett. **55**, 1388 (1985).
[3] CENPA Annual Report, University of Washington (2013) p. 15.

The assembly of the VCR and 2.75-inch CF portions of the ultra-high vacuum system, comprising the gas-handling, pressure-measurement, and pumping sections, is essentially complete. A partial redesign has been implemented to ensure electrical isolation between the front-end electronics and the vacuum gauges and pumps. Upgrades to the support structure, which will simplify the final installation of the decay chamber and the final positioning of the vacuum system relative to the magnets, are underway.

The beta detector will be held at 60 kV relative to the ion detector. In a test setup, the decay chamber, including detector blanks and the internal metal plates that will define the potential near the detectors, has been placed in the 2-kG magnetic field and successfully maintained at voltages up to 70 kV. The test has been performed both under a vacuum at 3×10^{-8} Torr and with injected H_2 gas at 1×10^{-7} Torr, which matches the anticipated T_2 pressure during eventual data-taking.

Data will be acquired with a 250-MS/s digitizer from CAEN, which has now been integrated with ORCA by Mark Howe at the University of North Carolina, Chapel Hill. We have written OrcaRoot code, including an offline trapezoidal filter, to translate the raw data into an analysis-ready format. Initial tests of the detectors, digitizer, and front-end electronics, using ^{241}Am calibration data, give a preliminary energy resolution of ~ 1.1 keV (σ). Once these tests are complete, the detectors and decay chamber will be installed on the main vacuum system.

Pumps, pressure gauges, and the high-voltage supply will be continuously monitored via a LabJack ADC read out by ORCA. We have tested this functionality and are working to integrate the readout with a PostgreSQL monitoring database.

A gaseous $^{83\mathrm{m}}$Kr source[1] has been produced at the CENPA tandem van de Graaff accelerator. The TRIMS apparatus will be commissioned with a measurement of the charge spectrum of the krypton ion following conversion. The resulting data may suggest modifications or upgrades before tritium data-taking commences. In preparation for the commissioning period, an upgraded simulation using Geant4 is in development.

1.7 Single-electron detection for KATRIN time-of-flight operation

E. L. Martin and R. G. H. Robertson

Implementing a time-of-flight capability in the KATRIN experiment could allow measurement of the energy spectrum above each retarding potential, instead of simply the rate of electrons above each retarding potential. This could significantly reduce the data collection time required to attain the same statistical uncertainty[2].

In time-of-flight mode the energy of each electron is determined from the time it takes to pass through the main spectrometer. As flight time is mostly determined by the slow

[1] CENPA Annual Report, University of Washington (2014) p. 13.

[2] N. Steinbrink, V.'Hannen, EL. Martin, R. G. H. Robertson, M. Zacher and C. Weinheimer, New J. Phys. **15**, 113020 (2013).

movement through the analyzing plane, where the remaining transverse momentum on the electron results in reduced energy resolution similar to high pass filter mode, the energy resolution in time-of-flight mode can be nearly as good as high-pass-filter mode. Energy resolution will be further reduced by timing resolution. The stop signal for time of flight is already available from the focal plane detector with around 100 ns timing resolution, but a start signal is still required. The best location for generating the start signal is between the pre-spectrometer and main spectrometer.

Electrons trapped between the main spectrometer and pre-spectrometer would cause a background in the tens of MHz. A removal method using a small rod inserted in the beam line has been proposed. Most electrons that pass the pre-spectrometer will be reflected by the main spectrometer and pass the tagger twice. This background can be reduced by using a higher pre-spectrometer retarding potential, but will still be in the range of tens of kHz. Time of flight is tens of μs, so random triggers are expected to be nearly as frequent as signal events. Even so, reduced measurement time is expected.

An electron tagger test setup using a resonant cavity is under construction. It uses a cylindrical cavity with a small hole through the center for electrons to pass through. A cylindrical cavity designed for the width of the KATRIN beam line would be too large to place between the pre-spectrometer and main spectrometer, so a different cavity with a helical design is also under development.

The cavity is excited by a loop inserted through the cavity wall, and excitation is measured from another loop. As an electron passes through it will exchange a small amount of energy with the cavity. How much depends on one cavity excitation amplitude and phase. A change in cavity excitation would indicate the passing of an electron, and how much it changed measures the change in electron energy.

The energy change of the electron is proportional to the cavity excitation voltage, but the energy stored in the cavity is proportional to the square of the excitation voltage. Excitation needs to be sufficient to overcome thermal noise, but not so large that the fractional change from a passing electron is too small. Based on component specifications the signal power is expected to be around 28 times the noise power for optimal excitation.

Project 8

1.8 Status of the Project 8 neutrino mass experiment

P. J. Doe, J. A. Formaggio[*], M. Fertl, D. Furse[*], M. A. Jones[†], J. Kofron,
B. H. LaRoque[‡], E. L. McBride, B. Monreal[‡], N. S. Oblath[*], R. Patterson[§],
R. G. H. Robertson, L. J Rosenberg, G. Rybka, M. G. Sternberg, J. Tedeschi[†], and
B. A. VanDevender[†]

Project 8 marked completion of phase 1 of its experimental effort with the publication of a highly resolved ^{83m}Kr conversion electron spectrum, shown below in Fig. 1.8-1, which includes conversion from the K, L, M, and N shells of krypton. This is the first demonstration of the technique, now called Cyclotron Radiation Emission Spectroscopy (CRES). CRES combines the rich history of single-electron trapping with high resolution-analysis techniques to provide a unique avenue to electron energy measurement and spectroscopy.

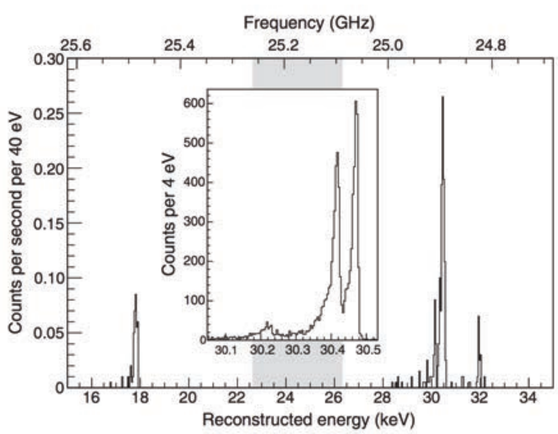

Figure 1.8-1. The conversion electron spectrum of ^{83m}Kr as measured by Project 8. The inset spectrum shows high resolution data from conversion of L shell electrons, with a characteristic FWHM of 15 eV.

With phase 1 completed, development efforts are ongoing for phase 2 of the prototype. In expectation of future challenges, initial designs for a version of the prototype experiment which contains tritium have been drawn. The fundamental difference in the design is an extended magnetic bottle formed from a pair of solenoidal coils. Small magnetic inhomogeneities can easily spoil such a confining potential, and therefore extensive magnetic surveying of the components of the prototype has been performed.

Data taking which is scheduled for later this year should probe both the design of the extended magnetic bottle as well as its performance, and lay the groundwork for a CRES measurement of the full β-decay spectrum of tritium.

[*]Massachusetts Institute of Technology, Cambridge, MA.
[†]Pacific Northwest National Laboratory, Richland, WA.
[‡]University of California Santa Barbara, Santa Barbara, CA.
[§]California Institute of Technology, Pasadena, CA.

Ho-163

1.9 Searching for neutrino mass with ^{163}Ho: spectrum shape

R. G. H. Robertson

In our search for new and more sensitive methods to measure the mass of the neutrino, we have given some consideration[1] to an idea that has its origins more than 30 years ago. It was noted that electron capture decay could be used to measure the mass because, although capture leaves a vacancy in an atomic orbital and ejects a nominally monoenergetic neutrino, in fact atomic vacancies have short lifetimes and therefore non-negligible widths. The decay process is then formally the same as a radiative decay,

$$^{A}Z \quad \rightarrow {}^{A}(Z-1) + \nu_e + \gamma_i + Q_i \tag{1}$$

with a 3-body phase space. The tails of the lines extend to the energy limit imposed by the ground-state Q-value, and at that limit are sensitive to the modification of phase space caused by neutrino mass. This method looks particularly attractive in the case of ^{163}Ho, which has a low Q-value in the vicinity of 2.5 keV. A number of experimental groups (ECHo, HoLMES, NuMECS) are developing high-resolution calorimeters to record the 'visible' energy, i.e. that not carried away by the neutrino. With such a detector, one observes sharp lines from the 7 occupied orbitals from which capture can occur: (3s), (3p1/2), (4s), (4p1/2), (5s), (5p1/2), and (6s). The lines have Breit-Wigner shapes extending to the energy cutoff at the Q-value, where neutrino mass information would be found. The determination of the mass requires knowledge of the spectral shape in the absence of neutrino mass, which can only be obtained from theory. Unfortunately the simplified theory just described neglects an important complication, the population of multivacancy states in the daughter ^{163}Dy atom. Fig. 1.9-1 shows the complex spectrum of satellite peaks that results. Their lineshapes are not Breit-Wigner and cannot easily be calculated, which makes the theoretical spectrum needed for extraction of neutrino mass problematic.

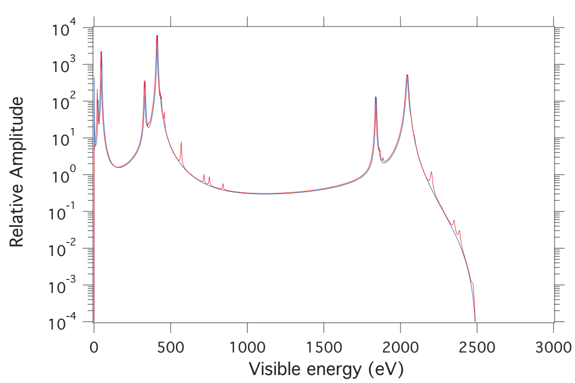

Figure 1.9-1. The visible energy in a calorimeter following electron capture in ^{163}Ho. The simpler spectrum (blue) is calculated in the customary single-vacancy approximation. The more complex spectrum (red) includes configurations with 2 vacancies.

[1] R. G. H. Robertson, Phys. Rev. C **91**, 035504 (2015).

SNO

1.10 Search for hep neutrinos in SNO data

T. J. Major and N. R. Tolich

The SNO experiment collected six years' worth of solar neutrino data. Most of the events were interactions of neutrinos originating from the decay of ^{8}B in the Sun, but a small fraction of the events correspond to events from the hep reaction, $^3\text{He} + p \rightarrow {}^4\text{He} + \nu + e^+$. Hep neutrinos are interesting because the hep reaction is less dependent on solar composition than are other fusion processes, and because calculation of the nuclear matrix element is prohibitively difficult. Determination of the rate of the hep reaction in the Sun would serve as a test of the Standard Solar Model in a new way. Hep neutrinos are distinguishable in principle from ^{8}B neutrinos because they have a different energy spectrum that extends to a higher energy regime than ^{8}B neutrinos.

To improve our knowledge of the rate of the hep reaction, we have developed a new event fitter that uses the spatial distribution of detected photons in addition to the time distribution. This fitter has improved the spatial resolution of event locations by around 10%. This fitter is also more reliable than previous methods at identifying a class of instrumental backgrounds that previously required a considerable fiducial volume cut.

Previous SNO analyses have used a rather conservative data set, but many runs that were excluded from this set may contain useful data. Some calibration runs that used a low-energy source may also contain useful higher-energy ^{8}B and hep neutrino events. We have developed a technique to test whether these runs contain data that are sufficiently similar to the conservative data set to be included in our analysis. Our technique uses a multi-dimensional modification of a Wald-Wolfowitz test, as discussed in Friedman and Rafsky[1]. We begin by treating each event as a vector in a phase space composed of energy and spatial distribution information. We then combine the test data set and the accepted data set, and calculate the Mahalanobis distance between every pair of events. From these distances, we construct a graph composed of the union of an appropriate number of minimum spanning trees. An analysis of the interconnectivity of this graph produces a p-value that can be interpreted as a measure of similarity between the data sets. In this way, we can systematically (and blindly) assess individual events, runs, and sets of runs to decide which data to add to our analysis.

[1] J. H. Friedman and L. C. Rafsky, Ann. Statist. **7**, 697 (1979).

Majorana

1.11 Overview of the Majorana Demonstrator

T. H. Burritt, M. Buuck, C. Cuesta, J. A. Detwiler, J. Gruszko, I. Guinn, J. Leon, A. Li, D. A. Peterson, R. G. H. Robertson, A. H. Thompson, and T. D. Van Wechel

The Majorana Demonstrator is a ∼40-kg array of high-purity germanium (HPGe) detectors enriched in ^{76}Ge that is under construction at the Sanford Underground Research Facility (SURF) in Lead, SD. The detectors are arranged in strings of 4-5 on low-background copper supports which are then placed in two cryogenic lead- and copper-shielded modules (see Fig. 1.11-1). The primary technical goal of the Demonstrator is the achievement of a radioactive background of 3.1 counts/ton/year within a 4-keV region of interest surrounding the 2039-keV Q-value for ^{76}Ge neutrinoless double-beta ($0\nu\beta\beta$) decay. Such a low background level would justify deeper investment in a much larger ton-scale experiment with sufficient sensitivity to definitively search for $0\nu\beta\beta$ decay for inverted hierarchical neutrino masses. In the process, the Demonstrator will simultaneously perform a sensitive test of a claimed observation of $0\nu\beta\beta$ decay[1], and will also perform searches for low-mass WIMP dark matter, solar axions, and other physics signals.

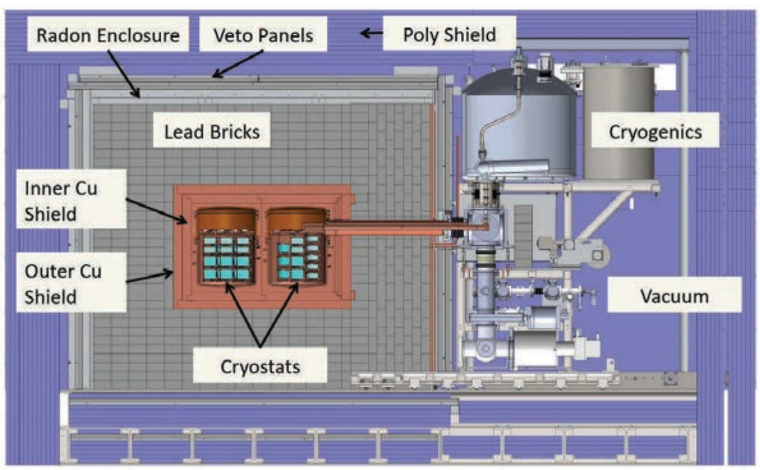

Figure 1.11-1. MAJORANA DEMONSTRATOR schematic.

The UW Majorana group leads the simulations and analysis effort within the collaboration, and contributes significantly to efforts in software development, data analysis techniques, background modeling, geometrical models for Monte Carlo simulations, data handling and storage issues, and feedback to design teams on background impact of proposed modifications. We are also responsible for the design, production, and testing of the low-mass signal cable connectors to be used in the experiment, and for the testing of the high-voltage (HV) feedthrough flanges and Picocoax® cables that deliver the bias voltage to the detectors. In addition to these responsibilities, our group at the University of Washington is also contributing to the ongoing construction efforts at SURF of the Majorana detector arrays.

[1] H. V. Klapdor-Kleingrothaus *et al.*, Phys. Lett. B **586**, 198 (2004).

1.12 String building for Module 1

T. H. Burritt, M. Buuck, C. Cuesta, J. A. Detwiler, J. Gruszko, I. Guinn, J. Leon, D. A. Peterson, R. G. H. Robertson, and T. D. Van Wechel

CENPA MAJORANA collaboration members have worked extensively building detector strings for the MAJORANA DEMONSTRATOR, contributing over 2000 on-site hours in the past year. The strings, which are tower assemblies holding four to five P-type point contact HPGe detectors and the low-mass front end boards that provide the first stage of signal amplification (seen in Fig. 1.12-1), are built entirely at the Sanford Underground Research Facility (SURF) Davis Campus on the 4850 ft. level. They are assembled in a class-10 glovebox to mitigate radon backgrounds, and then tested in individual string test cryostats. Following validation, they are installed in one of two electroformed copper cryostats, or the commercial copper prototype cryostat. Seven strings are installed into each of the modules that make up the MAJORANA DEMONSTRATOR.

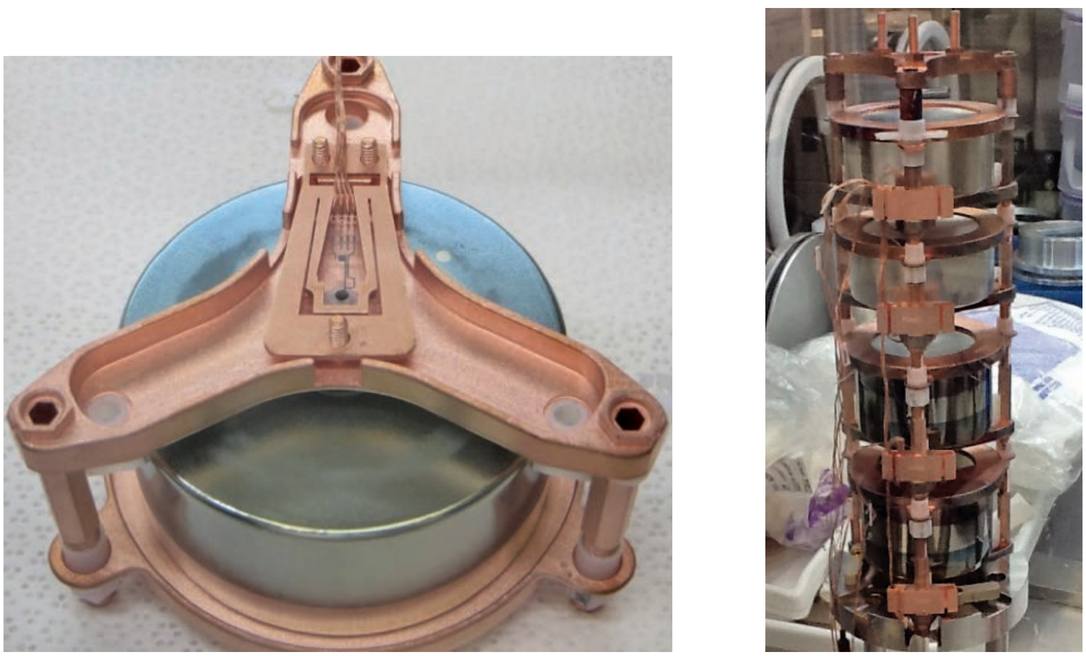

Figure 1.12-1. *Left:* The MAJORANA detector unit holds a P-type point contact HPGe detector and low-mass front end. *Right:* Detector assemblies are stacked to create a string.

Over the past year, the MAJORANA collaboration has reached many milestones in string and module operations. Following improvements to the prototype cryostat, which was used to develop the design and procedures needed for the MAJORANA DEMONSTRATOR, the prototype module was commissioned in May and June of 2014. Since July of 2014, it has been stably taking data with nine natural-abundance detectors. The veto system was integrated into its operation in September of 2014.

The procedures needed for the string-building of Module 1 were finalized via the construction of another natural-abundance detector string, and seven strings containing enriched detectors were built and tested for use in Module 1. This work continued over several months,

Figure 1.12-2. Seven strings are installed in each module of the MAJORANA DEMONSTRATOR.

during which CENPA members contributed to detector unit assembly, string assembly, and string characterization. After Cryostat 1 was commissioned, the 7 strings were installed, as in Fig. 1.12-2. Commissioning of the 29 detectors of Module 1 began in early April 2015, and will continue in the coming months.

1.13 High-voltage cable and feedthrough characterization

T. H. Burritt, M. Buuck, C. Cuesta, J. A. Detwiler, J. Gruszko, I. Guinn, J. Leon, A. Li, D. A. Peterson, R. G. H. Robertson, A. H. Thompson, and T. D. Van Wechel

The high-voltage (HV) cables and feedthrough flanges to be used at the MAJORANA DEMONSTRATOR have been characterized looking for micro-discharge events (MD) at the University of Washington. In total, 129 HV cables were tested: 42 for Module 1, 38 for Module 2 and 49 for the string test cryostats; and 280 HV feedthroughs since there are five 8" flanges with 40 feedthroughs each for Modules 1 and 2, and eight 6" flanges with 10 feedthroughs each for the string test cryostats.

First, the leakage current of the flange feedthroughs was measured up to 5 kV, which is the maximum operating voltage of the detectors. The feedthroughs failing this test, i.e. with leakage current >2 μA, were not further tested and used as ground at the MAJORANA DEMONSTRATOR. Then, each cable was tested with a feedthrough for at least 3 h, with an average time of 14 h. If a set did not pass the test, the cables were tested individually and the one creating MD events identified. The criteria that each cable and feedthrough have to fulfil to be accepted are: Holding 5 kV without current fluctuations, no excessive leakage current, and <5 MD/h.

The leakage current results are shown in Table 1.13-1, where it can be seen that 98% of the pins showed typical leakage current values at 5 kV. However, some pins were not recommended to be used at the MAJORANA DEMONSTRATOR as high-voltage.

Flange model	Total feedthroughs	High-leakage current feedthroughs	Average leakage current
6 inch	80	5	$1648 \pm 61\,\mathrm{nA}$
8 inch	200	2	$1653 \pm 57\,\mathrm{nA}$

Table 1.13-1. Leakage-current measurements results of the feedthroughs to be used at the MAJORANA DEMONSTRATOR.

The MD event rate per cable results are shown in Fig. 1.13-1. The rate should be considered as an upper limit since a contribution to the rate from the feedthrough or other parts of the electronic chain is expected. No issues were found for any of the cables, and a rate <5 MD/h was measured for all cables, with an average of 0.60 ± 0.11 MD/h. One feedthrough was found to create a rate >5 MD/h and was not recommended to be used at the MAJORANA DEMONSTRATOR as high-voltage.

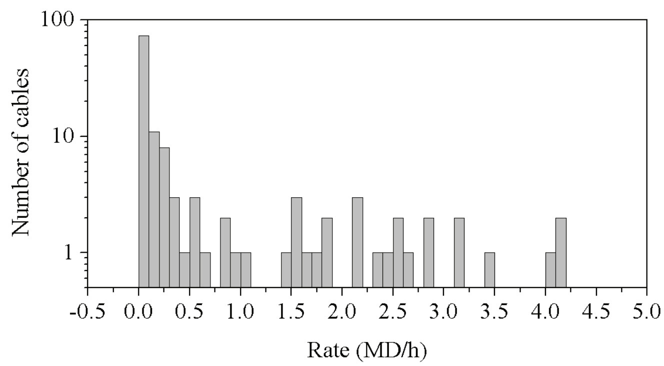

Figure 1.13-1. Micro discharge event rate per cable results for the cables to be used at the MAJORANA DEMONSTRATOR.

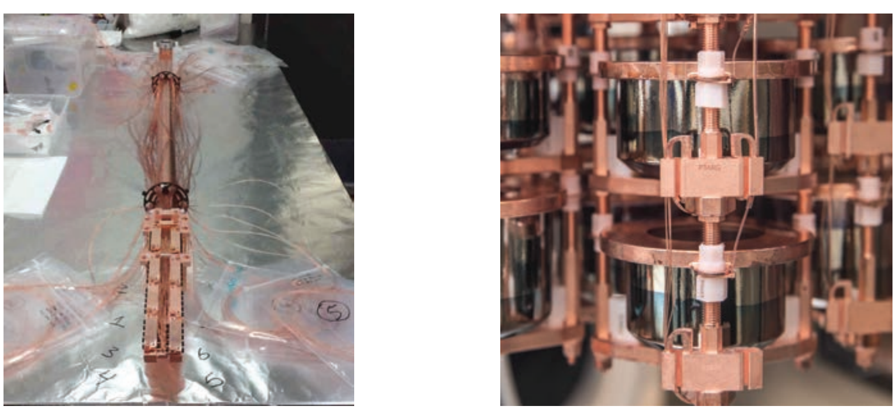

Figure 1.13-2. *Left:* Picture of the MAJORANA Module 1 cross-arm with the signal and high-voltage cables installed. *Right:* Picture of Module 1 already installed with a closer view of the detectors and cables.

The cables have already been installed in the string test cryostats and in Module 1. Fig. 1.13-2 shows the high-voltage and signal cables being installed into Module 1 and a close view of Module 1 with the cables and detectors installed.

1.14 Low-background signal connector production and testing

T. H. Burritt, M. Buuck, C. Cuesta, J. A. Detwiler, J. Gruszko, I. Guinn, J. Leon, A. Li, D. A. Peterson, R. G. H. Roberston, A. H. Thompson, and T. D. Van Wechel

In order to reach the background goal of <3 counts/ROI-ton-yr (ROI is the 4 keV region of interest around the Q-value of the $0\nu\beta\beta$), the Majorana Demonstrator requires low-background signal connectors. Each signal connector must connect the 4 coaxial cables that run between the front-end charge-collecting amplifier placed near the point contact of each detector to a feedthrough flange running out of the cryostat. The connectors are placed above the cold plate directly above the detector array. Commercially available connectors use electrical contact springs made out of beryllium copper alloy (BeCu), which is difficult to get with a low enough uranium and thorium content to meet the background goal. For this reason, UW has developed signal connectors for the experiment. These connectors must have a low mass and use low-activity materials. They must also be able to survive multiple cycles to vacuum pressure and liquid-nitrogen temperatures, and must be easy to manipulate inside a glovebox without breaking.

UW has developed a design consisting of electrical contact pins and sockets housed in Vespel® plugs, shown in Fig. 1.14-1. The connectors use gold-plated brass pins and sockets manufactured by Mill-Max®, with the BeCu contact springs removed. The pins and sockets are deliberately misaligned so that when plugged in, the pin is forced to bend against the socket. The spring force from this bending plays the role of the contact springs, providing reliable electrical continuity. The pins and sockets are attached to the signal cables using a low background Sn-Ag eutectic that was developed for the SNO experiment. Strain relief is provided by FEP heat shrink.

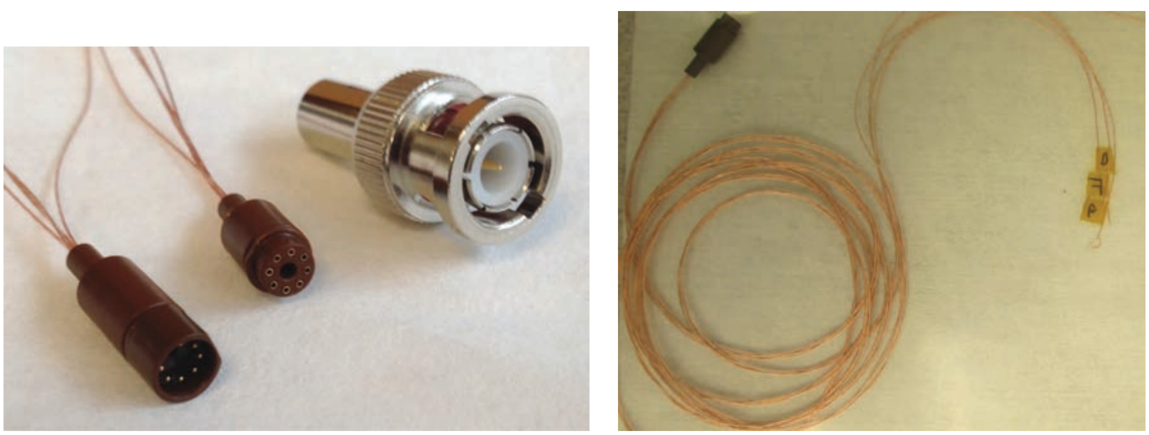

Figure 1.14-1. *Left:* A signal plug pair, with a BNC connector for comparison. *Right:* A signal cable soldered to a signal plug.

Production of signal plugs for the Majorana Demonstrator began in April 2014. The Vespel housing is machined at the 4850' level of SURF. The housing is then leached in nitric acid, sonicated in ethanol and deionized water, and pumped and baked. The pins are sonicated in ethanol and deionized water before being inserted into the housings underground. These plugs are then sent to UW to be soldered to signal cables in a clean room. Quality control (QC) tests are then performed to reject plugs that do not form reliable connections. The plugs are then sent to LBNL and SURF to be incorporated into the strings of detectors. So far, 159 female plugs and 109 male plugs have been produced. Of these, 112 females and 58 males have been soldered for use in Module 1 and the string test cryostats. Approximately 20-25% of plugs are rejected during the QC stage. In preparation for the production of signal plugs for Module 2, a batch of female plugs with different dimensions is being tested to improve on this figure.

Assays of the materials in the signal plugs and a full-body assay of 2 signal plugs have been performed to estimate the activity of the connectors. The assays were combined with the results of the background model to estimate the background contribution in the region of interest. Table 1.14-1 lists all background contributions. The results are consistent with a background dominated by the pins. Notice that the BeCu contact springs alone would surpass the MAJORANA DEMONSTRATOR's background goals by more than a factor of three. The current estimate for the contribution from signal connectors is 0.284 cts/ROI-t-yr.

Material	Assay Method	Mass [g per conn. pair]	Isotope	Activity [μBq/kg]	MJD BG [c/ROI/t/y]
Pins (w/BeCu)	ICP-MS	0.112	^{238}U	795000 ± 12000	8.8 ± 0.1
			^{232}Th	41000 ± 1000	2.3 ± 0.1
Pins (no BeCu)	ICP-MS	0.112	^{238}U	4600 ± 1500	0.05 ± 0.02
			^{232}Th	5800 ± 100	0.32 ± 0.01
Vespel SP-1	NAA	0.95	^{238}U	<1000	<0.20
			^{232}Th	<12	<0.01
Solder	GDMS	0.04	^{238}U	5600 ± 1000	0.02 ± 0.004
			^{232}Th	<12	<0.0002
Solder flux	GDMS	0.04	^{238}U	1200 ± 200	0.005 ± 0.001
			^{232}Th	<400	<0.007
FEP (shrink tube)	NAA	0.1	^{238}U	<1250	<0.012
			^{232}Th	<138	<0.007
Total (sum of materials)		1.25	^{238}U	<1490	<0.29
			^{232}Th	<550	<0.35
Total (full body assay)	ICP-MS	0.95	^{238}U	1160 ± 20	0.110 ± 0.001
			^{232}Th	365 ± 6	0.174 ± 0.003

Table 1.14-1. Summary of all background contributions from signal plugs. ICP-MS is inductively coupled plasma mass spectrometry. GDMS is glow discharge mass spectrometry. NAA is neutron activation analysis. Material component masses are all approximate, with a bias towards larger masses.

1.15 Simulation and analysis activities for the MAJORANA DEMONSTRATOR

T. H. Burritt, M. Buuck, C. Cuesta, J. A. Detwiler, J. Gruszko, I. Guinn, J. Leon, D. A. Peterson, R. G. H. Robertson, and T. D. Van Wechel

The UW MAJORANA group leads the simulations and analysis effort within the MAJORANA collaboration. Much of the low-level software for data I/O, event building, data processing, and simulation were written by CENPA personnel. Members of our group have played a central role in the building and validation of the background model for the MAJORANA DEMONSTRATOR, which informs the radiopurity criteria upon which the experimental design is evaluated. We also participate in the development and implementation of data analysis techniques, geometrical models for Monte Carlo simulations, and data handling, storage, and database technologies. Our efforts over the past year have focused on workflow management, improvements to data processiong and cleaning, the development and use of analysis tools for data from the MAJORANA DEMONSTRATOR Prototype Module, and preparation for data taking with enriched Ge detectors.

As the Simulations and Analysis task leader for MAJORANA, Jason Detwiler oversees the development of the software tools necessary for full data taking. This past year, Detwiler implemented a working group structure to better organize the members of the collaboration around the software tasks at hand. This restructuring has been a great success, and has significantly accelerated the production of the MAJORANA software tools.

Clara Cuesta took the role of head of the Data Cleaning and Run Selection working group. The group has implemented a Data Cleaning Framework to identify different types of events and to specify cuts to remove non-physics events from data-sets. External variables, such as environmental effects, are being integrated with the Ge data to be studied. Run and channel selection tools are being developed to automatically determine which runs will be used in neutrinoless double-beta decay analysis. Good runs will be integrated into data sets and a database will handle all the information, including the blind data. Finally, the total exposure and efficiency of the experiment will be determined. Run evaluation has been done with the prototype module data and will be done for Module 1 as soon as it starts taking data.

Micah Buuck has primarily been focused on implementing a pulse-shape-based analysis technique for rejection of background multi-site events. In this capacity, he is a part of the Pulse Shape working group. The technique requires the generation of a "basis library" of single-site event pulses, which is then used to accept or rejcet incoming pulses based on a χ^2 fit. He has successfully implemented the software necessary to generate the basis, and is now working on streamlining the process and applying it to physics data.

Ian Guinn has significantly improved the event builder for the MAJORANA DEMONSTRATOR. The event builder has three main responsibilities. First, it converts the raw data files produced by the data acquisition system (ORCA) into ROOT files, known as built files, that are compatible with the MAJORANA software. Second, it combines waveforms and muon veto events that occur at closely separated times into a single event, in order to detect coincidences. Finally, it filters out corrupted data that may confuse the main analysis software, a process known as garbage collection. Guinn has made several improvements to the event builder in the last year, including but not limited to: the addition of tools to read the ORCA XML header file, which contains important information about the hardware configuration, the ability to read out events from the muon veto, the addition of the garbage collector, and a 6-fold reduction in file size.

Julieta Gruszko has successfully implemented and begun to use new frequency-domain analysis techniques. She will use the techniques to identify and eliminate noise sources and for data cleaning. The resulting noise curves of detector baselines will be used to characterize the detector, to accurately simulate pulses, and for optimum filtering. The tools she developed this year allow researchers to view noise curves over time, which can be used to identify intermittent noise sources and therefore tag events for data cleaning. Average noise curves taken with the Prototype Cryostat system are being used to identify the optimal electronics setup and laboratory conditions for data taking. For an example, see Fig. 1.15-1.

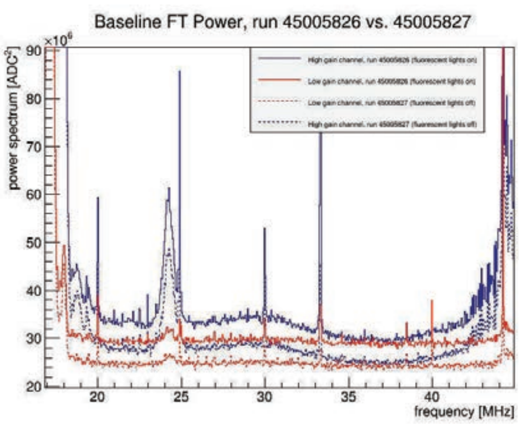

Figure 1.15-1. A comparison of the white noise levels showed that the use of fluorescent lights in the lab was introducing noise. Following this study, the shielding of module electronics box was improved.

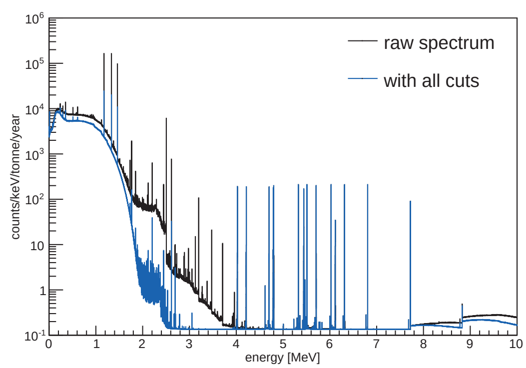

Figure 1.15-2. Full-spectrum background model for the MAJORANA DEMONSTRATOR, with and without analysis cuts.

Our attention is now turning toward completing preparations for the first data to come from the enriched Ge detectors. New assay results have improved the predicted background rate in the 4-keV region of interest surrounding the 2039 keV Q-value for double-beta decay of ^{76}Ge to 3.1 counts/ton-year. Major simulation campaigns are underway to provide up-to-date predictions for the full spectrum we expect to see with enriched detector data. Fig. 1.15-2 shows the full simulated spectrum, including the effect of analysis cuts. Other major activities include software quality assurance tests, database implementation of run information recording and automatic data workflow management, refinement of event building routines, optimization of energy estimation and pulse-shape parameter extraction algorithms, and data monitoring and cleaning routines.

1.16 Low-noise forward-biased preamplifier tested with a mini-PPC Ge detector

J. A. Detwiler, J. Leon, D. A. Peterson, R. G. H. Robertson, and T. D. Van Wechel

P-type point contact (PPC) germanium detectors are in principle sensitive to very low-energy nuclear recoils, such as those produced by coherent scattering of dark matter particles or neutrinos. In order to realize this sensitivity, low-noise electronics capable of achieving sub-keV energy thresholds are required. We report on the development of a low-noise charge-sensitive preamplifier which is continuously reset by the forward-biased gate-to-source junction of an input tetrode JFET. In contrast to commonly used reset mechanisms, this design avoids the noise associated with a feedback resistor while also providing continuous operation. Refer to previous reports for more information on the preamplifier's design principle and operation[1].

Whereas previous protoypes have only been tested with Si PIN diode detectors, the most recent prototypes have been designed to work with a Ge detector. Given the small signals produced by PPC Ge detectors, the first-stage (or front-end) amplifier must be connected near the detector. Otherwise, capacitive loading from long cables would reduce the signal-to-noise ratio. For this reason, it is crucial to choose materials that can be made or found to be low in radiactive backgrounds. Our front ends were fabricated out of gold on a fused-silica wafer[2]. This substrate material has a low loss tangent (10^{-4}) for low dielectric dissipation noise, and good thermal conductivity (41.9 W/mK) which makes it possible to control and optimize JFET temperature. Fabrication of the front ends was performed at the UW Nanofabrication Facility using standard photolithographic techniques. A thin adhesion layer of Ti was deposited followed by 4000Å of Au to form the circuit traces. Bare-die Moxtek MX-30 JFETs were epoxied on the front end and wirebonded to the gold traces (see Fig. 1.16-1).

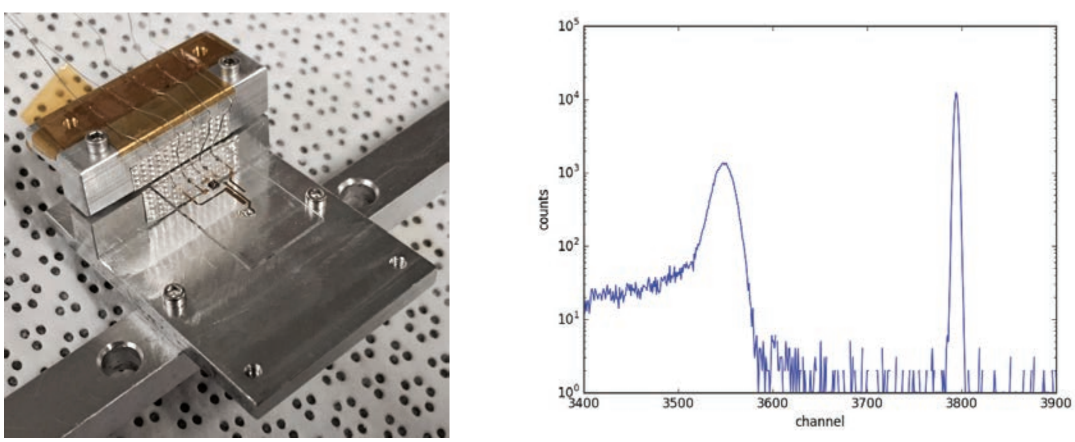

Figure 1.16-1. *Left:* A front end board (20 mm X 10 mm) made from 500-mm-thick fused silica, shown here clamped in aluminum mount. *Right:* Pulse-height spectrum collected with Amptek MCA8000D using ^{241}Am and injected pulser. Semi-gaussian shaping time set to 24 μs and pulser frequency at 500 Hz. Refer to text for more information.

[1] CENPA Annual Report, University of Washington (2013) p. 24.

[2] From MarkOptics, Corning 7980

A miniature PPC Ge detector (mini-PPC) has been used to test our preamplifier. The mini-PPC[1] has low leakage current (<1 pA) and low capacitance (∼0.5 pF), which means it has the intrinsic low-noise performance necessary to test our preamplifier. A tensioned pin between the preamplifier and detector makes the electrical connection to the input. This system is cooled down to 87 K inside a cryostat via a copper coldfinger. Signals generated by the detector are amplified by the front end and passed to a second-stage amplifier. We can subsequently pass these amplified signals through a semi-gaussian shaping amplifier and measure the pulse-height spectrum with a multi-channel analyzer (MCA). Fig. 1.16-1 contains an energy spectrum collected in such a way using an ^{241}Am source. The peak on the left is from the source's 59.5 keV gamma, which is used for energy calibration. The energy of the pulser peak (63.5 keV) on the right corresponds to an injected amount of charge, which in turn is used to calibrate the feedback capacitor (∼0.16 pF). The electronic noise level can also be inferred from the full-width-half-maximum (FWHM) of this pulser peak, 73 eV FWHM. This demonstrates one of the lowest electronic noise levels observed with a PPC Ge detector, even when the mini-PPC's low capacitance is taken into account.

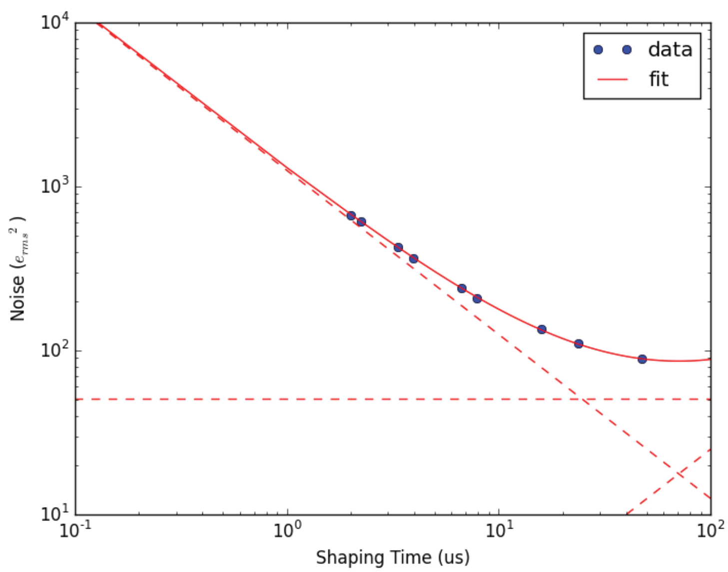

Figure 1.16-2. Noise level of preamplifier connected to mini-PPC at 150 V bias and 87 K, in terms of squared electrons-RMS versus full-width-half-maximum time of a semi-gaussian shaper (blue dots). Also shown are a three-component fit to data (red solid) and individual noise component fits (red dashsed).

Alternatively, the noise level can be measured from the RMS of baseline noise. In this method, the output from the shaping amplifier was passed on to a digital oscilloscope that was then used to average the RMS of ten baseline noise traces. Fig. 1.16-2 shows the electronic noise measured in this way versus shaping time. The minimum of this curve corresponds to about 65 eV FWHM, which is consist with the previous measurement method if one considers potential pulser instabilities and the effects of pileup. Additional tests with a ^{60}Co source show that this system has a linear energy response out to at least 1.33 MeV.

[1]2 cm X 1 cm cylinder fabricated at Lawrence Berkeley National Lab.

2 Fundamental symmetries and non-accelerator-based weak interactions

Torsion-balance experiments

2.1 Progress on the upgrade of the wedge-pendulum experiment for testing short-range gravity

E. G. Adelberger, S. Fleischer, C. D. Hoyle*, J. G. Lee, and H. E. Swanson

The plans for a comprehensive upgrade of the Fourier-Bessel short-range experiment have been described in the previous annual report[1]. In short, the upgrade consists of a new set of pendulum and attractor disks, an improved electrostatic shield with a motorized in-situ alignment system for the attractor-shield gap, a new vacuum chamber and pump line, a new calibration turntable, and new in-vacuum wiring and optical readout alignment.

With the exception of the new pendulum and attractor, all parts of the upgrade have been manufactured, tested, and are ready to be deployed. After some further improvements to the alignment system, we have demonstrated working separations of less than 5 μm between the attractor and the electrostatic shield.

Regarding the production of the new pendulum and attractor, we have developed a better process to glue the patterned platinum foils to the supporting glass substrate. It allows for significant improvements in terms of flatness, and it completely avoids the problem of surface irregularities as seen in the old process. Unfortunately an attractor disk assembled in this way showed clearly measurable permanent magnetization. The magnetic contamination probably comes from a layer of stainless-steel foils which — due to a miscommunication — surrounded the stack of platinum foils during the electric-discharge machining (EDM) of the foil patterns. In the meantime, we have investigated the potential of our new UV-laser prototyping setup for a radically simplified pattern-manufacturing process. While some issues related to burr formation in the laser-cutting process still need to be addressed, it looks as though this might be a feasible way to produce the pattern for the Fourier-Bessel experiment. It would be dramatically faster and cheaper than our previous EDM-based method. Additionally, as it would allow cutting the active pattern into a metal foil that has already been glued to a glass substrate, it would solve several problems in the gluing and centering process. As a further safeguard against the magnetic contamination issue, we will screen the raw materials for magnetic impurities before assembling the next pieces.

In summary, almost all parts of the short-range setup upgrade have been manufactured and tested, and are ready to be deployed. They can be installed as soon as the data-taking

*Humboldt State University, Arcata, CA.

[1]CENPA Annual Report, University of Washington (2014) p. 33.

for the spin-spin experiment has been completed. The only remaining question concerns the best process to create and mount the active patterns for the pendulum and the attractor. Significant progress has been made in this regard, and we may have a much cheaper and faster method available now. We are looking at mitigating the problems related to burr formation. Additionally, the extensively researched EDM-based process is available as a fallback solution.

2.2 Progress on a high-precision ground-rotation sensor for Advanced LIGO

J. H. Gundlach, C. A. Hagedorn, M. D. Turner, and K. Venkateswara

Advanced LIGO (aLIGO) is a next-generation gravitational-wave-detector system expected to make first detections in the next few years. Key among the improvements in the new detector is a better seismic isolation system to cancel the effect of ground motion on the suspended optics. This is done through an active-control system which measures the ground translation through seismometers and applies a corrective force on the optics platform. However, at low frequencies (10-500 mHz) conventional seismometers and tiltmeters are unable to separate ground rotation (tilt) and horizontal acceleration, which limits their ability to correct for ground translation. Thus, aLIGO needs a ground-rotation sensor to accurately distinguish between horizontal-ground acceleration and rotation. Such an instrument is not commercially available and the required sensitivity of the rotation sensor is challenging to reach.

Over the last four years, we have developed two prototype instruments that meet a significant part of the requirement specified by the seismic-isolation team for aLIGO in the frequency range of 40 to 400 mHz. The device consists of a low-frequency flexure-beam balance. We measure its angle using a multi-slit autocollimator mounted rigidly to the ground. Above its resonance frequency, the balance remains inertial, thus the autocollimator measures ground rotation. Torque from horizontal acceleration is rejected by locating the center of mass at the pivot point of the flexure. The prototype beam-balance consists of a 0.75-m aluminum tube with 1.8 kg-brass weights attached at each end. It is suspended by two, 15-μm-thick, copper-beryllium flexures. The entire balance is surrounded by an aluminum heat shield and is placed in high vacuum to minimize thermal effects.

One rotation sensor was installed at one of the end-stations at the LIGO Hanford Observatory. It is now referred to as the Beam Rotation Sensor (BRS). Under windy conditions, tilt as measured by the BRS has been shown to be very coherent with a seismometer output at frequencies below 0.1 Hz, and has been used to remove tilt-induced noise from the seismometer output. Fig. 2.2-1 shows an example of a measurement taken when wind speeds were between 15-25 mph. In the top plot, the red trace shows the tilt measured by BRS, the blue curve shows the seismometer output (converted to angle units), and the cyan curve shows the tilt-subtracted ground translation signal. At frequencies greater than 0.1 Hz, the cyan curve follows the blue, but below that frequency, tilt dominates the seismometer output. Also shown as the purple trace is the BRS reference signal, which is indicative of the instrument noise, and the output of a seismometer mounted on the optics platform is shown in green. The bottom plot shows the coherence between the two seismometers and the BRS, indicating that tilt constitutes a significant part of the low-frequency signal in both seismometers.

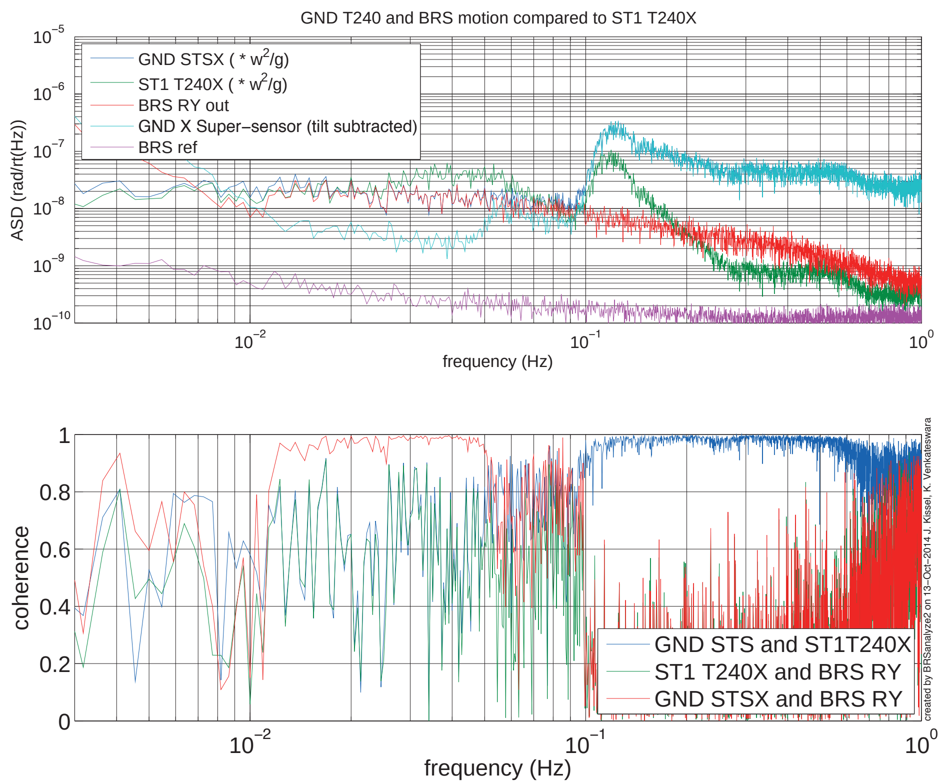

Figure 2.2-1. Seismic data measured at LHO. Top plot shows the ground rotation recorded by our sensor (BRS, red) in comparison to a seismometer (T240, blue) measured at LIGO Hanford Observatory. Also shown are the tilt-subtracted translation signal (cyan), sensor noise (purple) and the optics platform motion (green). Bottom plot shows the coherence between the two seismometers and the BRS.

Measuring the tilt-free translation of the ground has been demonstrated to improve the isolation performance of the optics platform by reducing its low frequency motion, especially in windy conditions. Doing so enables more consistent locking of the interferometer and can help reduce up-conversion effects and hence improve its sensitivity. Further testing and characterization of this instrument is currently underway at LHO.

At our lab, we are building a new compact version of the BRS with several improvements. A new compact readout using two fiber-optic interferometers is being developed to improve sensitivity. A mechanism for repeatable locking of the beam balance is being tested to enable the instrument to be transported safely. Further, the balance will have a cross shape to reduce sensitivity to gravity gradient noise.

2.3 Silica fibers for increased torsion-balance sensitivity

J. H. Gundlach, C. A. Hagedorn, J. G. Lee, E. A. Shaw, W. A. Terrano, M. D. Turner, and K. Venkateswara

We are exploring fabrication and use of fused silica as a superior torsion fiber material for several torsion-balance experiments, with a focus on our equivalence-principle test. Many of our torsion balances are limited by Brownian motion intrinsic to the torsion fiber. The thermal torque noise power, for an internally-damped fiber, is $\tau(f) = \sqrt{2k_BT\kappa/(\pi Q f)}$, where k_B is Boltzmann's constant, T the fiber temperature, κ the fiber torsion constant, and Q the mechanical quality factor. To minimize noise we must minimize the ratio of the torsion constant κ to the Q factor[1]. We have made silica fibers with torsion constants comparable to those of tungsten fibers with equal tensile strength. In addition, we have measured $Q \sim 270,000$ in one of these fibers compared to the best $Q \sim 6000$ for tungsten fibers. It is likely that the Q of this fiber is still limited by non-fiber losses.

In past work, flame-pulled fibers reached high Q at modest tensile strength, but fabrication was difficult and inconsistent[1]. Our recent improvements were enabled by the CO_2 laser at CENPA[2]. Last year, we built an apparatus that used the laser to pull fibers, but not of the right diameter nor length. The main improvement was to switch from fiber pulling powered by a stepper motor to using the laser cutter's integrated servo rotary stage. With smoother operation and integrated timing between the laser control and rotary stage, we were able to reliably explore the fiber-pulling and laser-heating parameter space.

We have improved the characterization of our fibers. After pulling, fibers are checked with a reference pendulum for satisfactory κ and minimum breaking strength. At fixed κ the tensile strength is limited by thin spots in the fiber. Fiber uniformity is critical to optimal performance. We imaged our fibers along their entire length using the CENPA SmartScope and used custom Python software to determine fiber diameter curves. These characterizations allowed us to improve on uniformity and reproducibility. A fiber measurement is shown in Fig. 2.3-1 (*left*).

To measure fiber Qs and torque noise, we restored the LISA apparatus[3] and attached one of our new autocollimators[4] . Our first laser-pulled fiber initially displayed $Q \sim 28,000$, low for a silica fiber. After excluding gas damping, we found that the dominant loss was magnetic. Canceling ambient fields with Helmholtz coils gave a Q of 60,000-70,000. Inserting a refurbished μ-metal shield gave us $Q = 271,000 \pm 1,000$, shown in Fig. 2.3-1 (*right*). We

[1] C. A. Hagedorn, S. Schlamminger, and J. H. Gundlach, 2006 Proc. 6th Int. LISA Symp. AIP Conf. Proc. **873**, 189 (2006).

[2] CENPA Annual Report 2013, pp 118.

[3] S. E. Pollack, M. D. Turner, S. Schlamminger, C. A. Hagedorn, and J. H. Gundlach, Phys. Rev. D **81**, 021101(R) (2010).

[4] CENPA Annual Report 2013, pp 47.

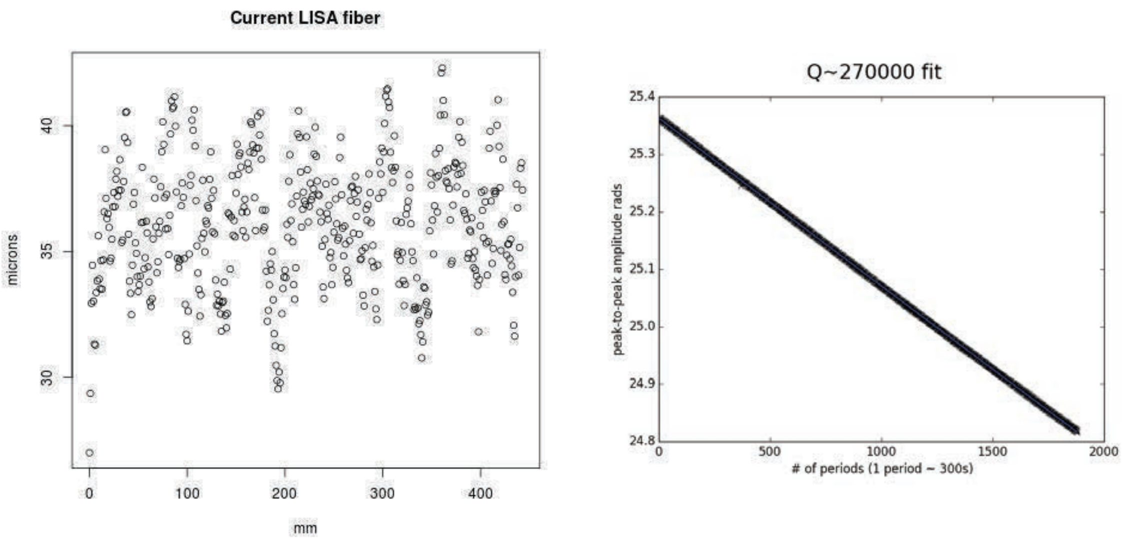

Figure 2.3-1. *Left:* Diameter-vs-length characterization of fiber currently being used for Q measurements and investigation of noise. *Right:* Q measurement at large amplitude done by measuring the time of zero crossings of the pendulum mirrors and using that information to fit a sine curve for each period.

are installing a purpose-built magnetic shield to minimize magnetic damping further. We will continue our investigation of silica fibers until they reliably surpass tungsten as our fiber of choice.

2.4 Parallel-plate inverse-square-law test

J. H. Gundlach, C. A. Hagedorn, M. D. Turner, and K. Venkateswara

This has been a year of documentation and data analysis. We will unblind our parallel-plate test of gravity[1] at sub-millimeter scales on May 5, 2015. Charlie Hagedorn's thesis is nigh complete, pending a post-unblinding conclusion.

Our bootstrapped analysis method allows easy accommodation of difficult-to-model systematic uncertainties, including the important effects of isolating-foil displacement and systematic uncertainty in the pendulum-attractor distance ("horizontal error bars"). While bootstrapping removes analytic intuition from error propagation, its simplicity is an advantage.

A small, important, insight is that, in the Yukawa parametrization, in which Newtonian gravity is modified to the form $V(r) = -G\frac{m_1 m_2}{r}\left(1 + \alpha e^{-r/\lambda}\right)$, α and λ share no *a priori* relationship. Thus, the traditional 'pick a λ, fit for α' approach to constraining inverse-square-law violations is more appropriate than sophisticated approaches like kernel-density estimators. Our bootstrapped method is quite traditional, determining α exclusion limits at

[1] CENPA Annual Report, University of Washington (2014) p. 32.

a given λ from best-fit points with nearby λ. If there is a signal to find, our method moves smoothly from exclusion to detection.

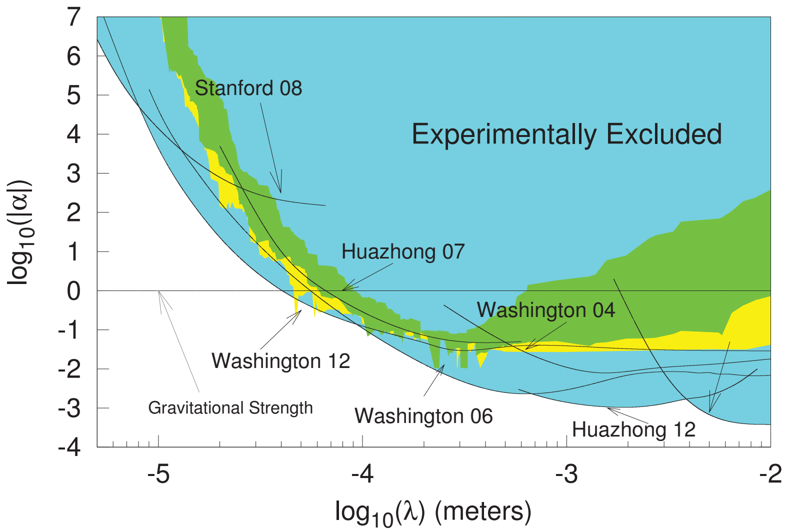

Figure 2.4-1. Expected limits for this iteration of the parallel-plate experiment, including systematic uncertainties. Our 2σ limit should fall in the green or yellow (optimistic) regions.

Useful upgrades for the experiment are clear: Re-enabling our pendulum/foil voltage control system will yield an immediate improvement in signal-to-noise ratio and decreased systematic coupling. This change, along with minor improvements to the autocollimator, alignment, and data-taking procedure, should yield an improved measurement within six months of running time. An upgraded pendulum may allow greater sensitivity through improved metrology and electrostatic properties. Our automated analysis software is ready for a second round of data.

2.5 Improved short range spin-coupled force test

E. G. Adelberger, B. R. Heckel, J. G. Lee, and W. A. Terrano

We have upgraded the torsion pendulum designed to look for short-range spin-coupled forces[1]. Residual magnetic couplings and thick magnetic shielding limited the previous version. Upgrades consisted of multiple improvements to magnetic shielding and thinner components to decrease separations, increasing the sensitivity of the balance and increasing the signal respectively.

Multiple layers of thin magnetic shielding proved to be more effective than a single thick layer. The 0.030” mu-metal cans on the 20-pole magnet of the pendulum and attractor were each replaced with two layers of 0.010” nested mu-metal cans with a layer of 0.001” aluminum foil between each can. The new shielding was tested on a turntable under a

[1]CENPA Annual Report, University of Washington (2014) p. 36.

GMR probe showing a factor of about 14 improvement in the magnetic field peak-to-peak (Fig. 2.5-1). Alternating 76-μm tungsten and titanium shims glued directly to the magnet rings eliminated a 0.050" alignment disk and gravitationally compensated both the pendulum and attractor.

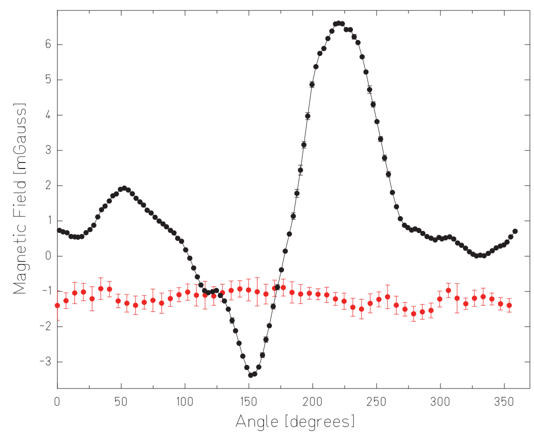

Figure 2.5-1. Magnetic field from enclosed 20-pole magnets. Black is with a single 0.030" mu-metal can; red is with two nested 0.010" mu-metal cans.

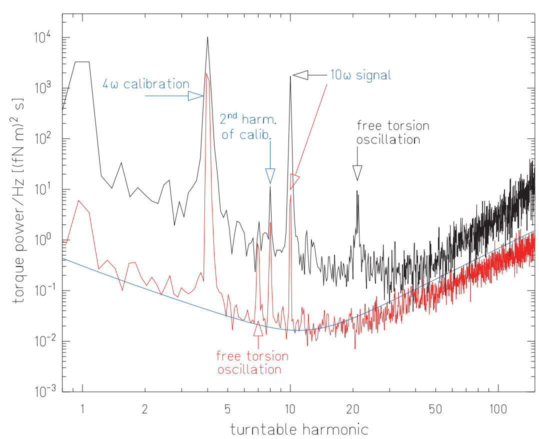

Figure 2.5-2. Improved torque sensitivity in the 2015 vs. the 2014 gravitational data. The improved noise floor comes from moving from a 30-μm fiber to a 20-μm fiber, a higher Q from improved shielding, and a faster rotation rate. The smaller 10ω peak comes from improved gravitational compensation.

The improved shielding decreased the loss of the pendulum oscillation, $1/Q$. We also replaced the 30-μm fiber of the previous test with a 20-μm fiber. Additionally, the electrical contact on the turntable was replaced with a design that caused less friction and allowed a faster rotation rate. The increase in Q (1.6x), thinner fiber (2x), and faster attractor rotation rate (1.4x) improved the torque sensitivity of the balance by a factor of 4.5, as shown in Fig. 2.5-2. Finally, we replaced the shielding screen with 10 layers of 0.002" mu-metal and 1 layer of 0.010" mu-metal, all with 0.001" aluminum foil spacing between each layer.

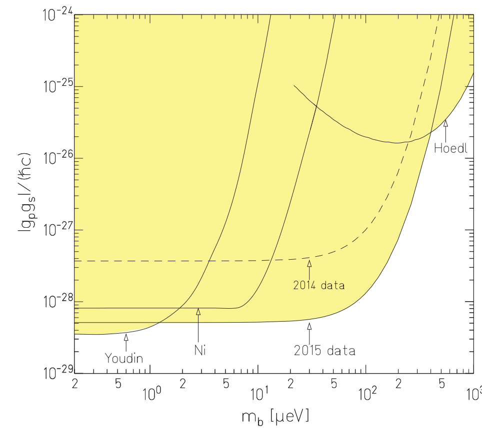

Figure 2.5-3. New limits on a monopole-dipole force. The shaded region is excluded at 1σ

Data-taking with the gravitational attractor is complete and has led to improved limits on CP-violating monopole-dipole couplings (Fig. 2.5-3) for bosons of mass between 1 and 400 μeV. Data-taking with the spin attractor is complete, having reached a torque sensitivity of 2 atto-Nm and an a attractor to pendulum separation of 4.1 mm, down from 6.1 mm. This data sets new limits on dipole-dipole interactions for all mass ranges (Fig. 2.5-4 *left*). Interpreting these results as excluding new Goldstone bosons implies that a new hidden symmetry must be broken at a scale $F > 100$TeV for bosons with mass less than 100μeV (Fig. 2.5-4 *right*).

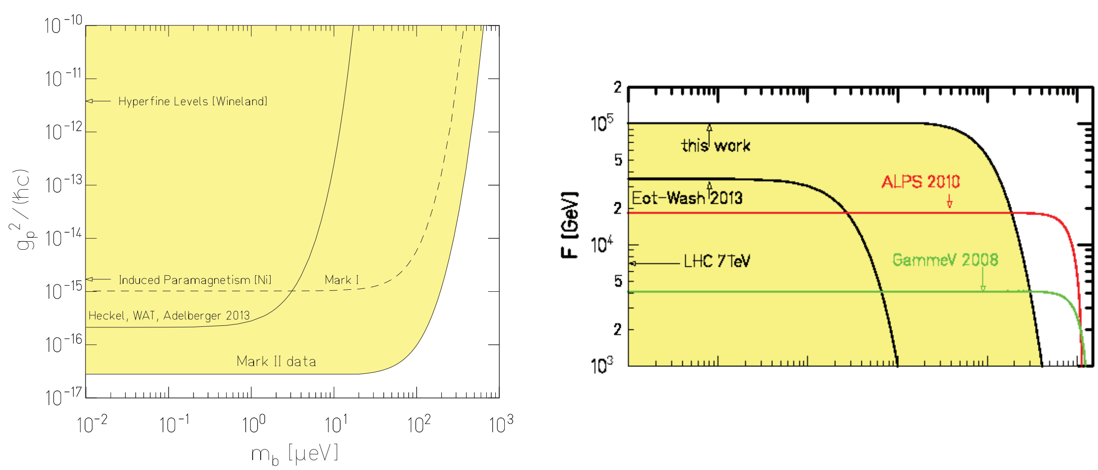

Figure 2.5-4. *Left:* New limits on dipole-dipole interactions. The shaded region is excluded at 1σ. *Right:* New limits on a hidden high-energy symmetries. The shaded region is excluded at 1σ.

Non-accelerator-based weak interactions

2.6 The ^{199}Hg electric-dipole-moment experiment

Y. Chen, B. Graner, B. Heckel, and E. Lindahl

The ^{199}Hg EDM experiment has been taking data since the summer of 2013. After a several-month delay due to the failure of the UV laser system, data acquisition resumed. In February, 2015, a complete data set was completed. An initial analysis of the data revealed a new systematic error associated with small movements of the stack of ^{199}Hg vapor cells due to forces induced by the applied electric field. We are currently taking additional auxiliary data to better understand the impact of the vapor cell movement onto the EDM signal.

The ^{199}Hg EDM apparatus uses UV laser light to polarize and measure the spin precession frequency of ^{199}Hg atoms in a stack of 4 vapor cells, 2 of which (the inner pair) have oppositely directed electric fields. A pump-probe sequence is employed, with the electric fields reversed between each pump-probe cycle. A blind frequency offset is added to the inner-cell frequency difference to mask the EDM signal until the analysis of the entire data set is complete. EDM data collection is divided into "sequences", groups of 16 days of data distinguished by the ordering and orientation of the 4 vapor cells. Each sequence includes equal numbers of runs with electric field magnitudes of 6 kV/cm and 10 kV/cm, magnetic field normal and reversed, and slow and fast electric field ramp rates. We have completed 12 sequences of EDM data, a complete set of data for 3 vapor cells cycling through the EDM-sensitive positions in the apparatus.

Fig. 2.6-1 shows the EDM measurements taken at 10 kV/cm for the 12 data sequences. Each run represents one day of data accumulation. A similar data set exists for measurements taken at 6 kV/cm.

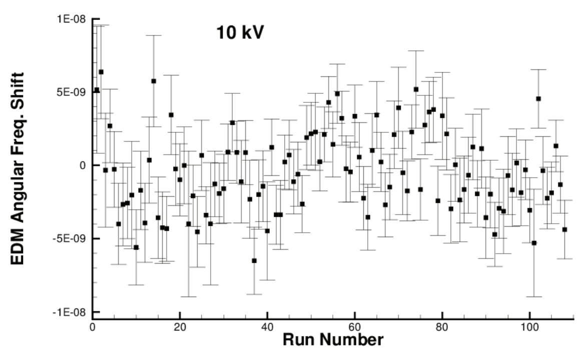

Figure 2.6-1. Angular frequency (rad/s) Hg EDM results for the 10 kV/cm data sequences.

Preliminary analysis of the data gives a statistical error on the ^{199}Hg EDM of $2.7 \times 10^{-30} e\,\text{cm}$. This represents an improvement by a factor of 5 over our previous ^{199}Hg EDM result from 2009. There is good agreement between the data taken at 10 kV/cm and 6 kV/cm, and between data taken for the two magnetic field directions. The systematic error analysis is in progress and we expect to complete the analysis and unblind the data in the summer of 2015. This project is supported primarily by the NSF (P. I. Heckel).

3 Accelerator-based physics

Accelerator-based weak interactions

3.1 Overview of the ^{6}He experiments at CENPA

Y. S. Bagdasarova, K. Bailey*, C. Devon, X. Fléchard†, A. García, R. Hong, A. Knecht‡, A. Leredde*, G. Leum, E. Liénard†, P. Müller*, O. Naviliat-Cuncic§, T. P. O'Connor*, W. Shaffer, M. G. Sternberg, J. Stiebritz, D. W. Storm, H. E. Swanson, M. Van Genabeek, F. Wauters, and D. W. Zumwalt

We are carrying out an experiment to search for tensor currents by measuring the correlation coefficient between the electron and the antineutrino (called "little a") from ^{6}He beta decay. The tensor currents flip chirality and are forbidden in the standard model but predicted by some extensions of it.

Our present effort aims at determining the $e-\nu$ correlation coefficient at the level of 0.1% (about 1 order of magnitude improvement over previous measurements) by trapping ^{6}He in a laser Magneto-Optical Trap (MOT). The electron is detected via a combination of a multi-wire proportional chamber and a scintillator. The recoiling Li ions are detected via a focusing electric field that guides them onto a position-sensitive Micro Channel Plate (MCP) detector. By measuring the time of flight and the landing position of the Li ion the Li momentum can be reconstructed. Both the electron and Li momenta can be used for reconstructing the anti-neutrino momentum.

During the last year much progress has occurred in making the ^{6}He production more stable, improving and developing calibrations for the detector setup systems, improving the He trapping systems and understanding possible systematic uncertainties. A new source for pumping He into its metastable state has been constructed, installed and recently modified to allow the recirculation of the ^{6}He and to improve the trapping efficiency.

The following articles describe progress in each area. We have taken some data to debug our systems and we are aiming at getting the first data to determine little a to $\sim 1\%$ before the end of the summer of 2015.

*Physics Division, Argonne National Laboratory, Argonne, IL.
†LPC-Caen, ENSICAEN, Université de Caen, Caen, France.
‡Paul Scherrer Institute, Villigen, Switzerland.
§Department of Physics and Astronomy and National Superconducting Cyclotron Laboratory, Michigan State University, East Lansing, MI.

3.2 ^{6}He source developments for the β-$\overline{\nu}$ angular correlation experiment

Y. S. Bagdasarova, K. Bailey*, X. Fléchard†, L. Fonte†, A. García, A. Hillman, R. Hong, A. Knecht‡, A. Leredde*, G. Leum, E. Liénard†, P. Müller*, O. Naviliat-Cuncic§, T. P. O'Connor*, W. Shaffer, M. G. Sternberg, D. W. Storm, H. E. Swanson, M. Van Genabeek, F. Wauters, and D. W. Zumwalt

The ^{6}He source has continued to provide consistent, abundant production for the $\beta-\overline{\nu}$ angular correlation experiment[1] via the ^{7}Li(d,^{3}H)^{6}He reaction using 18 MeV deuterons provided by CENPA's tandem Van de Graaff accelerator. With little tuning, ^{6}He production rates exceeding 10^{10} atoms/s are readily achieved. Last year we reported[2] on improvements which made the system more robust, including an all-stainless steel redesign of the main target housing which can better handle the high-intensity deuteron beam used in the production of ^{6}He. Since that time we have made additional improvements to the system.

The previous target housed lithium inside a stainless-steel vessel. Separating the lithium from the beamline vacuum was a 2 mil (50 μm) stainless-steel foil. Stainless steel had been chosen because it is one of the few materials which does not react chemically with lithium. However, the intense deuteron beam, which is typically focused to a 1-mm diameter, caused strong local heating on the stainless-steel foil. Liquid lithium backing the foil helps to cool the foil, acting as a heatsink, but the poor thermal conductivity of stainless steel caused the foil to melt, sometimes within one day of bombardment.

The chemical reactivity of lithium presents a short list of suitable candidates to replace stainless steel, but tantalum is one of them. Tantalum is an attractive choice because it has a significantly higher melting point compared with stainless steel (3020 °C for tantalum compared with ∼1400 °C for typical stainless steels). Tantalum is a very strong metal as well, so comparatively thin foils can be used which can still withstand 1 atm pressure differentials. The deuteron beam deposits less energy into thinner foils which further aids in the suppression of local heating. We therefore now use 0.3 mil (0.75 μm) tantalum foils to separate the lithium from the beamline vacuum. In doing so we have extended the operating life of our targets at maximum beam intensities from hours to weeks. Fig. 3.2-1 shows a comparison between the effects of high-intensity beam exposure for stainless steel and tantalum foils. While the stainless steel foil suffered a complete rupture after several hours, the tantalum foil only begins to show signs of any kind of wear after more than 60 hours of uninterrupted beam.

Good contact between the liquid lithium and the foil is crucial in maintaining foil integrity over long runs. If left undisturbed the local heating from the deuteron beam would begin to evaporate the lithium on the surface of the foil, forming a void which is not always filled by the surrounding bulk liquid. To prevent these voids from forming, we had previously

*Physics Division, Argonne National Laboratory, Argonne, IL.
†LPC-Caen, ENSICAEN, Université de Caen, Caen, France.
‡Paul Scherrer Institute, Villigen, Switzerland.
§Department of Physics and Astronomy and National Superconducting Cyclotron Laboratory, Michigan State University, East Lansing, MI.

[1] CENPA Annual Report, University of Washington (2014) p. 42.
[2] CENPA Annual Report, University of Washington (2014) p. 45.

installed a stirring paddle which was inserted into the bulk lithium metal via a rotatable translation feedthrough. Its function was twofold: first, by lowering or raising the hemi-cylindrical paddle, the lithium could be displaced vertically to maximize production, and second, by periodically stirring the lithium, the surface of the foil could be recoated with lithium to ensure thermal contact. At low intensities this stirring was only needed every few hours, and the activity in the target cave was low enough that personnel could enter the room safely shortly after the deuteron beam was off. Therefore the stirring had been done manually as needed. However, with increasing intensity we needed to stir more frequently, and needed to wait longer after deflecting the beam before we could safely enter the cave. To address these issues we have installed a remotely controlled auto-stirring system.

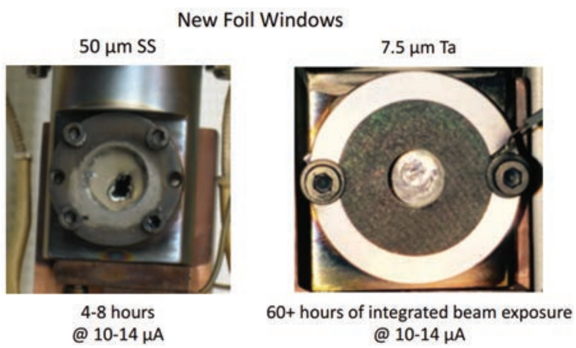

Figure 3.2-1. On the left, a stainless steel foil ruptured after several hours of beam. On the right, only minor signs of wear are seen on the new tantalum foil after several days of continuous beam exposure.

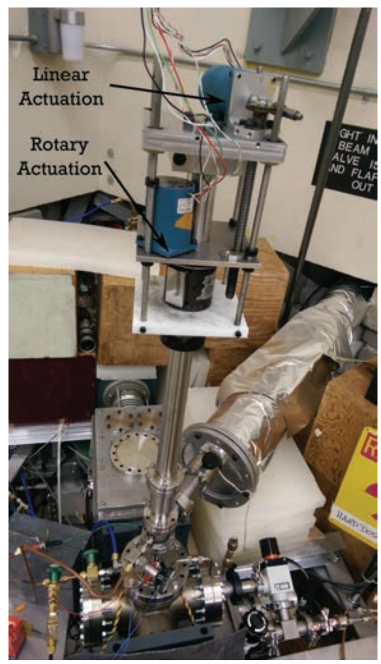

Figure 3.2-2. The remotely-controlled auto-stirring hardware which operates the internal stirring paddle of the lithium target.

The auto-stirrer consists of two stepper motors connected to the feedthrough which provide translation and rotation capabilities (see Fig. 3.2-2). The stepper motors are driven by an Arduino microcontroller which is in turn controlled by custom-written LabView software. The software automatically starts a fully programmable stirring cycle typically spaced at 20-minute intervals. The software additionally checks for interlocks before running, including a thermocouple interlock which does not allow the system to stir unless the lithium is above its melting point.

Through the combination of the new tantalum foils and the auto-stirring system, we have reduced or eliminated foil ruptures. In parallel, we are still developing a windowless target system which uses an electromagnetic pump to transport the liquid lithium metal through a fountain.

3.3 Systematics and calibrations of the array geometry and electric field for the ^{6}He experiment

Y. S. Bagdasarova, K. Bailey*, D. Carleton, X. Fléchard†, A. García, R. Hong, A. Knecht‡, A. Leredde*, E. Liénard†, P. Müller*, O. Naviliat-Cuncic§, T. P. O'Connor*, M. G. Sternberg, J. Stiebritz, D. W. Storm, H. E. Swanson, F. Wauters, and D. W. Zumwalt

Table 3.3-1 lists the contribution of the MOT-MCP distance and electrode voltage uncertaintites to the systematic uncertainty of a. The present parameter uncertainties δx are determined from calibrations outlined in this article.

Parameter x	$\partial a/\partial x$	$(\partial a/\partial x)/a$	δx	$\Delta a/a$
MOT-MCP Distance	-6.67E−05/100μm	-0.02%/100μm	100 μm	0.02%
Electrode Voltage	+1.00E−04/V	+0.03%/V	0.4 V	0.01%

Table 3.3-1. Systematic Uncertainty from Chamber Geometry and Electric Field Parameters.

The MOT-MCP distance calibration is a set of two calibrations: (1) a calibration of a new CCD camera to image the MOT position relative to the top electrode in the array and (2) a mechanical measurement of the distance between the top electrode and the MCP. To calibrate the camera, we machined a ruler assembly to rest on the top electrode as shown in Fig. 3.3-1. We engraved the face of the ruler with a $500-\mu$m-spaced grid using a laser cutter, and measured the dimensions of the ruler and grid to 6 μm using a microscope. We imaged the ruler face with the CCD camera through an iris aligned with the central ports of the chamber (Fig. 3.3-2) (chamber center) and thus determined the distance between the chamber center and the top electrode. We performed a mechanical measurement of the individual electrode spacings and thicknesses using precision gauge blocks and calipers. The composite distance from the top electrode to the MCP combined with the camera measurement yielded a chamber center-MCP distance of 94.628 ± 0.092 mm. The MOT-center distance is still unknown but we will determine this by imaging the MOT with the calibrated camera at the next opportunity to trap atoms.

The approximate MOT-MCP distance was also extracted by measuring the time of flight (TOF) of photoionized ^{4}He atoms as a function of uniform electric field strength E_0 (Fig. 3.3-3). The ^{4}He atoms were ionized using a pulsed nitrogen laser that is aligned with the MOT cloud, and the TOF peaks were fit to Gaussians to extract the centroids. Assuming the field is perfectly uniform, the TOF of ionized atom scales with the field like $TOF \propto \sqrt{Z/kE_0} + t_0$ where k is the field scaling factor that ranges from 0.2 to 1, and t_0 is the timing offset of the system. The unformity of the field is largely determined by the electrode voltages which were optimized using a simulation to yield maximal field uniformity ($\sigma_{E_0}/E_0 = 0.07\%$) in the

*Physics Division, Argonne National Laboratory, Argonne, IL.

†LPC-Caen, ENSICAEN, Université de Caen, Caen, France.

‡Paul Scherrer Institute, Villigen, Switzerland.

§Department of Physics and Astronomy and National Superconducting Cyclotron Laboratory, Michigan State University, East Lansing, MI.

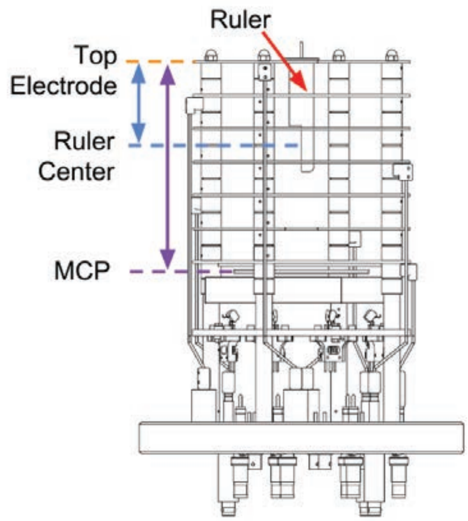

Figure 3.3-1. Placement of the ruler in the context of the electrode array. The distance from the top electrode to the MCP is measured mechanically. The distance from the top electrode to the ruler center is measured with a microscope.

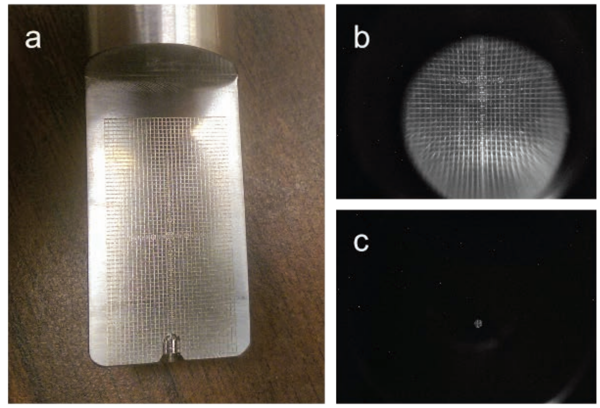

Figure 3.3-2. (a) Face of the ruler. (b) CCD camera image of ruler through iris aligned with chamber port (chamber center). (c) Iris closed in on grid point.

region of ion flight. Assuming a field strength of $E_0 = 1.55$ kV/cm, the TOF measurement produced a MOT-MCP distance of 94.04 ± 0.05 mm. A calculated correction of $+0.05$ mm must be applied to account for the non-unformity of the field produced by the measured 5.2 mm offset of the MCP from the simulated geometry. Additional uncertainty comes from the misalignment of the laser with the MOT center, which causes the TOF spectrum to distort and shift, but the severity of this effect is unknown.

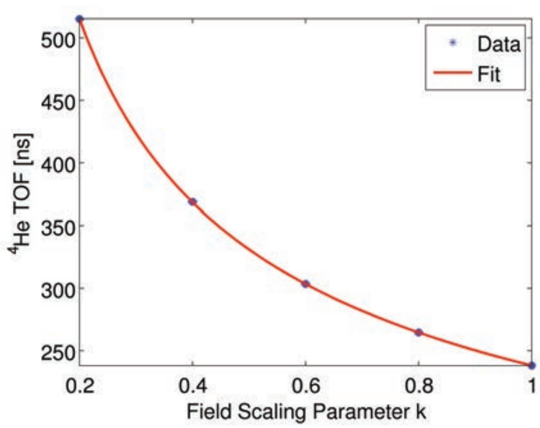

Figure 3.3-3. Fit of ^{4}He TOF data as a function of electric field scaling parameter k where $E_z = kE_0$ and $E_0 = -1.55$ kV/cm.

Comparing the ^{4}He measurement and the ruler measurement indicates a MOT-chamber center offset of 0.5 mm, which is not unreasonable and will be comfirmed or contradicted when we image the MOT with the CCD camera.

We measured the electrode voltages directy at the output of the power supplies with a NIST-calibrated high-voltage divider probe and a 6 1/2 digit multimeter. The listed uncertainty of $\delta V = 0.04$ V comes from the uncertainty of the probe in the voltage range of the electrodes nearest to the MOT, where the effect on the TOF is most pronounced.

3.4 β-detector calibration for the ^{6}He experiment

Y. S. Bagdasarova, K. Bailey*, X. Fléchard†, A. García, R. Hong, A. Knecht‡, A. Leredde*, E. Liénard†, P. Müller*, O. Naviliat-Cuncic§, T. P. O'Connor*, M. Sternberg, D. W. Storm, H. E. Swanson, F. Wauters, and D. W. Zumwalt

We performed several calibrations of the β-telescope of the ^{6}He β-ν angular correlation measurement. In short, the β-telescope consists of a multi-wire proportional chamber (MWPC) which measures the entrance position of the β-particle and a plastic scintillator-photomultiplier tube (PMT) assembly which measures the total energy of the β-particle. The γ-particle background in the scintillator is reduced by requiring a coincidence between the scintillator and the MWPC. The scintillator also starts the time-of-flight (TOF) measurement of the recoil ^{6}Li ion. Meanwhile, we ran Monte Carlo simulations for the calibration experiments and compared the simulated spectra with the measured ones.

We used an ^{55}Fe X-ray source to calibrate the position and energy response of the MWPC. Since the gas multiplication only happens on the anode wires and the perpendicular cathode wires create a non-uniform field, focusing some events towards the center between cathode wires, the position spectrum of the MWPC has peaks near positions ($\pm n$ mm, $1 \pm n$ mm) when illuminated with low-energy x-rays. Therefore, we designed an correction algorithm that moves the peaks to the positions where they are supposed to be, i.e. the intersections of anode wires and the center line between two perpendicular cathode wires. After this correction, the maximum difference between the peak position and its nominal position is less than 0.15 mm as is shown in Fig. 3.4-1. We observed the full-energy peak of the ^{55}Fe X-ray of 5.9 keV and the argon escape peak at $\sim$3 keV. We used the full-energy peak for the energy calibration of the MWPC. We divided the MWPC active region into 2 mm$\times$2 mm pixels, constructed the energy spectrum for each pixel, and fit the full-energy peak. We found that the gain is non-uniform across the active area of the MWPC as in Fig. 3.4-2. After applying with the gain correction according to the measurement, the energy spectrum of the whole MWPC agrees well with the simulation as shown in Fig. 3.4-3. Also, the energy response of the MWPC to β-particles from the ^{207}Bi source agrees with the simulation as shown in Fig. 3.4-4, after all corrections are performed.

*Physics Division, Argonne National Laboratory, Argonne, IL.

†LPC-Caen, ENSICAEN, Université de Caen, Caen, France.

‡Paul Scherrer Institute, Villigen, Switzerland.

§Department of Physics and Astronomy and National Superconducting Cyclotron Laboratory, Michigan State University, East Lansing, MI.

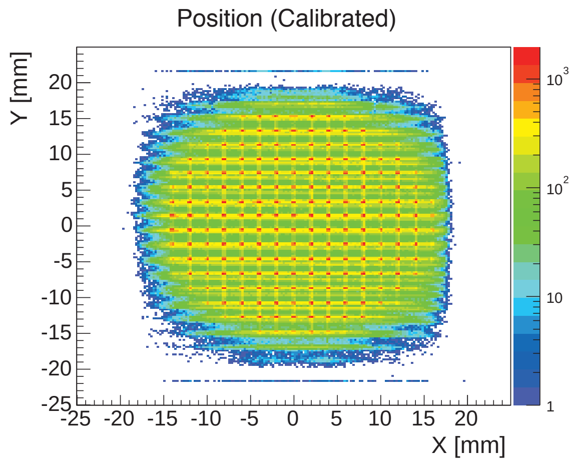

Figure 3.4-1. Calibrated position spectrum of the MWPC.

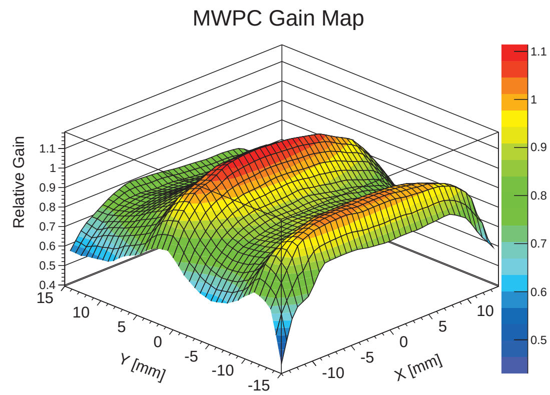

Figure 3.4-2. Gain map of the MWPC.

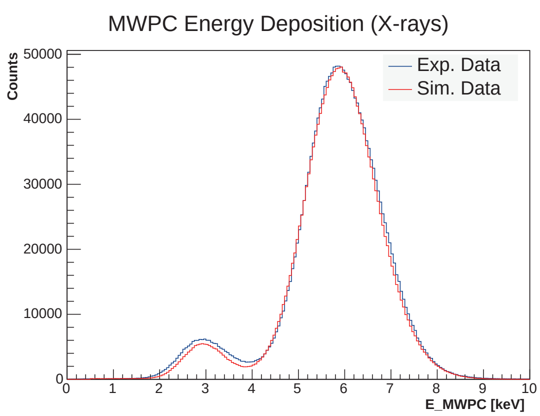

Figure 3.4-3. Calibrated MWPC energy spectrum of X-rays from ^{55}Fe.

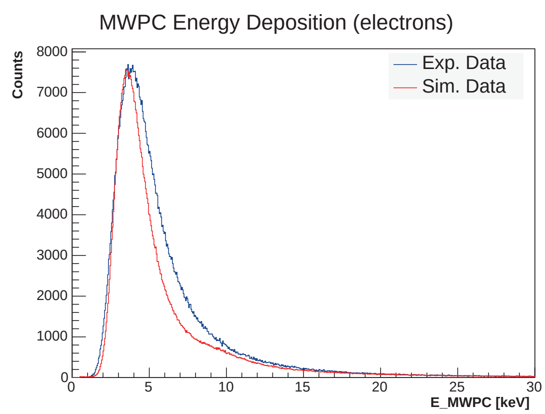

Figure 3.4-4. Calibrated MWPC energy spectrum of electrons from ^{207}Bi.

The energy response of the scintillator-PMT assembly was calibrated with ^{207}Bi conversion electron source. The source produces electrons at 976 keV, 482 keV, and 1682 keV. Using these three mono-energetic electron spectrum lines, we extracted a linear energy response function of the scintillator-PMT assembly. The low-energy tail of each peak is due to photo electrons from the source backing material, and the high-energy tail of each peak is due to coincidence detection of the two cascade decays from ^{207}Bi. As is shown in Fig. 3.4-5, the measured spectrum agrees very well with the simulation, and all peak deviations are below 1σ level. With this calibration precision, the β-energy threshold related systematic deviation in the β-ν correlation coefficient extraction is 0.08%.

The spatial uniformity of the scintillator-PMT assembly was studied by fitting the 976-keV peak of each pixel. The fluctuation of the energy response across the region of interest is less than 0.8% as is shown in Fig. 3.4-6. This non-uniformity can be corrected below the 0.1% level. The drift of the energy response with time is also less than 0.4%.

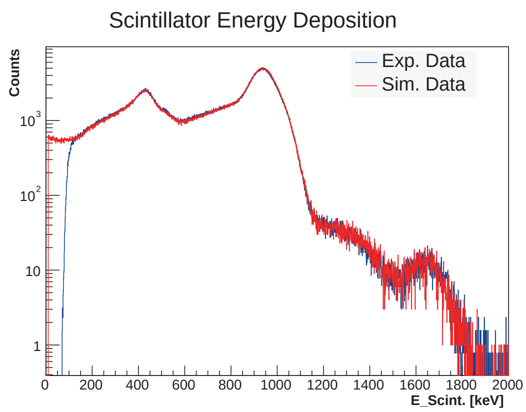

Figure 3.4-5. Energy response of the scintillator-PMT assembly using the ^{207}Bi source, compared with simulated data.

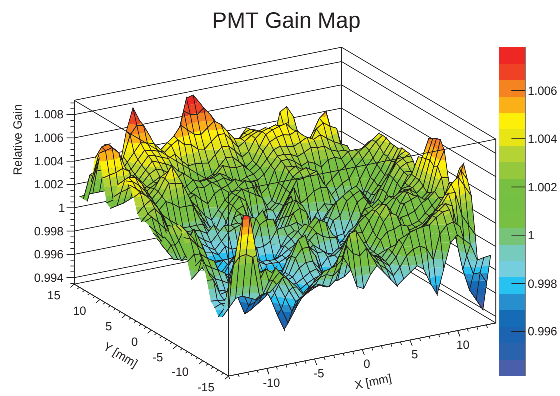

Figure 3.4-6. Gain map of the scintillator-PMT assembly.

The individual and overall systematic uncertainties related to the β-telescope is listed in Table 1.

Systematic effects	δa/a (%)
MWPC Center	0.19
MWPC Radius Cut	0.008
MWPC Position Resolution	0.05
MWPC Energy threshold	0.07
MWPC Efficiency non-uniformity	0.18
PMT Energy Response	0.08
PMT stability	0.07
total	0.30

Table 3.4-1. Systematic uncertainties related to the β-telescope.

3.5 Time-of-flight spectrum and kinematics reconstruction using the β-recoil ion coincidence measurement for ^{6}He decay

Y. S. Bagdasarova, K. Bailey*, X. Fléchard†, A. García, R. Hong, A. Knecht‡, A. Leredde*, E. Liénard†, P. Müller*, O. Naviliat-Cuncic§, T. P. O'Connor*, M. Sternberg, D. W. Storm, H. E. Swanson, F. Wauters, and D. W. Zumwalt

We performed several experiments from October 2014 to February 2015, taking triple-coincidence data (scintillator-multiwire proportional chamber-microchannel plate three-fold trigger) from laser-trapped ^{6}He atoms. The data rate was improved from $\sim$0.2 Hz in Oct. 2014 to $\sim$0.45 Hz in Feb. 2015. In this section, we present spectra for the ^{6}Li ion time-of-flight (TOF), the reconstructed Q-value, etc., based on the data taken in late Feb. 2015. These spectra gave us many insights on how to improve this experiment and achieve a 1% measurement of the β-ν correlation.

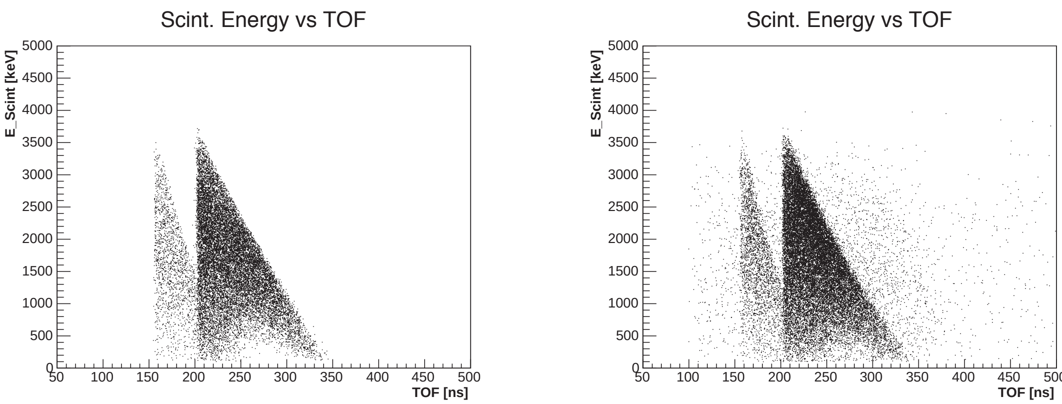

Figure 3.5-1. *Left:* 2D plot of β energy and recoil TOF with a cut on Q-Value from 2977 keV to 4043 keV. *Right:* 2D plot of β energy and recoil TOF without the Q-Value cut.

In Fig. 3.5-1, we show the scatter plot of the β-particle energy read by the scintillator-PMT assembly versus the recoil ion TOF, with and without the Q-Value cut. The two triangle regions correspond to charge states 1 and 2 of the recoil ions. Outside these triangles, events are not kinematically allowed so those events are either from untrapped ^{6}He atoms or from β-particle scattering before the detector. We reconstructed the momenta of the β-particle and the recoil ion using all data taken in the experiment, the trap position, the position and energy of the β-particle, the position of the detected recoil ion, the electric field strength, and the TOF of the recoil ion. The momentum of the anti neutrino is calculated through momentum conservation because the initial momentum of the ultra-cold ^{6}He atom can be neglected. Thus the Q-value of the ^{6}He decay is reconstructed by adding the β-energy and antineutrino energy. The Q-value spectra for the two charge states are shown in Fig. 3.5-2. We fit each Q-value peaks to a Gaussian distribution and cut the events 3 σ or farther away

*Physics Division, Argonne National Laboratory, Argonne, IL.
†LPC-Caen, ENSICAEN, Université de Caen, Caen, France.
‡Paul Scherrer Institute, Villigen, Switzerland.
§Department of Physics and Astronomy and National Superconducting Cyclotron Laboratory, Michigan State University, East Lansing, MI.

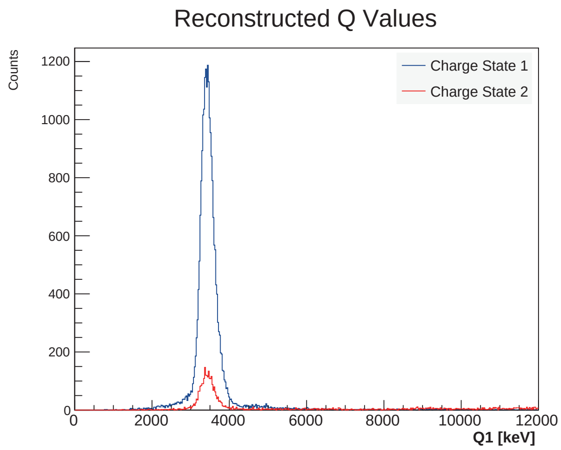

Figure 3.5-2. Q-value reconstruction, using charge state 1 (blue) and charge state 2 (red).

from the centroid. In this way, we removed $\sim$60% of the events from untrapped ^{6}He and from β scattering. Eventually, we achieved a 20:1 signal-to-background ratio.

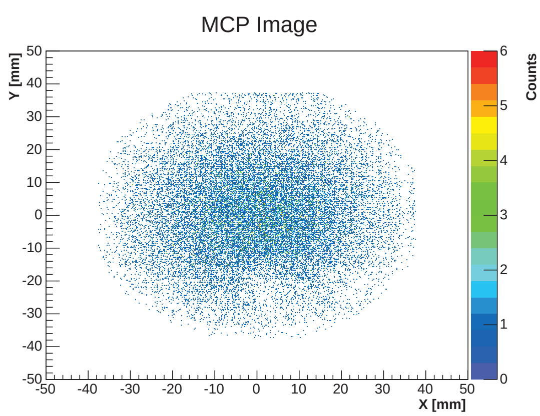

Figure 3.5-3. Position spectrum of the recoil ions hitting on the MCP. In the region near (0,-20) the lack of events is due to the efficiency non-uniformity.

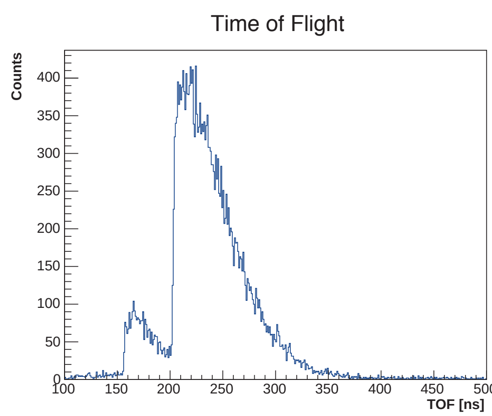

Figure 3.5-4. TOF spectrum of the recoil ions.

We observed non-uniform efficiency of the recoil-ion detector, a micro-channel plate (MCP), as is shown in Fig. 3.5-3. The shape of the TOF spectrum shown in Fig. 3.5-4 is very sensitive to parameters like the MCP efficiency map, the trap-to-MCP distance, the size of the trap, and the timing resolution. In order to have a high-precision measurement of the β-ν angular correlation coefficient $a_{\beta\nu}$, all these effects need to be accounted for very well. More efforts will be dedicated to solving these issues by the summer of 2015 and another data-taking run, aiming at a 1% measurement of $a_{\beta\nu}$, is scheduled around the beginning of June 2015.

3.6 Cyclotron radiation emission spectroscopy: an alternate approach to measuring the Fierz interference coefficient

Y. S. Bagdasarova, A. García, A. Hillman, A. Leredde†, P. Müller†, M. G. Sternberg, H. E. Swanson, and F. Wauters

The $\beta - \nu$ correlation coefficient $a_{\beta\nu}$ is dependent *quadratically* on the ratio of tensor couplings to axial-vector couplings without regard for the chirality of the interacting particles. As a result, improving limits on tensor currents by an order of magnitude requires two orders of magnitude of improvement on the measurement of $a_{\beta\nu}$. In contrast, the Fierz interference term, b, has a *linear* dependence, though it is only sensitive to couplings to left-handed neutrinos. While b is the more sensitive of the two parameters, $a_{\beta\nu}$ provides more robust constraints and is thus complementary data. The Fierz term can be directly determined through a precise measurement of the β spectrum in nuclear β decay, though energy-dependent systematic effects such as β scattering and detector response have made such measurements extremely challenging using conventional experimental techniques.

The current limit on b for pure Gamow-Teller transitions is[1] $b < 1.4 \cdot 10^{-2}$. Several groups have stated goals[2,3] to measure b with sensitivities below $5 \cdot 10^{-3}$. However, none of these programs have demonstrated how they will control systematic uncertainties at the sub-percent level, particularly those arising from β scattering and detector response. Achieving an uncertainty of $\delta b = 1 \cdot 10^{-3}$ would require a precision of 10^{-4} on the linear component of a detector's energy calibration as well as accurate modeling of the detector line shape across the entire energy spectrum. Meanwhile, β scattering poses an inescapable challenge for any detector that relies on an electron interacting with bulk material. Such experiments necessarily rely on simulations of low-energy electrons interacting with matter using packages like PENELOPE or GEANT with estimated uncertainties of order 10%[4]. This makes the goal of a sub-percent b measurement by conventional techniques daunting, and future prospects of achieving uncertainties below 10^{-3} seem unrealistic.

Cyclotron radiation emission spectroscopy (CRES)[5] offers a fundamentally new approach to measuring β-spectra that bypasses the conventional challenges associated with β scattering and detector response. The technique relies on the fact that a charged particle in a uniform magnetic field, B, emits radiation at the cyclotron frequency $\omega_c = qB/(\gamma m)$, where q is the charge of the particle, γ is the relativistic Lorentz factor, and m is the particle's rest mass. By measuring the cyclotron frequency of the radiation emitted from an electron in a known magnetic field, one can determine γ and thus the kinetic energy of the electron, free from the effects of β scattering. The technique has recently been demonstrated by the Project

†Physics Division, Argonne National Laboratory, Argonne, IL.

[1] F. Wauters, A. García, and R. Hong, Phys. Rev. C **89**, 025501 (2014).
[2] D. Počanić *et al.*, Nucl. Instrum. Meth. A **611**, 211 (2009).
[3] X. Wang, G. Konrad, and H. Abele, Nucl. Instrum. Meth. A **701**, 254 (2013).
[4] S. A. Hoedl, *Novel Proton Detectors, Ultra-Cold Neutron Decay and Electron Backscatter*, Ph.D. thesis, Princeton University (2003).
[5] D. Asner *et al.*, Phys. Rev. Lett. **114**, 162501 (2015).

8 collaboration, achieving 15 eV full width half maximum (FWHM) resolution at energies ranging from 17 keV to 32 keV with metastable ^{83m}Kr conversion electrons confined within a magnetic bottle[5].

CRES has a demonstrated energy resolution orders of magnitude better than the typical resolution used in measuring β-decay spectra in the 100 keV to MeV range. As a result, systematic uncertainties stemming from the characteristics of detector response, such as lineshape and linearity, that contribute significantly to measurements using conventional detectors are greatly reduced and simplified using CRES. For example, determining the resolution and centroid of an asymetric lineshape to within 10 eV from a detector with a nominal energy resolution of several keV requires immense effort and pushes the boundaries of modern experimental techniques. However, with a nominal resolution of 20 eV, this is a near trivial task. Monte Carlo simulations of β spectra from ^{6}He using lineshapes modeled from Project 8 data show that even a factor-of-two change in the resolution has a negligible impact on b at the level of 10^{-3}. Furthermore, because the technique relies on measurements of frequencies, better yet the ratios of frequencies, the linearity of the measurement can be calibrated against commercially available frequency standards which routinely achieve ppm accuracy. Motivated by the advantages in overcoming limitations from β scattering and detector response, we explore the potential for using CRES for a precision measurement of b.

There is no fundamental reason why CRES cannot be adapted to measure the continuous spectra of higher-energy electrons. In fact, the radiated power P rises rapidly with energy according to the Larmor formula

$$P = \frac{1}{4\pi\epsilon_0}\frac{2}{3}\frac{q^4}{m^2 c}B^2(\gamma^2 - 1)\sin^2\theta \tag{1}$$

where ϵ_0 is the permeability of free space, c is the speed of light, and θ is the angle between the electron momentum and the magnetic field. As a result, one expects better signal to noise for higher energy electrons and larger magnetic fields. The current signal-to-noise ratio for Project 8 is about 4:1 for 30-keV electrons radiating $\sim$1 fW in a 1-Tesla field, using amplifiers with a noise temperature of 100 K. An experiment performed in a 2-Tesla magnetic field with a lower threshold of 100 keV, and using amplifiers with a 10 K noise temperature (within the specifications of the current Project 8 first-stage amplifier), could expect more than 2 orders of magnitude gain in signal to noise. With a signal-to-noise ratio well above 100:1, the likelihood of misidentifying electrons, even with fluctuations in the noise floor as large as an order of magnitude, would be well below 10^{-4} and thus of little concern to a measurement of b.

A measurement of b in the pure Gamow-Teller β decay of ^{6}He would be uniquely adaptable to the CRES technique using a setup similar to that of Project 8, which requires a diffuse gaseous source. ^{6}He is the only nobel gas isotope that undergoes a pure Gamow-Teller decay and it remains gaseous well below 10 K, ideal for operation of low-noise amplifiers and achieving an ultra high-vacuum environment. With demonstrated yields of $2 \cdot 10^{10}$ ^{6}He per second at CENPA[1] and a short half life of $\sim$1 sec, one can readily achieve decay-rate densities

[1] A. Knecht *et al.*, AIP Conf. Proc. **1560**, 636 (2013).

of 10^7 decays per cm^3. A small-scale experiment similar in size to Project 8, with an effective trap volume of 10 mm^3, and a trapping efficiency of 1%, could anticipate a detection rate of 10 kHz. At this rate, one could acquire the 10^8 events required to achieve a statistical uncertainty of $\delta b = 1 \cdot 10^{-3}$ within 2 days. A larger-scale experiment with a trapping volume of 0.1 cm^3 could reach a statistical uncertainty of 10^{-4} within 20 days.

There are a number of experimental challenges in adapting CRES to precisely measure the ^{6}He β spectrum that are currently being investigated, such as dealing with high data rates over a large bandwidth and understanding the systematic effects associated with the effective trap volume, which changes with the cyclotron radius of the β particle. Thus far, nothing appears insurmountable. In the case of systematic errors associated with the effective trap volume, one can directly measure the effective volume as a function of cyclotron radius using a mono-energetic electron source of known strength at different magnetic field settings.

Most of the experimental techniques required to perform a sub-1% measurement of b in the ^{6}He system have already been demonstrated by the Project 8 collaboration. Such a measurement would provide the most stringent direct limit on left-handed tensor currents and leapfrog the experimental challenges associated with β scattering and detector response that have limited progress thus far.

3.7 Recent upgrades and achievements of the ^{6}He laser setup

Y. S. Bagdasarova, K. Bailey*, X. Fléchard†, A. García, R. Hong, A. Knecht, A. Leredde*, E. Liénard†, P. Müller*, O. Naviliat-Cuncic‡, T. P. O'Connor*, M. Sternberg, D. W. Storm, H. E. Swanson, F. Wauters, and D. W. Zumwalt

After the first observation of β-recoil ion coincidences from laser-trapped ^{6}He in November 2013, last year's upgrades have been focused on two major goals. First, increase the trapping efficiency in order to get a detection rate high enough to accumulate the statistics needed for a 1% measurement of $a_{\beta\nu}$ in about a week. Second, study and reduce our systematic errors based on experimental data and compare them to our simulations. In this section, we will discuss the improvements to the trapping efficiency and some upgrades of our detection chamber.

Laser system: As described in the previous annual report[1], trapping helium atoms first requires excitation to their metastable state $2^3\mathrm{S}_1$. This excitation is achieved when the helium atoms pass through a plasma sustained by a RF electric field and a high xenon pressure controlled by a leak valve. Our trapping efficiency is currently limited because of this process which, once optimized, excites only a fraction of $\sim 10^{-5}$ of the initial He flux.

*Physics Division, Argonne National Laboratory, Argonne, IL.
†LPC-Caen, ENSICAEN, Université de Caen, Caen, France.
‡Department of Physics and Astronomy and National Superconducting Cyclotron Laboratory, Michigan State University, East Lansing, MI.

[1]CENPA Annual Report, University of Washington (2014) p. 46.

As a brief reminder, the excited atoms are then slowed down from their initial Maxwell-Boltzmann velocity distribution by a Zeeman slower which has a capture velocity of about 900 m/s. A significant number of atoms have velocities above this capture velocity and one can try to pre-cool them to increase the overall trapping efficiency. This is achieved by cooling the ceramic tube surrounding the discharge. The He atoms thermalize by colliding with the walls and a larger fraction of the distribution can be trapped. A new discharge source with a better thermal coupling between the liquid nitrogen reservoir and the ceramic tube has been installed. The heat transport is now ensured by a copper conductor in which the ceramic tube is clamped. As compared to the previous discharge source, the efficiency has increased by more than a factor of 2. In this new version, two thermocouples and two heaters have also been added in order to control the temperature and prevent the xenon from freezing out on the cold finger or on the discharge tube. The lowest temperature measured near the discharge tube is -180° C and results in an increase of the trapping efficiency by more than a factor of 4 when the cooling is turned on. This gain is consistent with what is expected from the velocity distribution shift. Finally, a trapping efficiency as high as 1.25×10^{-7} has been measured.

When trapping ^{6}He, the combination of the production rate ($\sim 10^{10}$), the trapping efficiency ($\sim 10^{-7}$) and the lifetime of the trap (on the order of a few seconds) results in a trap size of $\sim$1000 atoms. The fluorescence signal from such a small trap is too low compared to the background coming from the diffusion of the trapping lasers and does not allow a detection of the trap. An imaging setup based on a different transition is used in this case and has recently been upgraded to reduce the detection threshold. The transition used is $2^3P_2 \to 3^1S_0$, at 706 nm, to which the detectors are more sensitive than the 1083 nm light. Moreover, the background can be significantly reduced since this laser beam doesn't need to be larger than the trap size and propagates only on one axis. After improving the lock setup of the laser diode and carefully aligning the detection setup, the detection threshold for a signal-to-noise ratio of 1:1 went down to 5 atoms. The signal obtained for a few hundred atoms is large enough that the trap parameters can now be optimized directly on the ^{6}He fluorescence signal. In February 2015, up to 1400 atoms have been detected in the first MOT.

Recently, a new idea has been developed and is now being tested to increase the transfer efficiency between the two MOTs. When pushing the trapped atoms from the first to the second MOT, the trapping lasers have to be turned off, which leads to a free ballistic expansion of the atomic cloud as it moves to the detection chamber. The expansion of the cloud can be related to its initial temperature by the following formula:

$$T = \frac{m}{4k_B}(\frac{\omega(t)}{t})^2 \tag{1}$$

where m is the mass of the trapped helium atoms, ω the width of the gaussian distribution of the trap, k_B the Boltzmann constant and t the time after after switching off the lasers. Currently, only 30% of the first trap can be recaptured in the second MOT. Radial confinement could in principle help increase the transfer efficiency to close to 100%. The idea is to generate a 2-dimensional dipole trap out of a blue-detuned Laguerre-Gauss laser beam. Dipole traps rely on the complex polarizability of the atomic transition considered. From the interaction between an induced dipole and the oscillating electric field, one can calculate the

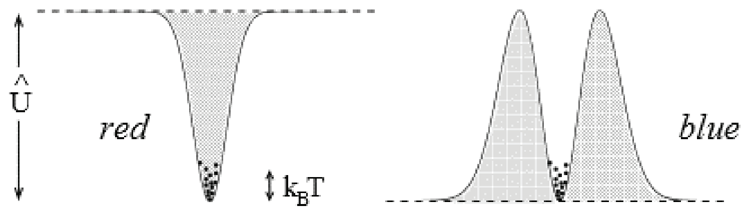

Figure 3.7-1. 1-D intensity profile required for the radial confinement of atoms with a red- (*Left*) or blue- (*Right*) detuned dipole trap.

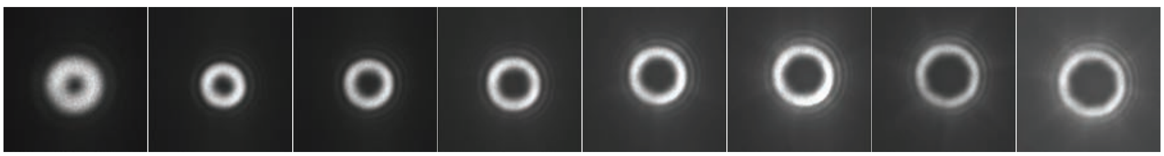

Figure 3.7-2. From left to right, pictures of the LG beams obtained with a VPP with topological charges going from 1 to 8.

depth of the potential as a function of the frequency of the laser ω and the position dependent intensity $I(\vec{r})$:

$$U(\omega, \vec{r}) = \frac{3\pi c^2}{2\omega_0^3}(\frac{\Gamma}{\omega_0 - \omega} + \frac{\Gamma}{\omega_0 + \omega})I(\vec{r}) \tag{2}$$

where c is the speed of light in vacuum, ω_0 is the resonant frequency of the transition considered and Γ is the natural width of the transition. The potential for a red-detuned beam is attractive whereas the one for a blue-detuned beam is repulsive. In the first case, the atoms will be attracted towards the high-intensity region and in the second case, they will be repelled from it. As shown in Fig. 3.7-1, the intensity profile needed for a radial confinement with a red- or a blue-detuned beam is different. Another important characteristic of these traps is the scattering rate. A high intensity is required to get a deep potential and confine the fastest atoms. But as the intensity increases, the scattering rate increases as well and the atoms are heated. Two solutions can be combined to avoid this effect. First, a blue-detuned trap should be favored as the atoms are confined in the low-intensity region. Second, the detuning ($\delta = \omega_0 - \omega$) should be increased as much as possible since the depth of the potential goes as $U \propto I/\delta$ whereas the scattering rate goes as $R \propto I/\delta^2$. We recently achieved the generation of a Laguerre-Gauss (LG) beam, by using a Vortex Phase Plate (VPP), which presents the right intensity profile for a blue-detuned dipole trap. The VPP induces a phase delay as a function of the azimuthal angle. The obtained interference pattern creates a phase singularity along the beam axis where the intensity becomes null. Laguerre-Gauss beams can have different topological charges, i.e. the number of 0 to 2π phase periods when doing a full revolution around the beam axis. The VPP used for the ^{6}He experiment has 8 different patterns which can generate LG beams with topological charges from 1 to 8. Fig. 3.7-2 shows the different intensity profiles obtained with the 1083-nm laser beam and the 8 different topological charges. In the case of a 1 mK MOT, a 1-mm-waist LG beam with 850 MHz detuning and a power of 2.5 W should ensure the radial confinement of the atoms during the transfer. The setup is ready to be tested and results for the transfer efficiency will be available soon.

Detection chamber: Upgrades have also been made to the detection chamber in order to improve the detection efficiency and reduce systematic effects. Major work has been realized on the vacuum system. The roughing line from the discharge chamber, where most of the ^{6}He is pumped away, has been separated from the roughing line of the two MOT chambers to prevent back-streaming of ^{6}He into the detection chamber. Moreover, an extra 50 l/s turbomolecular pump has been added to back up the first pump in the detection chamber. A getter pump has also been added in this chamber. Finally, the whole electrode assembly of our detection setup has been carefully cleaned and baked to reduce the outgassing rate. With all these upgrades, the pressure is now lower than 1×10^{-9} Torr, the trap lifetime has increased to $\sim$2.8 s and the β-recoil ion coincidence rate from untrapped ^{6}He has been reduced by more than an order of magnitude.

Recently, a bypass from the discharge chamber to the detection chamber (between the main turbomolecular pump and the back-up pump") has been added to deliberately flood the detection chamber with untrapped ^{6}He atoms and study the background properties with high-statistics samples.

In the near future, one last upgrade will be made. Re-circulation of the ^{6}He through the discharge should help us increase the trapping efficiency by a factor of 3, as it has been observed in the past. Ultimately, these modifications should result in a β-recoil ion coincidence rate from trapped atoms on the order of 2-3 Hz and a background rate lower than 0.01 Hz.

4 Precision muon physics

4.1 Overview of the muon physics program

L. P. Alonzi*, J. D. Crnkovic†, M. Fertl, A. T. Fienberg, A. García, F. E. Gray‡, N. S. Froemming, D. W. Hertzog, P. Kammel, J. Kaspar, K. S. Khaw, M. H. Murray, R. E. Osofsky, D. J. Prindle, R. A. Ryan, M. W. Smith, H. E. Swanson, and F. Wauters

The Precision Muon Group is involved in fundamental experiments that determine Standard-Model parameters or low-energy effective-field-theory constants, or provide sensitive tests for new physics. With strong CENPA support, the group has carried out a significant number of hardware development projects and has led several important data-taking periods. Our MuSun experiment completed a very successful physics run at PSI. Our final calorimeter prototypes for $g-2$ were tested at SLAC. We developed new pulsed nuclear magnetic resonance (NMR) probes, electronics, and the data acquisition system necessary for the magnetic-field measurements in $g-2$. A wide range of simulation efforts are ongoing, as are analysis efforts by several Ph.D. students in the MuSun project. A number of physics, instrumentation, and review articles have been published this year, with lead authors from our group. Highlights of our activities are described in the series of reports that follow this introduction. Briefly, we note:

- We completed the analysis of the formation rate of muonic hydrogen molecules—the thesis work of S. Knaack—and published the final result in Phys. Rev. C.[1] The paper describes a key correction needed to reduce the uncertainties in the MuCap determination of g_P, the weak-pseudoscalar coupling of the proton, a result described in a previous Annual Report[2]. Although the MuCap technique employs a low-density, active hydrogen target to suppress $pp\mu$ formation, the unprecedented precision of this experiment requires improving the experimental knowledge of the formation rate $\lambda_{pp\mu}$ in order to apply a small correction to the data that leads to the g_P extrapolation.
- Our MuSun experiment aims to determine the muon capture rate in deuterium to 1.5 %. A well-measured $\mu^- + \mathrm{d} \rightarrow \nu_\mu + \mathrm{n} + \mathrm{n}$ process will provide a clean determination of the low-energy constant arising in the effective-field-theory description of the two-nucleon weak interaction, which is relevant for fundamental astrophysics reactions, such as pp fusion and the neutrino breakup reactions in the SNO experiment. Central to the experimental method is a high-resolution time-projection chamber (TPC), filled with ultra-pure gaseous deuterium at cryogenic conditions, which serves as an active target. With major support from the CENPA technical staff, the TPC was rebuilt with high-Z materials to absorb stray muons, and the newly designed cryo-amplifiers[3]

*Presently at University of Virginia, Charlottesville, VA.
†Presently at Brookhaven National Laboratory, Upton, NY.
‡Sabbatical visitor, Regis University, Denver, CO.

[1] V. Andreev, *et al.* Phys. Rev. C, in press (2015).
[2] CENPA Annual Report, University of Washington (2013) p. 66.
[3] R. Ryan, *et al.* J. INST **9**, P07029 (2014).

were fully deployed to increase the TPC energy resolution. The excellent resolution enabled discrimination between signals from muon-catalyzed fusion and muon capture on chemical impurities. These improvements are crucial to the success of the experiment. In 2014, we completed a 3-month data-taking run in which 40% of the final statistics were obtained. The next production run is scheduled in 2015. No major changes are anticipated to the setup.

- One of the strongest hints of new physics is the persistent $> 3\sigma$ difference between the measurement and Standard-Model prediction for the muon anomalous magnetic moment, $a_\mu = (g-2)/2$. Both are known to $\sim$0.5-ppm precision. We co-led the E989 proposal to mount a next-generation muon $g-2$ experiment with a factor-of-4 improved overall precision goal. In 2014, the superconducting storage ring coils and steel yokes and pole pieces were delivered to the newly completed MC-1 building on the Fermilab Muon Campus. The assembly of the these components into the storage ring magnet is now complete, with cooldown and power-on scheduled for June, 2015. We then enter a nearly-year long period of shimming to create the required high-uniformity magnetic field. E. Swanson, Deputy Team Leader of the team, won a Fermilab Intensity Frontier Fellowship which will permit him to spend considerable time at the laboratory leading our UW field team's efforts there. Our responsibilities include the development and fabrication of the suite of NMR probes that will monitor the field, the data-acquisition system, and many of the pulsed-NMR custom electronics modules. We continue to be involved in the simulation of muon injection and storage into the ring and have complemented that activity with a new design of beam monitoring imaging detectors that will be positioned along the incoming corridor surrounding the inflector magnet. Finally, our funded NSF MRI proposal is being used to support the design and fabrication of the 24 electromagnetic calorimeter stations and their readout systems. We led a test beam run at SLAC in 2014. The results are published in NIM[1]. The $g-2$ experiment remains on schedule to begin data taking in 2017.

g-2

4.2 Overview of the $g-2$ experiment

L. P. Alonzi*, J. D. Crnkovic†, M. Fertl, A. T. Fienberg, A. García, N. S. Froemming, D. W. Hertzog, P. Kammel, J. Kaspar, K. S. Khaw, R. E. Osofsky, M. W. Smith, and H. E. Swanson

The anomalous magnetic moment of the muon, $a_\mu = (g-2)/2$, can be calculated and measured to sub-ppm precision. The comparison between theory and experiment continues to be one of the most sensitive challenges to the completeness of the Standard Model (SM). The

*Presently at University of Virginia, Charlottesville, VA.
†Presently at Brookhaven National Laboratory, Upton, NY.

[1] A. Fienberg, *et al.* Nucl. Instrum. Meth. **A783**, 12 (2015).

E821 measurement at Brookhaven National Lab (BNL)[1] and the SM theory have uncertainties of 0.54 ppm and 0.42 ppm, respectively. The difference between experiment and theory (Exp − SM) is $(287 \pm 80) \times 10^{-11}$, or a $3.6\,\sigma$ significance[1,2,3]. The previous measurement is highly cited and the discrepancy generates considerable new physics speculation, from supersymmetry (SUSY) to Dark Photons and beyond. To this end we co-lead the development of a next-generation $g-2$ experiment (E989) which has been approved at Fermilab with a precision goal of 0.14 ppm.

The Standard Model uncertainty is dominated by quantum loops involving hadrons, specifically the hadronic vacuum polarization (HVP) and hadronic light-by-light (HLbL) scattering. The relative uncertainties are 0.35 ppm and 0.22 ppm, respectively. The HVP contribution is obtained from $e^+e^- \to$ hadrons cross sections. The optical theorem, cross sections, and a dispersion relation are used to accurately determine a_μ(HVP). Low-energy cross sections are obtained from experiment and their uncertainty drives the overall error on the HVP contribution. A reduction to a relative uncertainty of ~ 0.25 ppm on the time scale of a new $g-2$ experiment is expected based on new experiments at BES and Novosibirsk. Of great importance is the less well-known, but much smaller, HLbL contribution, which cannot be directly obtained from measurements. Hadronic models, lattice QCD, and more recently a data-driven approach are all being developed. In a sequence of community meetings, including the 2011 INT Workshop we sponsored, the theoretical effort has intensified[4] and we are confident of an improved HLbL evaluation around the time of our first experimental result.

The muon anomaly is proportional to the ratio ω_a/ω_p, where ω_a is the anomalous precession frequency of the muon spin in a magnetic field and ω_p is a measure of that average magnetic field carried out using proton nuclear magnetic resonance (NMR). Both frequencies must be determined to 0.1 ppm, including systematic uncertainties. The statistics required exceed those obtained at Brookhaven by a factor of 20 and the new experimental plan can realize this in 1.5 years of data taking. Our UW group is involved in both the ω_a and ω_p measurements and we are designing and building a significant array of hardware tools to carry out the measurements. In addition, we remain involved in aspects of the beam simulations and muon storage fraction optimization. Recently we designed a set of detectors to image the muon beam as it enters the storage ring.

In the past year the experiment as a whole has progressed impressively. The new home of $g-2$ in the MC-1 building is complete (Fig. 4.2-1 *Left*) and is now being used by the Collaboration. The storage ring has been assembled (Fig. 4.2-1 *Right*) and is ready for cooldown and power tests. The Collaboration has grown to include 35 institutions and > 150 collaborators from 8 countries. The work is divided around the generically named Beam, Ring, Field, and Detector Teams. Progress from all four teams has been substantial as we summarize briefly.

---

[1] Muon g-2 Collaboration: G.W. Bennett *et al.*, Phys. Rev. D **73**, 072003 (2006).

[2] K. Hagiwara *et al.*, J. Phys. **G38**, 085003 (2011).

[3] M. Davier *et al.*, Eur. Phys. J. **C71**, 1515 (2011).

[4] See, for example *Hadronic contributions to the muon anomalous magnetic moment Workshop* M. Benayoun *et al.*, arXiv:1407.4021 (2014).

The Beam design includes all of the components—Booster, Recycler, Transfer Lines, Target Station, Decay Beamline, Delivery Ring—that are necessary to create and deliver a bunched, 3.1 GeV/c polarized muon beam, which is purified of background pions and protons. This effort is led by Fermilab accelerator physicists with collaboration members providing some of the modeling. The extensive work involved determines the critical path for completion of the overall experiment.

The Ring Team is responsible for building and operating the storage ring, and they provide the inflector, quadrupoles, and kicker subsystems. They carry out simulations of muon storage and evaluate beam-dynamic systematic uncertainties. UW student N. Froemming—who learned the craft of accelerator physics during a year-long study at Cornell—has modeled, in exquisite detail, the steps involved in storing the muon beam, given all of the subsystem components and their individual field maps. Recently P. Kammel has designed a set of entrance counters—the Inflector Beam Monitoring System—that are needed to image the beam in three distinct places: just upstream of the back-leg hole in the magnet yoke, and just before and after the inflector. We will use variants of the SiPM technology we developed for the calorimeters to read out a grid of scintillating fibers.

The Field Team is responsible for shimming the magnet to ultra-high uniformity using a suite of pulsed NMR probes and an OPERA-based model for predictive adjustments. Once physics data-taking commences the field will be continuously monitored using nearly 400 NMR probes that UW is preparing. We are also in charge of the electronics used to pulse and record the system, and the overall Field Team DAQ (Smith). While originally inheriting the equipment used in E821, it has become apparent that much of the equipment needed to be replaced, repaired, or updated, owing to aging and the lack of spare components. Led by Swanson, we have designed (Fertl) new NMR probes that can be easily tuned and are more robust for wear and tear. The production of 400 of these probes is well underway at this time. As described below, a wide variety of work has been carried out by our team in hardware and in signal-extraction techniques and systematics considerations. Using data obtained in our local magnet test system, we continue to be the collaboration's center for component testing of candidate electronics parts that must be located near the storage ring.

The Detector Team provides the instrumentation to measure the decay positrons and create the characteristic precession signal histograms. Additionally, the team will build specialized trackers to determine beam-storage properties needed for systematic uncertainty targets. The UW group led a six-university consortium proposal to NSF to secure funding for the precession frequency measurement. We are responsible for the electromagnetic calorimeter system, which consists of 24 stations, each having an array of 54 PbF_2 crystals with individual large-area SiPM readouts. The electronics, testing, and mechanical supports are all developed and built at CENPA. At this time, we have received and tested 600 of the 1300 needed crystals and have made the final optimization of the custom electronics that supports the SiPMs. A 2-week-long test run at SLAC in the summer of 2014 featured a 28-element array and a prototype calibration system provided by our Italian partners. The highly successful results were published in NIM. J. Kaspar leads the effort for the UW team. Grad student A. Fienberg analyzed the data from SLAC and is first author on the publication.


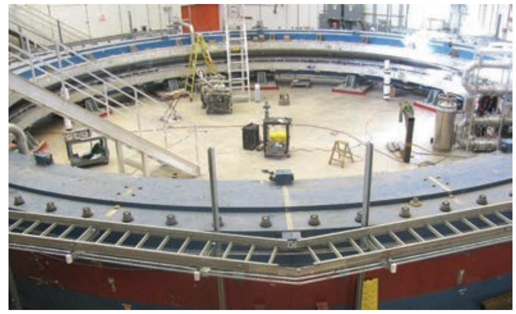

Figure 4.2-1. *Left:* The newly completed, temperature-regulated, MC-1 building on the Muon Campus, which presently houses the $g-2$ experiment. *Right:* Assembly photo of the nearly complete storage ring.

A detailed cost and technical CD2/3a review of the Project was carried out in August, 2014. While strongly positive, the DOE put on hold official approval pending a successful commissioning of the long-idled storage ring. In the interim, the funding to the Project has been relatively unimpeded. The ring will be cooled and powered in May, 2015 and a final CD2/3 review is scheduled for June, 2015. Nine months will then be devoted to shimming the magnet, followed by a period of detector installation and testing in summer 2016. Beam commissioning and the first physics run are scheduled to start in 2017.

4.3 NMR system for precision magnetic field measurement

A. García, M. Fertl, C. Helling, A. Kvam, R. Morris, R. Ortez, R. E. Osofsky, D. A. Peterson, E. A. Shaw, M. W. Smith, H. E. Swanson, and T. D. Van Wechel

At Fermilab the ring assembly is nearly complete and a high priority has been placed on activities to demonstrate that the magnet can be cooled and brought to its nominal field of 1.45 Tesla. Achieving this milestone is a necessary condition for the DOE's CD2/3 review and funding of the implementation phase of the project. Once powered, the field will be shimmed over the next 9 months to achieve the required homogeneity in the pole gap. Much of the effort of the UW field team over this past year was to prepare for this shimming phase.

We have completed the re-design of the NMR probes and our shops have produced more than enough parts to supply a new generation of probes for the shimming effort. We have in place procedures for assembling, quality-assurance testing and documenting the measured characteristics of each probe. We currently have over 50 working probes and expect to have all 400 ready for installation at Fermilab by year's end. All 20 E821 multiplexers and NIM modules used to generate and mix down free-induction decay (FID) signals (pulser/mixers) have been evaluated for performance. About half of the multiplexers had some channel failures and some components are no longer available as the technology is almost 20 years old. A set of fully functioning multiplexers and NIM modules has been set aside and will be sent to Fermilab for the shimming measurements. We have designed a functional replacement for the multiplexer using current technologies. A prototype of this design has been built and tested, leading to design modifications that should greatly enhance its performance. A new, improved prototype is under construction.

E821 pulser/mixers were designed to drive hardware that counted the number of zero crossings. These output channels are very nonlinear and as described below cannot be used for software extraction of the precession frequency. A second output is more linear but signal amplitudes vary by more than a factor of 2 from module to module. As the technology used is also about 20 years old, we have designed a functional replacement and completed a prototype which is currently under evaluation. Whereas field measurement extends technology from the previous $g-2$ experiment (E821), a new method for extracting field information from the probe electronics was pioneered here at the University of Washington. Waveform digitizers capture the mixed-down FIDs and fast Fourier transform (FFT)-based software algorithms process these data to obtain field values. Simulations show nearly an order of magnitude greater precision using these methods when compared with counting zero crossings.

There has been good progress on the data-acquisition system. It is PC-based and uses the MIDAS framework developed at the Paul Scherrer Institute (PSI). MIDAS is also used throughout the collaboration for data acquisition. Our system is fully functional, capable of addressing probe multiplexers, initiating FIDs and acquiring the resulting waveforms. Earlier in the year we hosted a workshop with collaborators from Argonne and Fermilab to determine the data-acquisition environment needed for the upcoming shimming work. This required integrating NMR field data with data from other MIDAS systems that measure azimuthal positions of the NMR probe matrix and environmental temperatures around the ring. A graphical user interface showing trends in the data was also developed. A functioning composite system now exists.

The storage-ring magnet will be shimmed before the installation of calorimeters and beam monitors is completed. It is important that materials used in the fabrication of any device placed close to the muon storage volume have a minimal influence on the field. NMR probes placed in the UW test magnet field are sensitive to sub-ppm changes in its value. We have automated a scanning system which moves samples of materials from close proximity to the probes to some distance away and, from the dependence on distance, determines the effective dipole strength of the sample. We have provided this measurement as a service to the collaboration.

4.4 PbF_2 calorimeter with SiPM readout

L. P. Alonzi[*], J. F. Amsbaugh, A. T. Fienberg, G. C. Harper[†], D. W. Hertzog, J. Kaspar, D. A. Peterson, G. J. Plunkett, W. Shaffer, M. W. Smith, T. D. Van Wechel, and K. B. Wall

After a muon decays into a positron and a neutrino, the positron has insufficient energy to fly along the magic orbit in the ring. It curls inward where a lead fluoride calorimeter read out by silicon photo-multipliers (SiPMs) waits to report on its energy and the hit time. This year, hundreds of the crystals destined for use in the $g-2$ experiment have arrived at University of Washington and been subjected to meticulous quality control procedures

[*]Presently at University of Virginia, Charlottesville, VA.
[†]Retired August, 2014.

(Sec. 4.18). A prototype calorimeter dark-box performed very well during a calorimeter test run at SLAC; the results of this test were published in Nucl. Instrum. Methods A . Data-analysis techniques were developed to process positron hits and laser calibration data.

The calorimeter is built around a 6×9 array of lead fluoride crystals. Lead fluoride was chosen because of its high density and intrinsically fast temporal response to energy deposition. This fast response comes from the purely Čerenkov radiation generated when a charged particle passes through one of the crystals. The segmentation and fast response both improve the detector's ability to distinguish events that are close together in time (pileup).

Silicon photo-multipliers collect Čerenkov photons emitted by a positron stopping in lead fluoride. Their operation is not disturbed by strong magnetic fields, their performance can be flexibly fine-tuned to match experimental needs, and their dynamic range spans from single counts to many thousands of hits. A pre-amplifier board designed by CENPA engineers delivers very fast pulses in the few-ns range to guarantee excellent pulse separation, stellar pulse fidelity, and optimal signal-to-noise ratio. The pre-amplifier board is based on a concept of a multi-staged transimpedance amplifier. In the first step, current pulses from 4 SiPM channels are added together and converted into voltage pulses in a fixed-gain transimpedance amplifier. In the second stage, the four partial sums are added together using a THS3201 op-amp operated at unity gain in voltage mode. The output stage drives an AC-coupled differential pair of coaxial cables, and is designed using a LMH6881 digitally controlled variable-gain amplifier. The multi-staged design provides a PMT-like pulse width, very high rate tolerance, and excellent gain stability. It has been a very good year for SiPM development. The CENPA pre-amplifier board in many aspects transcends the $g-2$ design.

Lead fluoride crystals and SiPMs are housed in a temperature-controlled calorimeter box. A cooling concept based on pressurized chilled and dried air blowing directly on SiPM boards was successfully tested this year, but the calorimeter team is currently working closely with CENPA engineers to design an even more effective cooling system. The light-tight box is being designed without any feedthroughs to avoid even the slightest impedance mismatch in cable junctions. Signal cables pass through a chicane in the box wall to maximize noise suppression. The calorimeter box sits on a chariot that runs on rails. Base plates and the rails were inherited from the previous experiment. CENPA engineers are designing a chariot which will also be a new home for an electronics rack holding custom digitizers and SiPM bias power supplies. The temperature-controlled box is a key to SiPM gain and energy-scale stability.

SiPM gain stability is a major contributor to the experiment systematics and a laser calibration system will mitigate this problem. While the calibration system is under development in Italy, a mock-up system has been in use for calorimeter development. It consists of a PicoQuant diode laser at 407 nm, a diffuser, and optical fibers feeding laser shots directly into the front face of the crystal. Dedicated laser runs calibrate the energy scale, and shots fired within a run monitor gain stability. Data-analysis techniques based on the statistical properties of laser light distribution were demonstrated to successfully extract the effective number of SiPM pixels fired from digitized traces, and correct for background-noise leakage into the light width as well as possibly disentangling laser fluctuations from the intrinsic

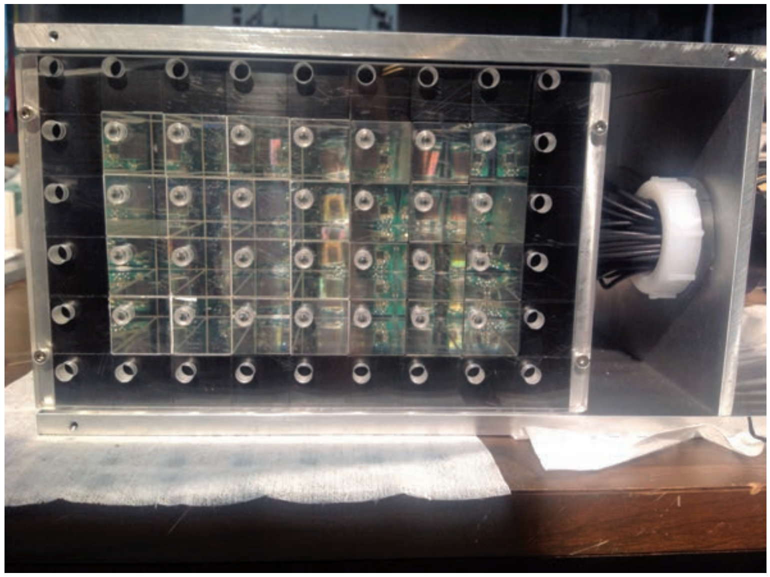

Figure 4.4-1. A prototype $g-2$ calorimeter, tested at SLAC. This test box consisted of a 4×7 PbF_2 crystal array with each crystal coupled to a Hamamatsu SiPM.

SiPM response.

The quality of our calorimeter design was thoroughly tested during a test run at SLAC (Fig. 4.4-1). Details of the test run are covered in a dedicated report (Sec. 4.6). The test run was a success; the calorimeter outperformed design specifications in both energy resolution and long-term gain stability.

As our calorimeter design has been proven, the focus of the team is shifting towards production, systematic error studies, and reconstruction-algorithm development. The systematic-error studies and reconstruction algorithms are highly interconnected. For example, the $g-2$ pileup systematic error depends on how effectively decay positrons can be distinguished based on their hit separation in time and space. GEANT4 simulations and lab tests are underway to test these reconstruction techniques.

4.5 Inflector beam-monitoring system

J. F. Amsbaugh, D. W. Hertzog, P. Kammel, and N. S. Froemming

The muon injection into the g-2 storage ring is one of the most critical and complex elements in the muon delivery concept. The challenges are extensively described in the Muon $g-2$ Technical Design Report (TDR)[1]. The entering muon beam has to pass through strong fringe fields and the narrow inflector apertures (18 mm(W)×56 mm(H)), which results in a mismatch between the transmitted beam phase space and the ring acceptance. Extensive simulations were performed to study the impact of this beam section on the muon storage fraction and betatron oscillation amplitudes in the $g-2$ ring.

[1] J. Grange *et al.* [Muon g-2 Collaboration], arXiv:1501.06858

The Inflector Beam Monitoring System (IBMS) is being designed and constructed at CENPA as the primary diagnostic tool to develop and verify the beam optics tune in the muon injection section. It is also foreseen as a continuous monitor of the beam properties, relevant for detecting systematic problems. This project will be largely funded by the DOE muon $g-2$ project office.

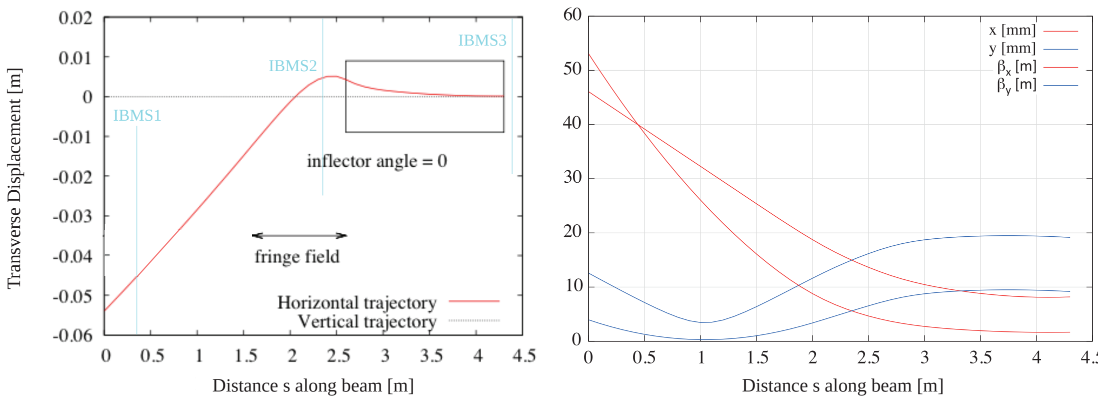

Figure 4.5-1. *Left:* Trajectory through the injection channel. *Right:* Accelerator physics β-functions and 90% beam envelopes for the current beam optics design. According to the simulations these settings maximize transmission and storage. The limiting horizontal aperture is the inflector. The origin of the coordinate system in these plots is 30 cm upstream of the hole in the magnet iron.

The development of the beam center and envelope over the injection region in Fig. 4.5-1 demonstrates the significant transverse beam motion and focusing forces in this region. The transmission and storage fraction η_{store} is highly sensitive to the initial Twiss parameters of the beams, the precise knowledge of the field maps, the inflector tilt angle and the materials traversed by the incoming beam. Downstream of the inflector several other parameters enter, like the kicker field strength and pulse shape, the betatron tunes in the ring and the storage aperture as defined by the collimators and scraping procedure. The positions of the three IBMS detectors are indicated. They will measure the transverse and longitudinal beam properties to allow a systematic comparison with the beam optics model and the observed transmission/storage efficiency. This information is essential for both the initial beam tuning and the final optimization for production running.

The transmission and storage efficiency η_{store} for E821 was significantly below expectations and was not well understood. It was not possible to disentangle the inflector losses from losses induced by the sub-optimal kicker; only the net storage efficiency was measured. A main reason for this deficiency was the insufficient beam monitor in the injection region. Simulations for E989 indicate that the combined action of optimal injection and the new kicker should increase η_{store} nearly four-fold. The IBMS will be essential in achieving this goal, by verifying the optics model and directly measuring the phase space of the beam entering the ring. This information will also constitute an important reality constraint in any effort to develop a new inflector.

The locations of the IMBS detectors are shown in Fig. 4.5-2. Detector 1 and 2 will be

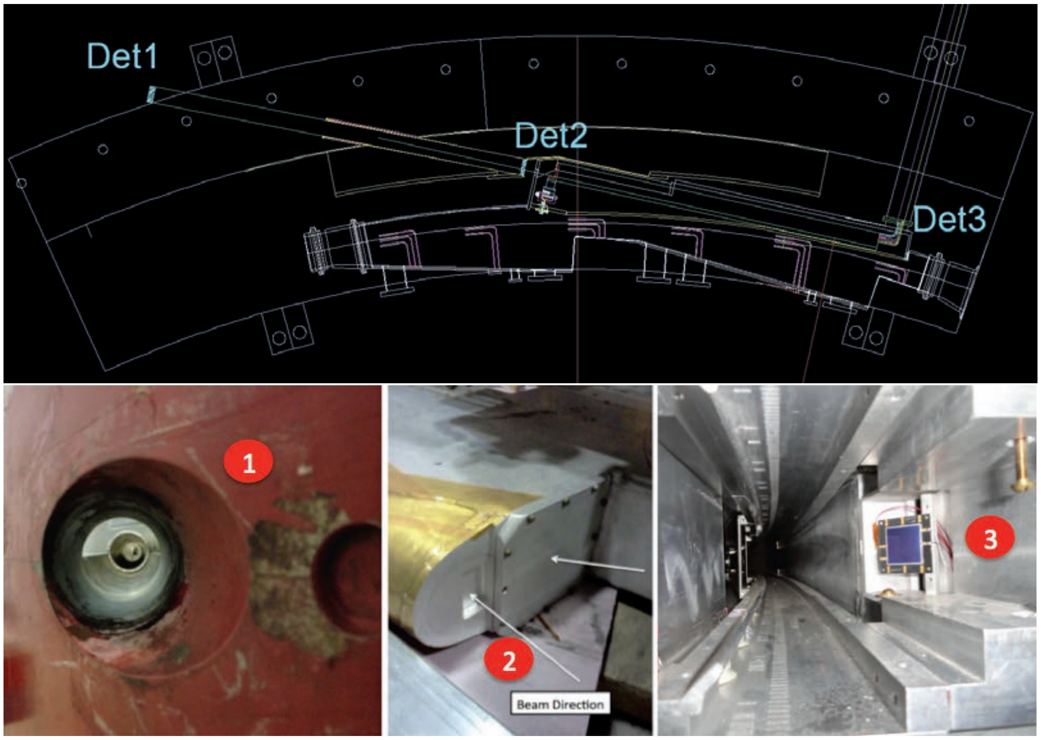

Figure 4.5-2. Detector locations: detector 1 at entrance to yoke hole, detector 2 at entrance of inflector and detector 3 inside ring vacuum close to injection point.

made of two planes of 16 scintillating fibers each, oriented in the horizontal and vertical direction. Simulations show that only vertical fibers are needed for detector 3. Each fiber will be read out by silicon photomultipliers S12571-010P from Hamamatsu. These 1-mm^2-area devices were selected for their large dynamic range (10000 pixels) and speed. All fiber signals will be digitized with CAEN V1742 switched-capacitor digitizers.

Detector 1 will be mounted on a separate stand or fixed to the outer beam entrance hole in the magnet yoke. The positioning of detector 2 is more difficult. While it could be mounted to the inflector entrance flange, this would require the removal of the inflector vacuum chamber for any detector modification, maintenance and repair. Thus we envision a rail system to move the detector in place, starting from the outside hole of the yoke. Because the the size difference between the outer hole and outer cryostat pipe and the misalignment between the two, this construction is challenging. Moreover the space is highly constrained. The current CAD model of the design is shown in Fig. 4.5-3. Detector 2 will be inserted into the yoke hole shown left/bottom in Fig. 4.5-2, then pulled to its nominal position 2.3 m downstream on a miniature aluminum rail. The rails are mounted on several rings. A laser and camera will observe the insertion and verify the position. An encoder will determine the distance on the rail to allow beam monitoring at different positions along the nominal beam trajectory. Detector 3 needs a special construction which ideally contains no metals or currents, which might interfere with the ring field. The old silicon detector shown in the right/bottom panel of Fig. 4.5-2 does not have any segmentation.

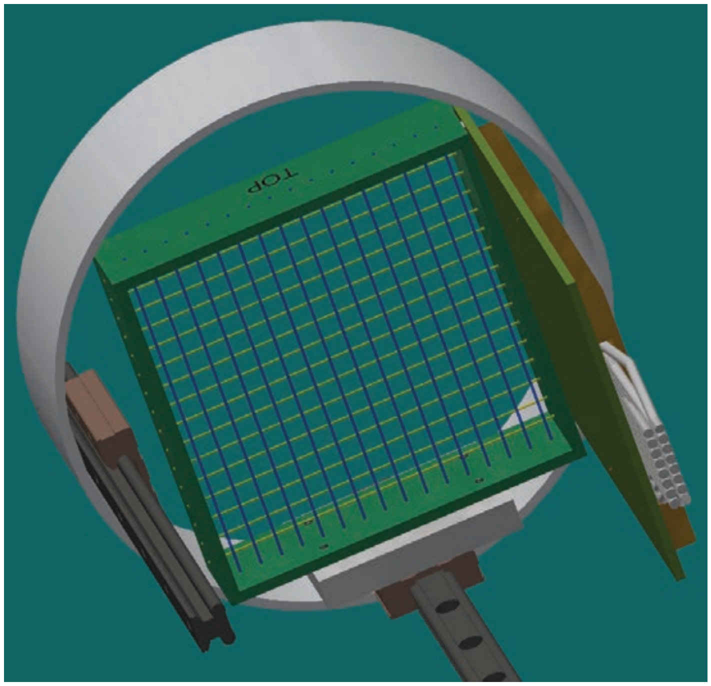

Figure 4.5-3. CAD model of detector 2.

The maximum expected rate is about 2500 maximum-ionizing particle (MIPS)/5ns in a ∅=0.5-mm fiber within an overall pulse of 120 ns. In order to avoid saturation of the SiPM this pixel number should be reduced by a factor of two by light attenuation for the nominal beam rate. At the same time we would like to observe a dynamic range of 50 to cover the transverse and longitudinal intensity variations. In case the beam intensity is 10 times lower during tuning, we would like to also observe these low intensity profiles. This large dynamic range will be covered by inserting neutral density filters between the fiber and SiPM and by measuring the SiPM current with a variable-gain amplifier with a 45-dB range. A prototype electronics has been designed and is currently being tested. After a successful test a compact multichannel layout has to be prepared. The above pixel rate estimates must be verified on a prototype detector, before building the full IBMS.

4.6 Test beam studies of the $g-2$ PbF_2 calorimeter

A. T. Fienberg, D. W. Hertzog, J. Kaspar, and M. W. Smith

In July of 2014, the University of Washington-led $g-2$ calorimeter team once again traveled to SLAC National Accelerator Laboratory's End Station Test Beams facility with a detector prototype. SLAC's test beam facility is ideal for characterizing the $g-2$ calorimeter because of its ability to deliver single electrons in the energy range of interest for the $g-2$ experiment, around 3 GeV. Additionally, the facility provides a remotely movable table on which to place the detector, allowing both investigation of detector response variation with electron impact position and confirmation of the correct relative calibration between detector segments. The beam time also provided an invaluable opportunity to investigate one of the last remaining design questions: whether it is optimal to wrap the PbF_2 crystals in white, diffusive paper or black, absorptive paper. To answer this question, the tested prototype was prepared as a 4×4 array of white-wrapped crystals adjacent to a 4×3 array of black-wrapped crystals. The test beam effort was augmented by the participation of collaborators from over 10 other institutions, both domestic and international.

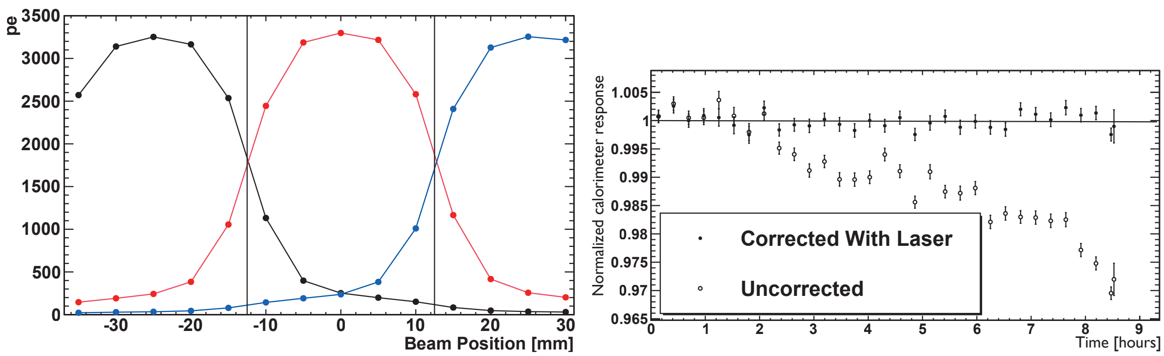

Figure 4.6-1. *Left:* Reconstructed energy in three adjacent crystals as the electron beam is scanned across. The calibration constants obtained from the technique described in the text bring their peaks to the same height; pe stands for photelectrons. *Right:* Reconstructed energy, normalized to 1, from a 3-GeV electron beam firing continually over a 9-hour period. After correction with the laser system, the reconstructed energy is stable at the level of 10^{-4}/hour.

A primary success of the test beam was the demonstrated efficacy of the planned calibration techniques. At the center of the calibration system is a pulsed diode laser, distributed through fiber optics to each crystal, and ultimately each SiPM, individually. A remotely controllable neutral-density filter wheel is placed in the path of the laser beam and used to vary the pulse energy seen by the calorimeter. By observing how the statistical width of the reconstructed energy distribution in each SiPM varies with the mean, one can obtain relative calibration constants for each of the calorimeter segments. In principle, this technique does not rely on each fiber delivering the same amount of light, as long as the light level is low enough that the SiPM responses can be treated as linear. Once relative calibration constants are established, long-term stability is ensured by periodically firing a fixed-energy laser pulse into every segment. Undesired fluctuations in laser pulse energy are corrected for by a suite of dedicated laser monitors. As shown in Fig. 4.6-1, these techniques produced a reconstructed energy that was independent of both time and impact position.

While the energy linearity of the calorimeter was confirmed in previous test-beam experiments, and the energy resolution was shown to exceed the design requirements, the calorimeter team had yet to complete a detailed experimental study of energy resolution behavior as a function of energy and how this behavior differs between white- and black-wrapped crystals. The main contributors to energy resolution are energy leakage fluctuations and photostatistics. Leakage fluctuations are differences in how much energy escapes the calorimeter from one event to the next. According to careful simulation, when all forms of leakage are considered, the leakage fluctuations account for a 1.5% term in the energy resolution σ_E/E. This value is independent of energy in the region of interest, 2–4.5 GeV. Photostatistics contributions arise from the discrete nature of photon detection: the more photons arrive at the SiPM, the smaller the relative width of the detected photon distribution. This contribution is described by a term of the form $\sigma_E/E \propto a/\sqrt{E}$. White-wrapped crystals collect more light than black, so it is in the photostatistics contribution that one expects to find the energy resolution difference between the white- and black-wrapped arrays. This expectation was confirmed at the test beam by varying the incident electron energy between 2 and 4.5 GeV, alternately aiming at the centers of 3×3 clusters of white- and black-wrapped crystals, and fitting the obtained σ_E/E curves to functions of the form $\sqrt{1.5\% + a^2/E}$. The curves from this test are shown in Fig. 4.6-2 with the resulting values being $a_{white} = (3.4 \pm 0.1)\%\sqrt{GeV}$ and $a_{black} = (4.6 \pm 0.3)\%\sqrt{GeV}$.

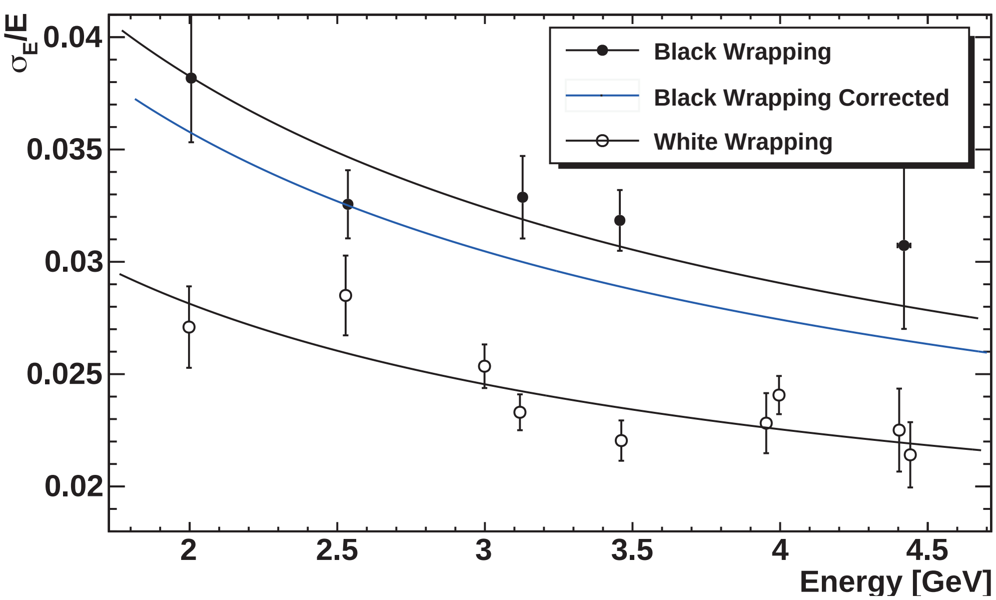

Figure 4.6-2. Energy resolution of 3×3 arrays of PbF_2 crystals with black and white wrappings as a function of energy. Fit functions are of the form $\sigma_E^2/E^2 = (1.5\,\%)^2 + a^2/E$. The blue dashed line is the result of correcting the black-wrapped curve for dead SiPM channels discovered after the fact.

Although white-wrapped crystals yield better energy resolution, black wrapping offers advantages that are more difficult to quantify. These advantages come from the shorter and more consistent SiPM pulse shapes produced by the black-wrapped crystals. Better pulse shapes have the potential to reduce $g-2$ systematic errors. With the successful completion of this test-beam experiment, the calorimeter team has all the data it needs to complete a thorough study of which wrapping choice will result in a more sensitive measurement of $g-2$. This study is planned for the coming months. A more detailed description of the experimental procedures and results from the test-beam experiment are available in our recent NIM publication[1]

[1] A. T. Fienberg *et al.*, Nucl. Instrum. Meth. A. **783**, 12 (2015).

4.7 SiPM pulse shape studies

A. T. Fienberg, D. W. Hertzog, P. Kammel, J. Kaspar, D. A. Peterson, M. W. Smith, and T. D. Van Wechel

Silicon photo-multipliers (SiPMs) collect Čerenkov photons emitted by a positron stopping in lead fluoride crystals sitting in the magnetic field of 1.45 T. Their performance can be flexibly fine-tuned to match experimental needs, and their dynamic range spans from single counts to many thousands of hits. They are non-magnetic, i.e., they can operate in a strong magnetic field, and they do not distort the field, on a 1-ppm level. That makes a SiPM more attractive than a combination of a PMT and a long light guide transporting photons out from the strong magnetic field.

For the $g-2$ experiment, a PMT-like pulse shape, in a few-ns range for multiple thousands of pixels fired, is required for excellent pulse separation to reduce pileup systematics. Further requirements include a large area of a SiPM to collect a significant fraction of photons reaching the $25\times25\,\mathrm{mm}^2$ rear face of a lead fluoride crystal, gain stability both short-term, from pulse to pulse within a muon fill lasting $700\,\mu$s, and long-term, in the course of hours; and fast recovery from complete overload, which might occasionally happen in the inflector region during the muon-beam injection.

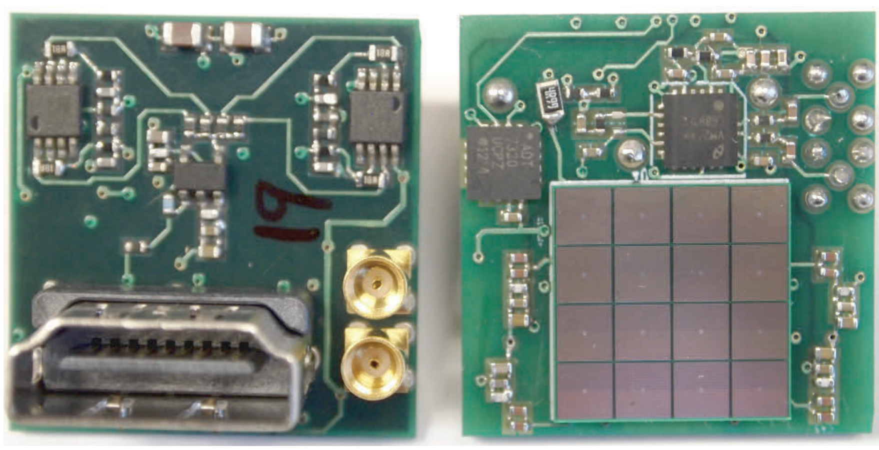

Figure 4.7-1. A baseline prototype of a surface-mount 16-channel SiPM soldered on the amplifier board. The two MMCX connectors correspond to the DC-coupled differential voltage signal out. The common bias voltage in, the board low voltage, and SPI lines to regulate gain are supplied through the HDMI connector.

A pre-amplifier board was designed at CENPA (Fig. 4.7-1) around Hamamtsu S12642-4040PA-50 SiPM featuring 16 independent channels, $12\times12\,\mathrm{mm}^2$ active area, and $50\,\mu$m pixel pitch. A usual electronics design relying on a shunt resistor cannot meet the requirements for pulse shape, and discrete components wouldn't fit in the space-constrained calorimeters. Instead, a novel multi-staged design with a purely current input was developed, i.e., a transimpedance amplifier. In the first step, current pulses from 4 SiPM channels are added together and converted into voltage pulses in a fixed-gain transimpedance amplifier (THS3202, see Fig. 4.7-2). In the second stage, the four partial sums are added together using a THS3201 op-amp operated at unity gain in voltage mode. A change in over-voltage applied to a SiPM affects both quantum efficiency (QE) and gain, if the gain is defined as the charge delivered by a pixel when the pixel fires. To control both QE and gain separately, the output stage amplifier, LMH6881, has a remotely controllable gain. The output stage drives a DC-coupled differential pair of cables. Differential signal with an excellent signal-to-noise ratio can explore the full potential of modern multiple-GSps 12-bit digitizers.

The breakdown voltage of a SiPM is a function of temperature, and therefore the over-voltage, QE, and gain depend on temperature, too. The reason is that the resistance of the quenching resistor connected in series with the diode changes with temperature. The latest generation of SiPM's comes with Ni-based quenching resistors with a temperature coefficient about 5 times lower than the previous generation of products using poly-crystalline silicon resistors. Although the temperature still needs to be stabilized, a stability within 1°C is sufficient. A temperature sensor mounted directly on the amplifier board helps track and correct for temperature fluctuations.

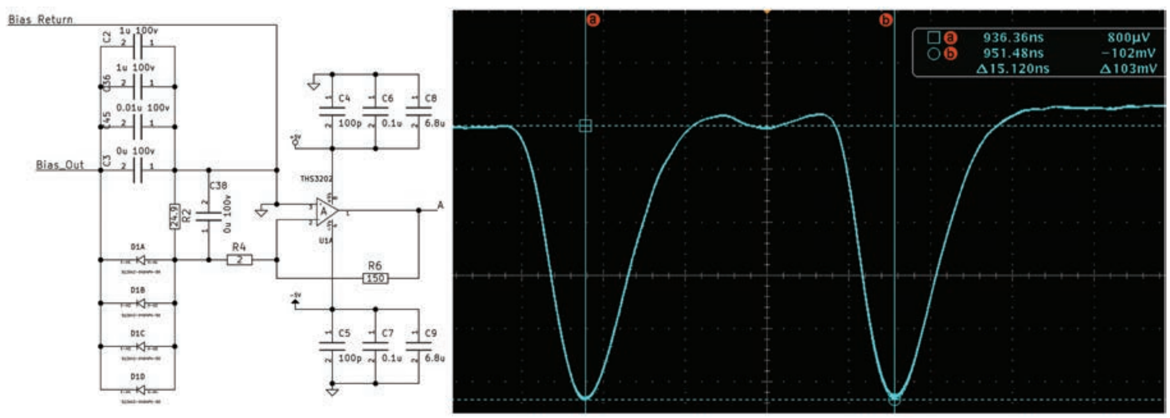

Figure 4.7-2. *Left:* The schematics of the first-stage trans-impedance amplifier. *Right:* The response of the SiPM board to the laser and LED pulses. The setup was used to measure gain changes as a function of load on the ns time scale.

This year we finished the board design, and made 26 prototype boards that underwent a successful beam test run at SLAC and extensive pulse-shape studies. We learned how the width of the pulse scales with the local charge buffer, proved the pulse shape is independent of the load up to 10 MHz, and understood how the QE, gain, and dark current scale with over-voltage. We demonstrated excellent gain stability on multiple time scales.

We gained experience in SiPM electronics design including an optimized SPICE model, and an understanding of how the pulse shape changes with pixel pitch and SiPM size. The experience is being translated into SiPM-based detectors for the inflector-beam monitoring system, the fiber harp detectors, and the veto for the MuSun experiment. This year, we are planning to test the radiation hardness of SiPMs using a strong PuBe source. A paper describing the design and documenting the development will be published.

4.8 Calorimeter simulation studies

A. T. Fienberg, D. W. Hertzog, J. Kaspar, and G. J. Plunkett

This past year featured a collaboration-wide, concerted effort to raise the $g-2$ simulation, based on Geant4 and Fermilab's art framework, to a new level of fidelity. The accurate extraction of detector behavior from the simulation is dependent on correctly implemented models of all geometries and fields in the storage ring. Experience from the last-generation $g-2$ experiment and simulation results so far have taught us that detector acceptance differs for calorimeters placed at different locations around the ring. Acceptance is the probability that a decay positron will be detected; it is a critical factor in determining how to translate the number of stored muons into a data rate and is therefore of high interest to the collaboration.

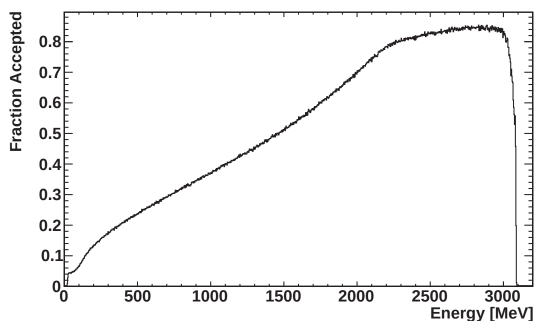

Figure 4.8-1. Recent results from the $g-2$ simulation: Detection probability for positrons of all energies.

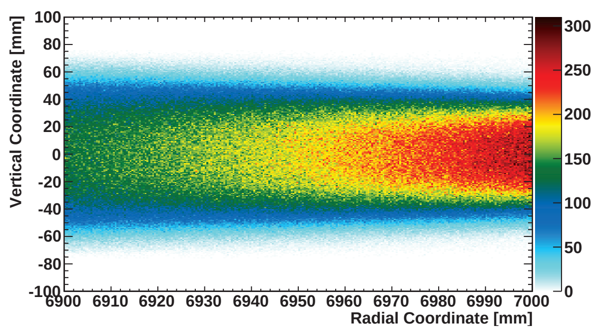

Figure 4.8-2. Recent results from the $g-2$ simulation: Map of where positrons hit the calorimeter, averaged over all calorimeters and positron energies.

A mature simulation provides the collaboration with an invaluable opportunity to develop and test analysis techniques in advance of data taking. In the case of the calorimeter, the simulation reports where positrons are most likely to hit the calorimeter, at what angle they impact, how these values vary with positron energy, and what overall event rate we expect in each crystal. This information can and will be used in training reconstruction algorithms to decompose pileup events into their constituents. A focus for the coming year will be development and testing of these reconstruction algorithms using simulation data.

4.9 Q method for anomalous precession frequency

A. T. Fienberg, D. W. Hertzog, and G. J. Plunkett

The Q-method of measuring ω_a (Q for charge) plots the light response of the calorimeters vs time, with no cuts to calorimeter data. What this effectively plots is positron events vs time, with each event weighted by the event energy. The resulting distribution is fit with the equation:

$$N_0 \exp(-t/\tau_\mu)\left[1 + A\cos(\omega_a t + \theta)\right] \ , \tag{1}$$

where N_0 is a measure of total charge measured by all calorimeters, θ is a function of the average path length a decay-positron takes to reach a calorimeter, A (asymmetry) is a the energy-weighted average asymmetry of detected decay-positrons, and τ_μ is the muon lifetime.

The traditional method of measuring ω_a, known as the threshold or T-method, plots only events which are above a certain energy threshold (~ 1.7 GeV), and assigns all such events with a weight of 1. The resulting distribution yields a higher value of A than the Q-method measurement, but with lower statistics. Also, the Q-method is attractive because it is exempt from the systematic uncertainty caused by pulse pileup that affects the T-method: When two events, each individually with energy below the threshold energy, strike a calorimeter within < 2.5 ns of each other, the T-method can erroneously count the two events as a single event with energy above the cutoff threshold if their combined energy is high enough. By having no cuts on energy, and by weighting each event by its energy, the Q-method weights the piled-up double-event as equivalent to two single, lower-energy events.

A digitizer waveform simulation effort is currently being undertaken to better understand problems posed by the Q-method. The simulation generates a digitizer trace for every crystal of every calorimeter, for each storage-ring fill. The necessary data are drawn from a large repository of `ARTG4-gm2` simulation data containing the energy deposited in each crystal, and the time that energy is deposited, for ~ 100 million muon decays. A crystal's energy deposition/time data are converted into a pulse shape and written onto that crystal's digitizer trace. Storage-ring fills are simulated by creating new digitizer waveforms every 10,000 $\pm$ 500 muon-decay events. Digitizer traces from each crystal, from each fill, are summed together to create Q-method plots.

Properly calculating the uncertainty of a Q-method plot is non-trivial and had not been previously investigated. Because each event is weighted by the amount of energy it deposits in a calorimeter, ideally the uncertainty of any one bin in a Q-method plot is equal to the sum of the weights squared for each event that occurred during that bin. However, the Q-method allows no event reconstruction, and the energy of individual pulses which contributed to a bin remains necessarily unknown. The solution to this problem was to consider each bin as composed of N average-energy pulses, and to set the variance of the bin as the sum of the weights squared and weight variance of the N average-energy pulses which made up the bin. The average and standard deviation of energy/event had to be calculated from simulations. Fig. 4.9-1 shows a Q-method plot generated by the waveform simulation, weighted with the average-energy uncertainty. The fit gives a very good χ^2 and suggests this method of weighting is very successful. It remains to be seen what effect noise has on the average pulse energy, however, as it is very possible that lower-energy events are rendered invisible by noise with a comparable height to the pulse height of a positron event. Further Q-studies will focus on the effect that noise has on Q-plots.

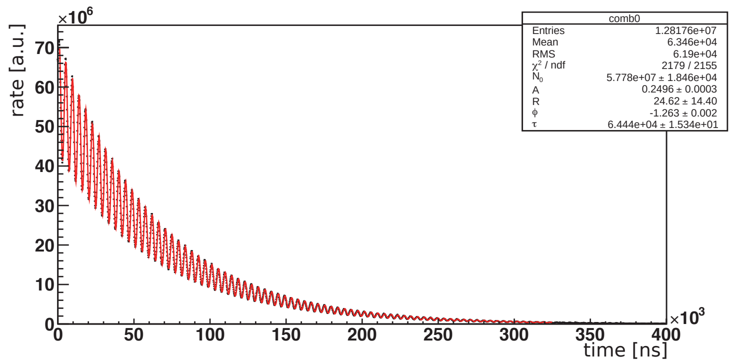

Figure 4.9-1. A Q-method plot generated by digitizer waveform simulation of 90 million muon decays. Each bin is weighted by the as if it were composed of N average-energy pulses, which resulted in a very good χ^2 (1.01).

4.10 Collimator optimization

D. W. Hertzog and N. S. Froemming

Knowledge of the position of the circulating muon beam in the $g-2$ storage ring is critical for determining the average field experienced by muons, and hence the value of a_μ extracted from the experiment. The maximum transverse extent of the muon beam is defined by the objects shown in Fig. 4.10-1A, called *collimators*. The main purpose of the collimators is to remove undesirable muons as rapidly as possible, while minimizing effects on the decay-electron signal measured in the downstream detectors.

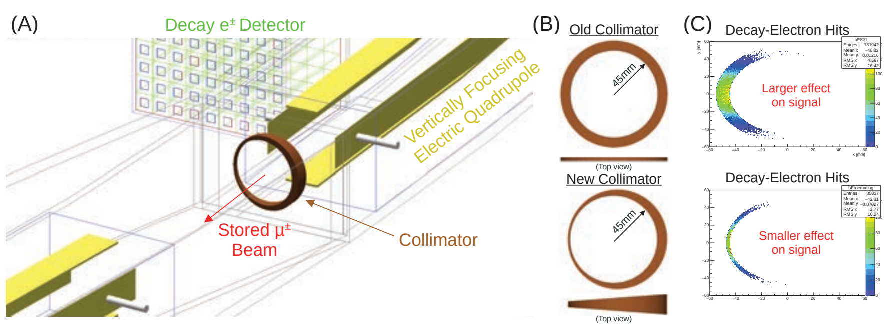

Figure 4.10-1. (A) Several collimators placed around the muon $g-2$ storage ring will define the maximum transverse extent of the stored muon beam. (B) Old collimator design *vs.* new collimator design. (C) Effect on decay-electron signal.

The UW has propsed an innovative variable-thickness collimator design for E989 (Fig. 4.10-1B). Muons striking the inner edge of the collimator have a lower momentum than those striking the outer edge of the collimator, and therefore a smaller energy loss is needed to ejected them from the storage region. The variable longitudinal thicknesses of the new collimators was chosen so that undesirable muons will (most probably) be ejected from the storage region after striking a collimator only once. The variable transverse thickness of the new collimators was chosen to minimize effects on the decay-electron signal while maximizing the loss rate of undesirable muons (Fig. 4.10-1C). The new E989 collimators, originally conceived at the UW, are now being constructed at Brookhaven National Laboratory in Upton, NY.

4.11 Injection optimization

D. W. Hertzog and N. S. Froemming

It is estimated that only $\sim 2\%$ of muons injected into the $g-2$ storage ring were stored in the BNL experiment. The biggest contributors to muon losses were (1) scraping/multiple-scattering in the beam channel during injection, and (2) inefficiencies in kicking the muon beam onto the proper orbit during injection. Thus, major improvements to the new experiment can be made by improving the above two areas. The UW has emerged as a collaboration leader in developing and implementing realistic simulations that allow various injection parameters to be investigated quickly and accurately. An example simulation is shown in Fig. 4.11-1. Several important design decisions, e.g. the beam collimators (Sec. 4.10), have been made based on UW simulation results.

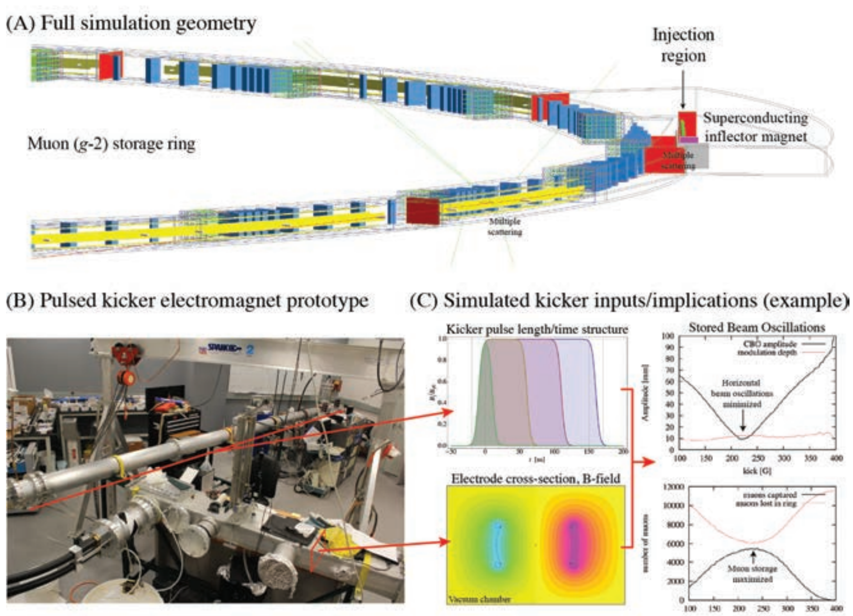

Figure 4.11-1. (A) The UW has emerged as a leader in the $g-2$ collaboration for developing realistic simulations. This particular example is designed to model muon injection and storage. (B) Pulsed electromagnet that will kick the muon beam onto the proper orbit during injection. (C) Example simulation parameters and results: When the number of muons injected is maximized, the amplitude of undesirable beam oscillations is minimized.

4.12 Measuring the effect of external, ppm-strength, periodic perturbations on a 1.45T magnetic field

M. Fertl, A. García, C. Helling, R. Ortez, R. E. Osofsky, M. W. Smith, and H. E. Swanson

The muon $g-2$ experiment requires very precise knowledge of the magnetic field seen by muons in the storage ring. Periodic perturbations from external sources, such as a 60-Hz field from power distribution and a 15-Hz field (plus harmonics) from the booster ring, perturb the nominal 1.45-T field. The storage-ring field is measured using pulsed NMR probes filled with petroleum jelly, which has a longitudinal relaxation time on the same order as the period of these perturbative fields, making their measurement difficult.

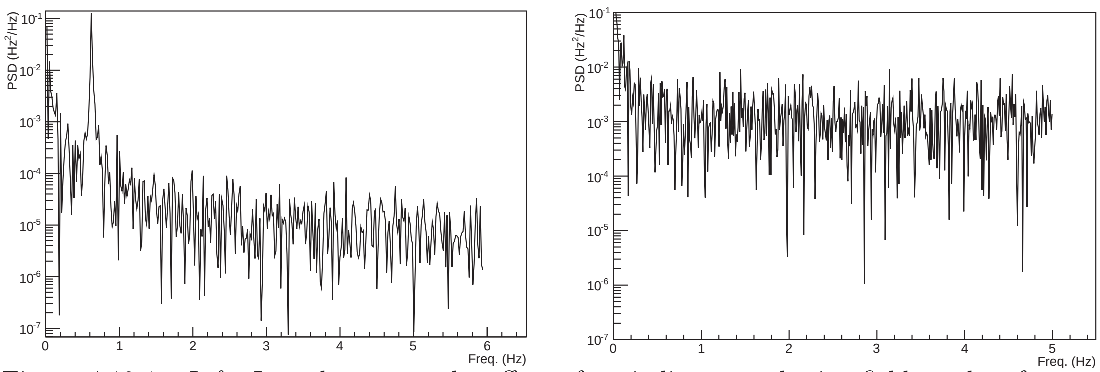

Figure 4.12-1. *Left:* In order to see the effect of periodic, perturbative fields at low frequencies, data can be taken at a specifically chosen measurement rate. To look for a 60 Hz perturbation, data were taken at 11.88 Hz. A PSD of the extracted frequencies is shown with a prominent spike. *Right:* Data were also taken at 10 Hz, an integer multiple of 60 Hz, so no signal is expected. The PSD is shown (these data were taken in a noisier part of the magnet). From a PSD containing a peak like the one on the left, the frequency and amplitude of an external, periodic perturbation can be calculated.

For a periodic perturbation, the frequency of interest can be aliased down and its effect seen over a sequence of many measurements. In particular, one can choose a measurement rate such that after 20 measurements, the same phase in the perturbation is reached again. Since the longitudinal relaxation time of protons in the NMR probes is on the order of 40 ms, simply moving ahead by $\frac{1}{20}$ of a period doesn't allow enough time for the spins to relax. Therefore, we would like to skip some number of full periods before shifting the phase by $\frac{1}{20}$ of a cycle. The time between measurements should be $\Delta t_{meas} = (N + \frac{1}{20})\frac{1}{f}$, where N is the integer number of skipped periods and f is the frequency of interest. The measurement rate is then $f_s = 1/\Delta t_{meas}$.

A series of FIDs is taken at the specially chosen measurement rate, and the frequency, representative of the field strength, is extracted from the first millisecond of each one. Next the squared Fourier transform of the frequency data (the power spectral density, PSD) is fit to a Lorentzian plus $1/f$ and white-noise terms. An example PSD, for data taken with a measurement rate of 11.88 Hz to look for a perturbation at 60 Hz ($N=5$), is shown in Fig. 4.12-1, in addition to data taken at a rate of 10 Hz, where no peak is expected. Using the peak frequency (f_0) from the Lorentzian fit, the frequency of the periodic signal is calculated as $f = Nf_s + f_0$. Extracting the amplitude of the signal is slightly more difficult.

One interpretation of Parseval's theorem is that for a signal, the power in time is equal to the power in frequency space. This is true both for a signal in its entirety, as well as for any given frequency component. In frequency space, the power is calculated by integrating under the peak in the PSD after subtracting the noise from each bin. In time space, the signal of interest is a sine wave at one specific frequency. The time-averaged power in a sine wave of amplitude A is simply $P = A^2/2$. Equating this with the power in frequency space, the amplitude of the sine wave can be calculated.

Using simulated frequency data, this method has provided good results. Analysis performed on simulated data of a 60-Hz periodic perturbation with a 324-ppb amplitude returned a signal at 60.0009 Hz with an amplitude of 326 ppb, which amounts to sub-Hz resolution for the nominal field in the storage ring magnet. A real 60-Hz signal has also been measured at CENPA in a dipole magnet at the same field strength expected in the storage-ring magnet and analysis returned an amplitude and frequency consistent with the oscillations seen in the extracted frequency values.

4.13 Production of 400 pulsed proton NMR probes for the $g-2$ Experiment

M. Fertl, A. García, C. Helling, R. Ortez, R. E. Osofsky, M. W. Smith, and H. E. Swanson

A successful measurement of the muon anomalous magnetic moment, $a_\mu = (g-2)/2$, crucially relies on a precise knowledge of the magnetic-field distribution seen by the muons orbiting in the storage ring. While this distribution can be measured with a special magnetic-field mapper several times a week, this trolley has to be retracted into its storage position during muon operation. To track changes of the magnetic field between trolley measurements a stationary array of pulsed proton nuclear magnetic resonance (pNMR) probes is distributed along the outside of the storage ring's vacuum chamber. The magnetic-field team at CENPA is responsible for providing the pNMR probes for the stationary array as well as the trolley. Over the last year the decision has been made to build 400 new pNMR probes, after the vast majority of those used in the BNL E821 experiment[1] were found to be broken[2].

Over the last year, different implementations of the necessary improvements have been tested and a decision was taken on a final design, shown in Fig. 4.13-1. The new features include a crimp connection between the radiofrequency cable braid and the base piece of the probe instead of a conduction epoxy joint as was used before. This will provide a very reliable electrical connection. All 400 probes will be filled with the petroleum jelly characterized beforehand by NMR measurements instead of with water doped with copper sulfate. This will eliminate the risk of corrosion for aluminum parts due to leaking of the water sample.

[1] G. W. Bennett *et al.*, Phys. Rev. D **73**, 072003 (2006).
[2] CENPA Annual Report, University of Washington (2014) p. 69.

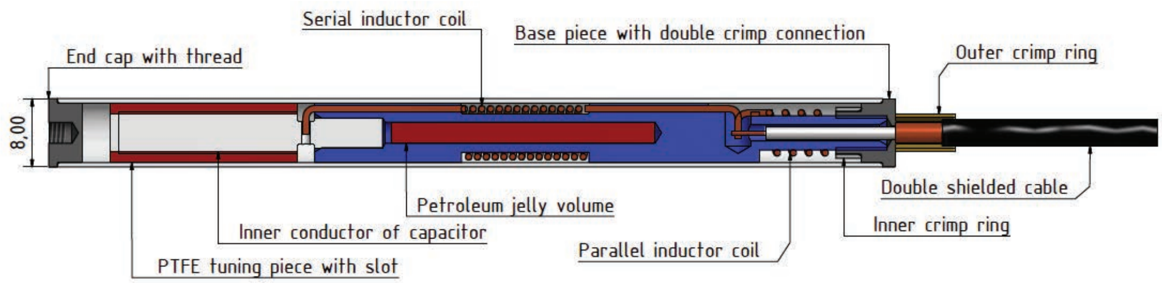

Figure 4.13-1. A cut-away view of the final design of the new pNMR probes. The double-shielded radiofrequency cable will be crimped to the base piece of the probe. This base piece holds the support structure for the serial and parallel inductors, the inner conductor of the capacitor, and connects to the aluminum sleeve that forms the ground plate of the capacitor. The easily removable end cap provides fast access to the PTFE tuning piece. By screwing the PTFE piece on or off the inner conductor the resonance frequency of the pNMR probe can be adjusted.

Figure 4.13-2. All the parts necessary to assemble a complete pNMR probe are contained in an *assembly kit*. Once a probe is completely assembled it is marked with a unique number on a shrink tube.

At the time of the report 75-pNMR probes have been completed. The production chain for the remaining probes is well on its way.

To make the most efficient use of machining time while ensuring good progress in the probe assembly, pieces are produced in batches of about 80 at a time. This allows parallel production and assembly lines for the new probes. To standardize the assembly among the different people involved, an assembly manual was written which describes all assembly steps in detail. After the pieces come from the machine shop they are cleaned and distributed among so called *assembly kits* as shown in Fig. 4.13-2. All parts necessary to assemble one complete probe can be found in an assembly kit. This makes the assembly of probes straightforward and avoids a time-consuming search for parts. After a probe is mechanically assembled it is frequency-tuned and matched to the cable impedance. The control measurements are recorded and stored for documentation in the $g-2$ Traveler database (Sec. 4.17).

4.14 Measuring the temperature dependence of the magnetic properties of petroleum jelly for pulsed proton NMR

M. Fertl, A. García, C. Helling, R. Morris, R. Ortez, R. E. Osofsky, M. W. Smith, and H. E. Swanson

To track changes of the magnetic field in the muon $g-2$ storage ring between trolley measurements, a stationary array of pulsed proton nuclear magnetic resonance (pNMR) probes is distributed along the outside of the storage ring's vacuum chamber[1]. One source of magnetic-field changes is expansion and shrinkage of the storage ring and the iron yoke due to residual temperature changes in the MC1 building at Fermilab. The frequency of an NMR signal is affected by the properties of the physical magnetic field and the properties of the pNMR probes. The magnetic field measured with the petroleum-jelly-filled probes, $B_{\mathrm{p,local}}$, is given by

$$B_{\mathrm{p,local}} = \left(1-\delta_{\mathrm{t}}\left(T\right)\right) B \tag{1}$$

$$\delta_{\mathrm{t}}\left(T\right) = \sigma\left(T\right)+\delta_{\mathrm{b}}\left(T\right)+\delta_{\mathrm{s}}\left(T\right) \tag{2}$$

where B is the magnetic field in vacuum, σ the isotropic chemical shift, δ_{b} the geometry-dependent bulk susceptibility correction, and δ_{s} a dia- and paramagnetic contribution of the construction materials. Each of the correction factors has a temperature dependence which must be understood to correctly distinguish between temperature-induced variations of the physical magnetic field and temperature-induced variations of the pNMR probe properties. Temperature changes of the ring will directly transfer onto the pNMR probes as they are directly mounted onto the vacuum chambers of the muon storage ring. While the temperature dependence of the construction materials (aluminum, copper, PTFE) are well known this is not the case for petroleum jelly, which is not a pure substance but a mixture of long-chain hydrocarbons.

Before deciding on the specific type of petroleum jelly to fill in the pNMR probes, the distribution of the magnetic moments for several samples of petroleum jelly was measured. To have a good frequency resolution and homogeneous magnetic field conditions a 500-MHz pulsed proton NMR spectrometer in the UW Chemistry Department was used. The petroleum jelly samples were injected into spherical NMR tubes with cylindrical extensions. This separates the temperature dependence of the isotropic chemical shift from the effect on the bulk susceptibility since the bulk susceptibility correction vanishes for a spherical geometry. While the NMR setup was standard, the running conditions were not. To avoid any shift of the proton spectrum no deuterated solvents (solvent shifts) were added. As a consequence the spectrometer could not be locked to a known reference frequency and the proton concentration in the sample was extremely high. To shim the magnetic field before the measurements a 99.9% D_2O sample was used which produced a line width of ~ 1 ppb. A sample distribution of magnetic moments in the sphere/cylinder geometry parallel to the magnetic field is shown in Fig. 4.14-1.

The spectrum is split in two groups due to the different bulk susceptibility contributions for the spherical and cylindrical geometries, which allows the extraction of χ. Furthermore

[1] G. W. Bennett *et al.*, Phys. Rev. D **73**, 072003 (2006).

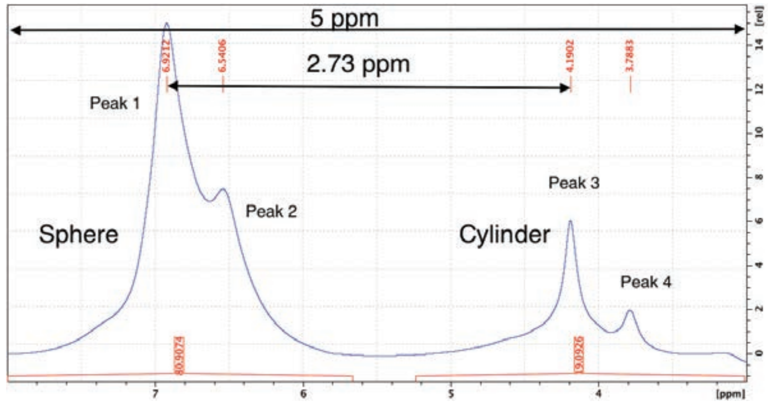

Figure 4.14-1. The distribution of magnetic moments in a petroleum jelly sample. The sample geometry is a sphere with a cylindrical extension. Due to the bulk susceptibility contribution the spectrum is split in two groups, separated by $\sim 1/3\chi$. Peaks 1 and 2 belong to the spherical part, and peaks 3 and 4 to the cylindrical part of the sample. The well-resolved peaks confirm that petroleum jelly has a broad distribution of magnetic moments in contrast to pure water.

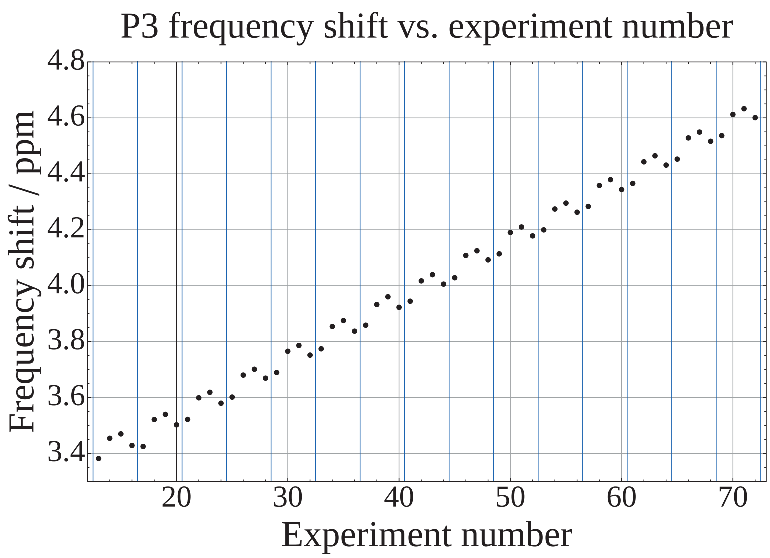

Figure 4.14-2. The modulation of a signal peak position as the sample temperature was varied by 10 °C in many ABBA sequences. The slow background drift is due to the free-running operation of the NMR spectrometer.

two peaks are visible in each group, showing the distribution of magnetic moments in a petroleum jelly sample. For the temperature-dependent measurements the sample temperature was changed by 10 °C in many ABBA sequences Fig. 4.14-2. This allows for the correction of linear drifts of the spectrometer reference frequency which occur over the timescale the sample needs to reach thermal equilibrium (600 s). Extracting the modulation amplitude of the peak positions as a function of sample temperature allows us to determine the temperature dependence of σ and χ.

Based on a preliminary analysis the petroleum jelly with the smallest temperature dependence was chosen to fill the new pNMR probes. From the different modulation amplitudes for the peaks in the cylindrical and the spherical cell parts one concludes that the temperature dependence in petroleum jelly is dominated by the bulk susceptibility correction. Overall it is about a factor of four smaller than for pure water. A more detailed analysis taking the exact geometry into account is a work in progress.

4.15 NMR DAQ for ring-magnet shimming

M. W. Smith

As the $g-2$ experiment's hardware approaches completion so must the data-acquisition (DAQ) systems. In particular much of the necessary work on the proton nuclear magnetic resonance (pNMR) DAQ was completed in the past year. The $g-2$ collaboration bases its DAQ systems on the MIDAS framework implemented by researchers at the Paul Scherrer Institute, Switzerland. MIDAS itself takes care of many aspects of the DAQ system, such as run control and integration of multiple data streams. Important tasks for the pNMR DAQ were implementing front-ends capable of reading out several different configurations of pNMR probes, creating analyzers for post-processing and online display purposes, and organizing the DAQ infrastructure on the DAQ machine to integrate different front-ends. The front-ends need to deal with different sequences of pNMR probes depending on whether they were used with the shimming platform, shimming fixed probes, running trolley, or running fixed probes.

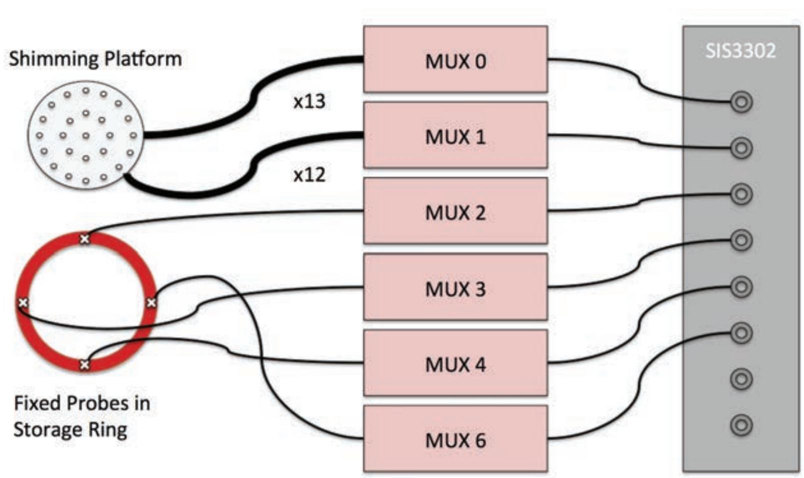

Figure 4.15-1. A diagram depicting the setup that will be present during the process of shimming the magnetic field. The DAQ must coordinate readout of all of these probes. The probes on the shimming platform are all triggered in a short sequence, and similarly the fixed probes must be triggered, but at a different rate compared to the platform.

The gist of working in the MIDAS framework involves implementing some standard functions on top of templates available in MIDAS. The front-ends have the standard run-control functions, i.e., start, stop, pause, resume, initialization, and teardown. In addition front-ends need to implement an event readout routine that transfers event data into a MIDAS "bank".

The banks are collected by MIDAS's event builder and written to an output file. Analyzer modules also have access to the MIDAS banks output by the front-ends, and analyzers can create histograms to provide online feedback as well as perform analysis to extract important characteristics from the data. MIDAS provides a convenient online run-control interface for starting/stopping/pausing runs.

The $g-2$ pNMR front-ends need a wide variety of features beyond the simple data serving model of MIDAS front-ends. Collecting data from a single pNMR probe requires selecting the proper configuration on a multiplexer using an Acromag IP470A VME module, triggering a fire pulse via the same device, triggering the start of data acquisition on the VME-based Struck 3302 waveform digitizer, and recording the resulting free induction decay of the pNMR probe. All of the hardware must be controlled in software run by the front-end. An example setup for the shimming process is depicted in figure Fig. 4.15-1. On top of all that, each front-end needs to poll a different sequence of pNMR probes. This is a tall order for a single C++ file, so the front-ends actually draw classes from an external codebase to do the brunt of the work. The front-ends use convenient classes to collect the data and perform preliminary analysis before passing the data through the MIDAS framework.

4.16 Applying time-frequency analysis techniques to nuclear free induction decay (FID) signals

M. Fertl, A. García, C. Helling, R. Ortez, R. E. Osofsky, M. W. Smith, and H. E. Swanson

The $g-2$ pulsed NMR probes make use of the proportionality between the frequency of the free induction decay (FID) signal and the magnitude of the magnetic field to determine the field strength affecting the active probe region. Because the $g-2$ experiment is a precision experiment, it is important to determine the frequency of a FID signal to ppb precision. A limitation comes from magnetic-field gradients which produce regions precessing at slightly different Larmor frequencies within the active probe volume. The probe will simultaneously pickup the decohering regions causing the frequency to change over the course of the FID signal. It is only the zero-time value, corresponding to the average field magnitude over the active region, which obeys the proportionality factor between frequency and magnetic field magnitude. Thus, given our required precision, techniques that simply report an average frequency over the lifetime of the signal could potentially have large systematic errors.

One of the techniques being developed to explore how the frequency changes with time is based on the Wigner-Ville distribution(WVD)[1], a member of the time-frequency class of distributions, which can be used to compute a frequency value at each time instant of the observed signal. The WVD is described by the following equation:

$$WVD(t,\omega) = \frac{1}{2\pi}\int_{-\infty}^{\infty} z\left(t-\frac{\tau}{2}\right)\cdot z^{*}\left(t+\frac{\tau}{2}\right)e^{-i\omega\tau}d\tau \tag{1}$$

[1] L. Cohen, "Time-Frequency Distributions - A Review," Proc. of the IEEE, **77**, 941 (1989).

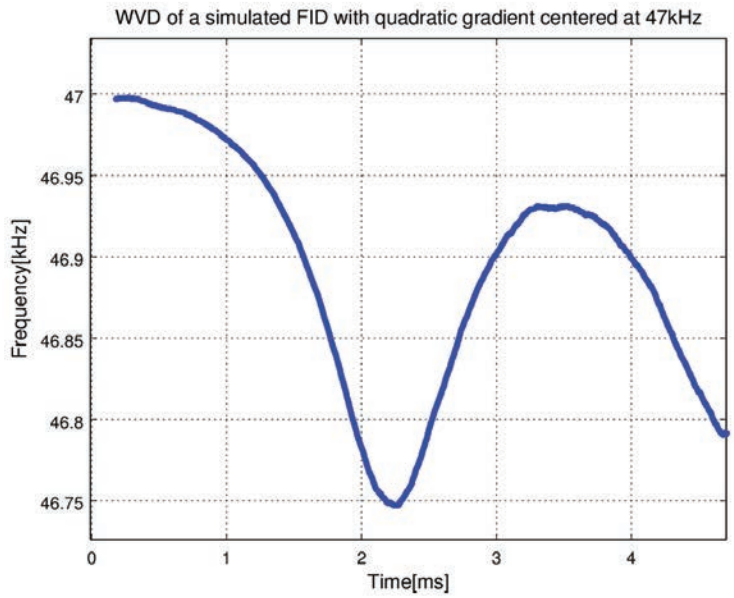

Figure 4.16-1. Magnetic-field gradients introduce a number of regions which precess at slightly different Larmor frequencies within the active sample region. The decoherence amongst these regions is what causes the observed frequency to change with time. We simulated a quadratic gradient with regions whose Larmor frequencies varied quadratically and summed up each region to make a single FID. The plot above shows the results of the Wigner-Ville technique applied to this simulated dataset.

where $z(t)$ is the analytic signal associate of our FID signal, $s(t)$, defined as:

$$z(t) = s(t) + ih(t) \tag{2}$$

where $h(t)$ is the quadrature component found by applying the Hilbert transform to $s(t)$.

The $z\left(t - \frac{\tau}{2}\right) \cdot z^*\left(t + \frac{\tau}{2}\right)$ function is a type of autocorrelation operation where the time variable t is not integrated out. This instantaneous autocorrelation function is then Fourier-transformed to give $WVD(t, \omega)$. For our purposes, it is sufficient to extract the peak frequency component (by fitting the peak of each Fourier spectrum to a Gaussian curve) for each time instant of $WVD(t, \omega)$, making its interpretation straightforward. To illustrate the technique, we simulated a quadratic gradient with a known zero-time frequency and applied the Wigner-Ville technique to map the frequency change of the signa with time Fig. 4.16-1.

The correct zero-time frequency for the simulated data is 47 kHz. If one extrapolates $WVD(t, \omega)$ to time zero, one gets a value roughly 2 Hz ($\sim$30 ppb) from 47kHz. We hope to use the difference between maximum and minimum and the periodicity of the frequency curve to estimate the magnitude of the net gradient affecting the signal. This method is reliable for the extraction of the zero-time frequency in the presence of gradients, and we are currently testing several possible physical scenarios with simulations.

4.17 Quality-control database

A. T. Fienberg, D. W. Hertzog, and M. W. Smith

By the time the $g-2$ experiment is ready to cut the ribbon and turn on the muon beam, the group will need to keep track on 1300 PbF_2 crystals, 1300 silicon photomulipliers, 400 pNMR probes, and additional hardware devices. There is a clear need for a centralized system for quality control. The quality-control system should be adaptable so it can interface with different hardware attributes, simple to allow adding new types of hardware, user-friendly for interfacing with stored entries, maintainable, scalable and secure.

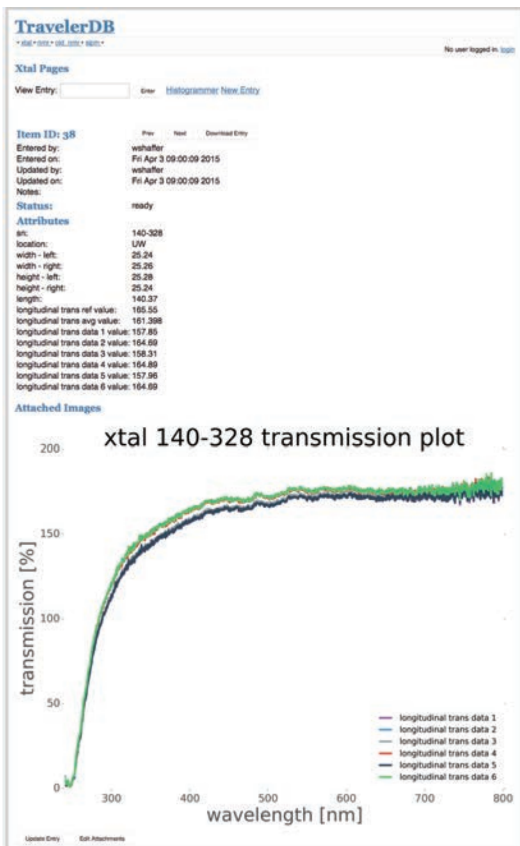

Figure 4.17-1. A screenshot of the TravelerDB displaying a PbF_2 entry. Notice the attributes as well as an attached plot which is generated in the Python function for saving crystal entries. It uses the mandatory data files attached to the entry to produce an aggregate plot.

TravelerDB is built on top of the Flask microframework for Python, and CouchDB. Flask facilitates all the power and simplicity of the Python language as well as bringing a powerful HTML templating library to the table, namely the Jinja2 engine. CouchDB is a database architecture based on JSON documents. It is inherently NoSQL and maintained under the Apache umbrella. CouchDB provides an extremely adaptable database for our purposes while maintaining a reasonable level of scalability which should suit our purposes. The database has no problems scaling up to tens of thousands of documents which is the expected order for the $g-2$ hardware quality-control pages. A sample crystal page is shown in figure Fig. 4.17-1

The user interface is completely web-based, a very convenient medium. The sole exception is if one needs to add a new hardware type into TravelerDB. Adding new devices is as simple as adding an entry to the JSON document entry_attributes.json found in the main "traveler" directory of the TravelerDB code, and adding save/update functions into entry_functions.py. The entry definition can require text attributes, numerical attributes, radio buttons for attributes with only a few common options, data files, and image files. Additional processing can introduce more attributes in the save/update functions for the hardware.

4.18 Quality-control procedures for lead fluoride (PbF_2) crystals

D. W. Hertzog and W. Shaffer

Central to the operation of the calorimeters that will be used in the $g-2$ experiment are the PbF_2 crystals. As such, the quality of the crystals must be assessed as shipments of new crystals arrive monthly. These testing procedures are necessary so that any trends in quality can be identified and the overall quality of the crystals can be tracked. Additionally they allow for preliminary mapping of crystal locations within the 24 calorimeters based on results obtained. The procedures can be divided into two separate but crucial areas, longitudinal transmission tests and physical measurement/characteristics, discussed in more detail below.

Given the fragile nature of the crystals it is simply not practical to remove every crystal from its protective wrapping. Instead, data sheets provided by the manufacturer, Shanghai Institute of Ceramics Chinese Academy of Sciences, are screened for any irregularities in measurements performed during manufacturing, and outliers are noted. After any outliers are identified one crystal in each case of ten is selected randomly, unless the case contains an outlier. In that situation the outlier crystal is the one measured for that case. The crystal is removed from its protective packaging and visually inspected with ambient light for any physical flaws. Once the initial visual inspection is completed high-intensity light is introduced into the crystal to reveal structural flaws and impurities. Finally, the height, width and length are measured with the height and width measured at each end to identify changes in uniformity.

Longitudinal transmission measurements are taken using an Ocean Optics PX-2 pulsed xenon light source and Ocean Optics USB2000+UV-VIS-ES spectrometer contained in a darkbox. The PX-2 light source emits light pulses of wavelengths ranging between 220 − 750 nm and the spectrometer wavelength response range is 200 − 1100 nm. The light source and spectrometer are run with Ocean Optics OceanView software. The optics are zeroed for any light present in the darkbox and a longitudinal transmission measurement is taken on a reference crystal to track any long-term fluctuations in the apparatus. Each crystal tested has six longitudinal transmission measurements taken, with the direction of the light pulse switched between single measurements (see Fig. 4.18-1). Once the measurements are completed an average is computed at 400 nm and the crystal is graded for overall quality and performance. All data from measurements performed is digitally logged.

Testing has so far revealed an overall increase in quality of the crystals, both in physical characteristics and transmittance. Only a single lot has required a second set of crystals to

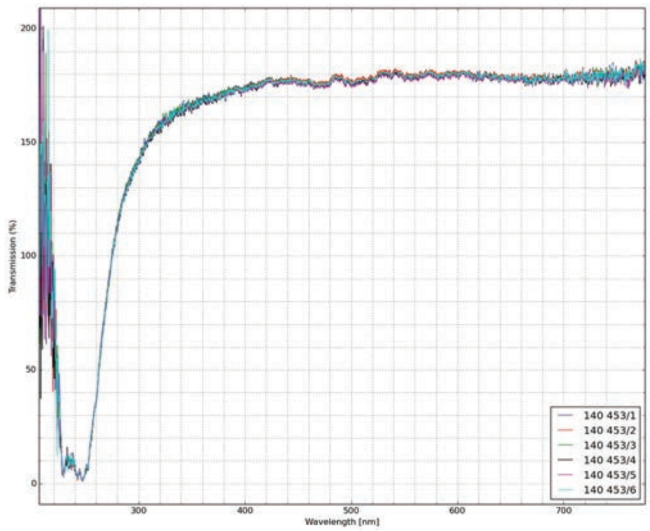

Figure 4.18-1. Results of typical longitudinal transmission measurement of a single crystal. Transmission percentage over 100 % is a result of the focusing effects of the crystals.

be tested due to fluctuations in the initial set. These procedures will be invaluable during the calorimeter construction process as they allow for very quick assessment of quality for each crystal as well as where it would perform best within the calorimeter, which is of fundamental importance for optimizing data collection.

4.19 Quality control of magnetic components

M. W. Smith and H. E. Swanson

The magnetic fields created in the $g-2$ ring need to be impeccably uniform in the muon storage region. The uniformity specification is a pure dipole field to about 10 parts per million (ppm) before the ring goes under vacuum. To add a little perspective, the Earth's magnetic field is somewhere around 25 ppm on top of the target field of 1.45 T. A 10-ppm perturbation is not negligibly small, so the perturbations caused by any electronics or materials that will reside close to the muon-storage region are of concern.

To characterize the perturbative threat of different materials, we set up a test bench at CENPA. We have the requisite: magnetic test field of 1.45 T, pNMR probes, data-acquisition system and analysis routines. Two pNMR probes are set up at slightly different distances from the sample inside the magnet. Test materials are placed on an aluminum arm used to change the displacement between the test material and the pNMR probes. The aluminum arm is linked to a stepper motor which can be controlled using a software interface. An image of the setup is included as Fig. 4.19-1 (*left*). The procedure starts with a background run if there isn't a recent one. After taking a background run, the test sample is mounted onto the aluminum arm and begins the test stand collecting data. The DAQ records a specific number of free induction decays at each step, extracts the frequency, averages the frequencies for each step and outputs the frequency difference between the two probes. A result for a well-known sample with large magnetic susceptibility shown in Fig. 4.19-1 (*right*).

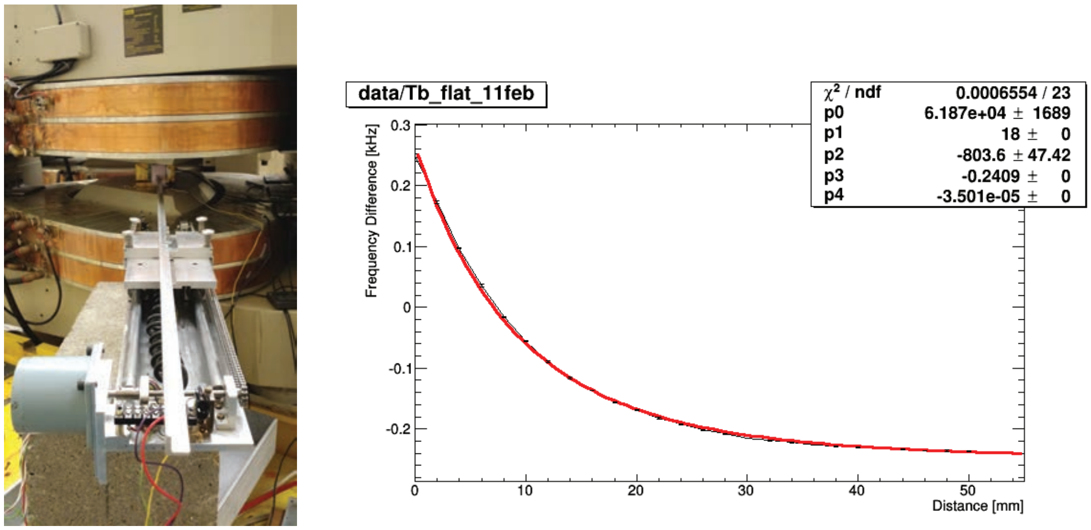

Figure 4.19-1. *Left:* The UW test stand. *Right:* Measurement for a sample of terbium which is known to have strong ferromagnetic properties.

The analysis routine is fairly straightforward. All fits are based on the difference between the two pNMR probes, so as to mitigate the effect of overall drift in the field. Each probe will experience similar drift, so it cancels out. The background run (no test sample) is fit to a linear background. This linear background is subtracted from the test sample data. Then, the processed data is fit to a point dipole model, and the dipole strength of the sample is extracted as a proxy for the field strength. The procedure, while not extremely high fidelity has been shown to agree with known test samples of terbium and bismuth to about a factor of two. This level of precision makes it useful for guiding hardware design choices.

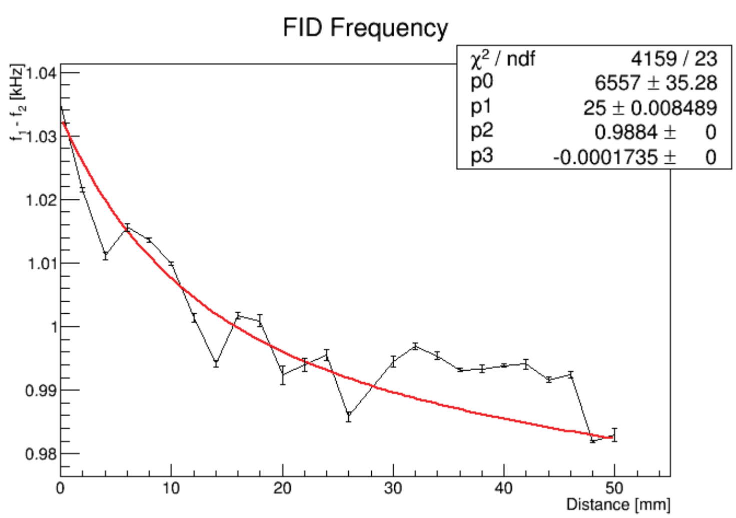

Figure 4.19-2. Measurement results for the straw tracker electronics board. Note the scale of the changes on the vertical axis, and compare them to those in Fig. 4.19-1 (*right*). The electronics board caused much smaller perturbations than the terbium sample.

Several components of the $g-2$ electronics have been sent to CENPA to characterize the perturbative threat to the magnetic field. Among these were electronics components from the straw tracker detector, several blocks of aluminum machined with different techniques from Argonne National Lab, electronics boards for the SiPM detectors used in the calorimeter, and additional electronics components. The expected perturbations on the muon magnetic storage field were found to be on the order of 1 ppm or smaller, and as such the samples were deemed clean. A sample measurement are shown in Fig. 4.19-2.

MuSun

4.20 Overview of the MuSun experiment

D. H. Hertzog, P. Kammel, M. H. Murray, D. J. Prindle, R. A. Ryan, K. B. Wall, and F. Wauters

The final result of the MuCap experiment[1] was recently published, followed by a technical paper describing the key enabling instrument for achieving this goal, an ultra-pure hydrogen time projection chamber (TPC)[2]. A publication of our precision measurement of the formation rate of muonic hydrogen molecules, an important ingredient to the MuCap analysis, was accepted by PRC on April 2015[3]. MuCap measured the rate of muon capture on the proton to determine g_P, the weak-pseudoscalar coupling of the proton. This first precise and unambiguous measurement of g_P confirms a fundamental prediction of low-energy QCD.

The good agreement between the MuCap result and theory demonstrates that all parameters entering the *one-nucleon* weak amplitudes are well under control. This allows the MuSun experiment to extend this program with a precise determination of the strength of the weak interaction in the *two-nucleon* system, using the process

$$\mu + d \rightarrow n + n + \nu. \tag{1}$$

MuSun will determine the sole unknown low-energy constant involved in modern – QCD-based – effective field theory (EFT) calculations of weak nuclear reactions. The anticipated precision is 5 times better than presently available from the two-nucleon system and will be essential for calibrating these reactions in a model-independent way. This will provide a benchmark for extending the EFT method to more complicated few-body processes. Regarding the family of two-nucleon weak-interaction processes, muon capture will provide unique constraints on electro-weak astrophysical processes of fundamental importance, like pp fusion or νd scattering, whose rates have never been measured directly. The scientific aspects of this field are covered in recent review[4].

[1] V. A. Andreev *et al.* (MuCap Collaboration), Phys. Rev. Lett. **110**, 012504 (2013).
[2] J. Egger *et al,*, Eur. Phys. J. A **50**, 163 (2014).
[3] V. A. Andreev *et al.* (MuCap Collaboration), Phys. Rev. C, in press (2015).
[4] P. Kammel and K. Kubodera, Annu. Rev. Nucl. and Part. Sci. **60**, 327 (2010).

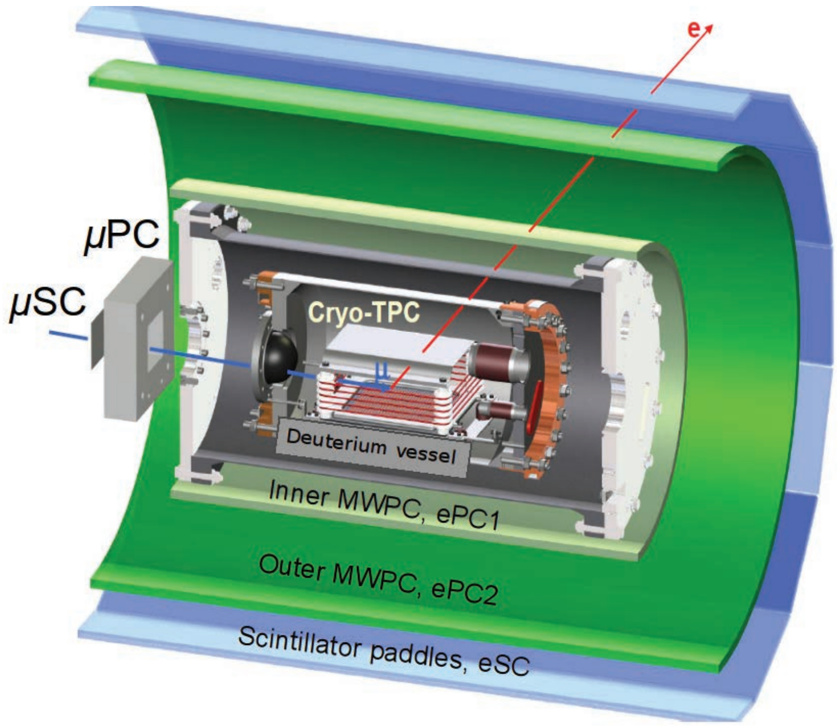

Figure 4.20-1. MuSun detector model. Muons pass through entrance detectors to stop in a deuterium target TPC. The decay electron is detected in two cylindrical wire chambers (green) and a 16-fold segmented scintillator array (blue).

MuSun measures Λ_d, the capture rate from the doublet hyperfine state of the muonic deuterium atom in its 1S ground state, by determining the negative muon decay rate λ_- in a time projection chamber filled with pure deuterium gas. The capture rate is derived from the difference

$$\Lambda_d \approx \lambda_- - \lambda_+ \ , \tag{2}$$

where λ_+ is the positive muon decay rate[1]. As shown in Fig. 4.20-1, incoming muons are detected by muon beam counters (two thin scintillator slabs and a wire chamber) and stopped in the TPC. The decay electrons are tracked in two cylindrical wire chambers surrounded by a hodoscope consisting of a double layer of scintillator paddles. The conditions of the active target must lead to an unambiguous extraction of Λ_d, independent of muonic atomic-physics complications occurring after the muon stops in deuterium. Conditions are optimized for T = 31 K and 6.5% liquid hydrogen density. A high-density cryogenic TPC filled with ultra-pure deuterium was developed as an active target to monitor the muon stopping location and muon-catalyzed fusion reactions.

2014 was an excellent year for MuSun. The new TPC designed at CENPA was constructed according to a tight schedule to allow thorough testing and preparation before the run. It performed flawlessly during the whole production period. The continuous purification system (CHUPS) maintained excellent purity at the 1-ppb level, which could be monitored

[1] V. Tishchenko *et al.* (MuLan Collaboration), Phys. Rev. D **87**, 052003 (2013).

by a significantly improved gas chromatography system that led to a consistent result. The new TPC cryogenic preamplifiers[1] also worked without problems and now have sufficient resolution to provide in-situ monitoring of the critical gas purity. The PSI accelerator delivered stable beam, but the secondary muon beam still needed improvements. We were forced to dedicate some time and effort to scanning the beam, but by the middle of the run this problem was resolved with a new collimator design.

The analysis also made significant progress, and we address the most challenging aspects in a dedicated section of this report.

MuSun plans to measure Λ_d with a precision of better than 1.5%, which amounts to $\delta\Lambda_d = 6$ Hz. The capture rate is derived according to Eq. (2). As the positive muon lifetime is well known, the uncertainty in $\delta\Lambda_d$ is dominated by the MuSun measurement of λ_- in deuterium. If we assume equal statistical and systematic contributions to the final result, the statistics requirement for the number of fully reconstructed $\mu - e$ decays becomes 1.2×10^{10} events. We collected 6×10^9 events in run 2014 and expect 8×10^9 events during the 3 months of data taking in 2015, in total 1.4×10^{10} events. Due to the fusion interference discussed below, the lifetime fits will start after 1 μs, which reduces the statistics by 37% to 0.9×10^{10}. Thus, if the 2015 run matches the excellent 2014 data-taking efficiency, we will come close enough to the desired statistics to complete production data-taking for MuSun. In 2016 we are considering a shorter run period for systematic studies.

4.21 2014 production run

D. W. Hertzog, P. Kammel, M. H. Murray, D. J. Prindle, R. A. Ryan, K. B. Wall, and F. Wauters

The 2014 production data run resulted in over 6×10^9 μ^- and 1×10^9 μ^+ events after all data-selection cuts, such that the remaining stops are representative of the final statistics. In addition to acquiring nearly half of the total required statistics for the MuSun experiment, a week of data was collected with modified running conditions for systematic studies. The accumulation of statistics throughout the run can be seen in Fig. 4.21-1.

The large success of the run was due, in part, to the installation of an upgraded cryo-TPC[2], comprised of a new Frisch grid, improved high-voltage structure, and high-precision temperature sensors. Several months before the run, the TPC was fully constructed in the PSI detector group clean room. After closing the pressure vessel and testing all electrical connections, the detector was installed and tested at its nominal temperature and pressure. All components survived temperature cycling, the vacuum seals were free of leaks, and the grid high voltage was found to be stable up to 3.5 kV — the voltage required for full transparency. A photograph of the new TPC can been seen in Fig. 4.21-2 . It operated at stable conditions, with 80 kV on the cathode and 3.5 kV on the Frisch grid, and in combination with the new cryogenic preamplifiers provided a 10 keV (D_2) resolution for the duration of the run.

[1] R. A Ryan *et al.*, J. Inst **9**, P07029 (2014).

[2] CENPA Annual Report, University of Washington (2014) p. 86.

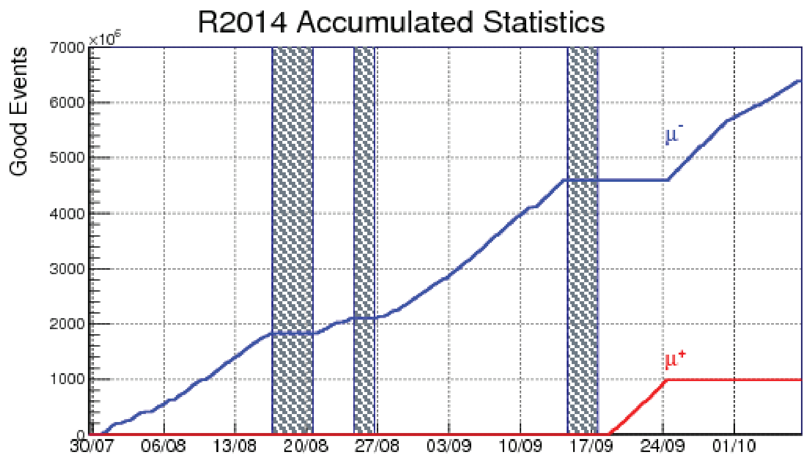

Figure 4.21-1. Number of good muon stops acquired over the run period, after all selection cuts applied, for the 2014 run. The gray bands indicate two beam-less periods due to scheduled shutdowns and one period for target exchange. The available beam could be utilized with high efficiency, averaging a collection rate of 10^9 good events per week.

Once beam time commenced, all detectors were brought into stable running conditions within one week, allowing for focus on optimization in several areas. Attempts to increase the data rate with DAQ improvements included mounting a new solid-state drive (SSD) on the main DAQ computer and changing the output file size. In the first week of production data, the DAQ performance was significantly improved, reducing the deadtime to 10%. Optimization of the beam tune continued for several weeks into production. In addition to careful tuning of the beamline elements, the apparatus was lowered to symmetrize the stopping distribution and the beam profile was scanned via a SiPM. A new collimator was constructed, and optimal muon rates of 26 kHz were achieved.

A portion of the beam time was allocated for running with modified conditions to accumulate data useful in studying background contributions, fusion interference, and gas impurities.

A clocked entrance trigger was installed on a 2.5-kHz clock to replicate a muon in the entrance detectors for background studies. In addition to running the clock permanently during the second half of production, an eight-hour shift with an increased rate of 20 kHz was taken to accumulate significant statistics during a shorter period.

Several weeks into the run, a magnet was installed to provide a spin-rotation field for positive muons and we switched to data taking with μ^+. A week of data was accumulated with smooth running conditions, resulting in 10^9 events. These data will be compared to μ^- data to characterize effects which are only present with negative polarization, such as fusion interference.

To increase sensitivity for in-situ impurity detection in the TPC (Sec. 4.22), data were taken for three days at 50% nominal density. This reduction in density provides a clear separation between the recoil energies from muon capture on impurities and the ^{3}He recoil

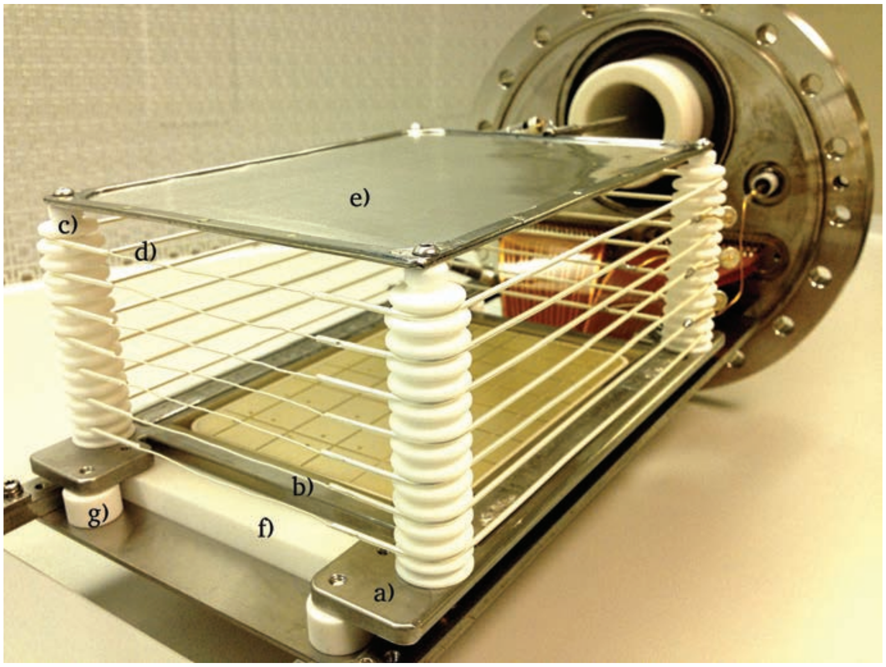

Figure 4.21-2. Assembled TPC for the 2014 run in the cleanroom of the PSI detector group. a) New composite grid with b) tungsten cross bars. A new high-voltage structure with c) simplified macor posts, d) silver-plated tungsten field wires, and e) silver cathode. The new grid design also implied a new support structure for the f) anode and the g) grid.

energies. An additional three days of data were collected at the reduced density with 28 K. A decrease in temperature should lead to a reduction in impurity captures and acts as a test for the in-situ measurement of gas impurities.

In summary, the 2014 production run was highly successful, accumulating over half of the statistics required for the target MuSun accuracy, as well as providing several datasets needed to study various systematic effects.

4.22 Determining the target gas purity

D. W. Hertzog, P. Kammel, D. J. Prindle, M. H. Murray, R. A. Ryan, and F. Wauters

The gas impurities of concern for the MuSun cryo-TPC are oxygen and nitrogen. With the capture rate of negative muons on these impurities much larger than on deuterium, the respective concentrations of O_2 and N_2 have to be be $\leqslant 3$ ppb and $\leqslant 1$ ppb. In addition, the expected nitrogen concentration at the vapor pressure at 31 K is still > 10 ppb. Our Circulating Hydrogen Ultrahigh Purification System (CHUPS)[1] continuously purifies the deuterium gas to the required level. For the 2014 run, the zeolite filters were equipped with temperature-controlled heaters, allowing online regeneration. The gas impurity level was stable during the entire run, and much lower compared to the 2013 run.

[1] V. A. Ghanza *et al.*, Nucl. Instrum. Meth A. **578**, 485 (2007).

To quantify the purity level of the deuterium gas, the MuSun experiment has a dual approach. A custom gas-chromatography system, developed by our collaborators from the Petersburg Nuclear Physics Institute, is directly connected to our TPC and CHUPS. After a careful calibration procedure and an upgrade of the readout system, the gas chromatography reached a sensitivity of ∼1 ppb this year. The uncertainty is dominated by the uncertainty of nitrogen and gas impurities introduced by the room-temperature gas system and sampling lines.

A complementary method to determine the level of chemical impurities is direct impurity detection in the TPC. Following muon capture on nitrogen or oxygen, the recoiling nucleus has a kinetic energy of $\mathcal{O}(100)$ keV, which yields a localized signal in the TPC. The dominant background in the relevant energy range comes from μd + d $\rightarrow {}^{3}$He + n muon-catalyzed fusion signals. These events are suppressed by a delayed time cut after the muon stop since the dominant fusion yield comes from the μd quartet state, which depopulates with a lifetime of ∼300 ns. In addition, the requirement that no Michel electron is associated with the event further suppresses the ^{3}He background, as the muon get recycled after the fusion process and most likely will undergo regular muon decay afterwards. The remaining fusion background is subtracted by taking the capture-free spectrum (events associated with Michel electrons) and normalizing it to the ^{3}He yield. At the increased impurity level of ∼20 ppb of nitrogen during the 2013 run, this in-situ method proved to be in excellent agreement with the gas chromatography (see Fig. 4.22-1). The improved energy resolution achieved by our new cryogenic preamplifiers[1] proved to be essential. The same analysis for the 2014 data shows that the impurity level of the 2014 run is at least 5 times lower than that of the previous year (see Fig. 4.22-1), which is confirmed by gas chromatography. The *residual* signal at this level is composed of impurity capture signals and a significant contribution of neutrons from μd captures. Before we can determine the impurity level with an accuracy of 1 ppb, this neutron background has to be quantified with input from the MuSun Monte-Carlo code.

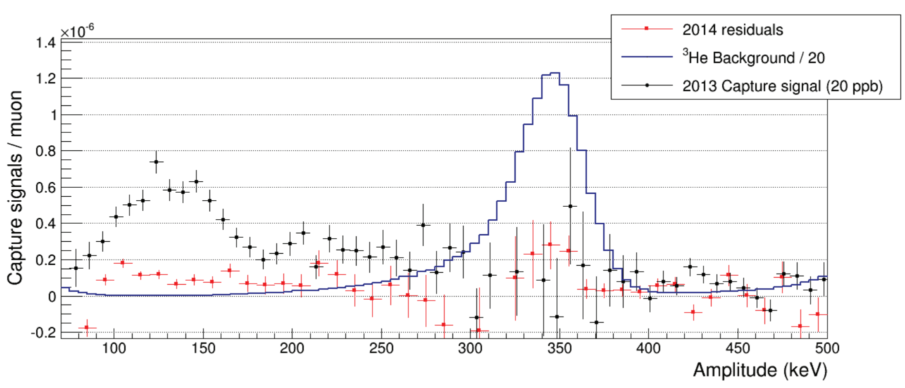

Figure 4.22-1. Comparison of the 2013 (black) and 2014 (red) capture recoil spectra. Ignoring any background contributions, the residual count in the 100-200 keV region corresponds to 2-3 ppb of nitrogen. In blue, the subtracted ^{3}He muon-catalyzed fusion background is shown.

In order to correct our lifetime measurement for muon captures on nitrogen, we need to

[1]R. A. Ryan *et al.*, J. Inst. **9**, P07029 (2014).

know the transfer rate of $\mu d \rightarrow \mu N$. In 2013, we doped our deuterium target with 2 ppm and 0.5 ppm of nitrogen. In addition to a clear capture yield in the TPC, orders of magnitude more intense than the production yield, the observed lifetime spectrum significantly deviated from a pure exponential. This allows us to extract the effective $\mu d \rightarrow \mu N$ transfer rate for high concentrations. Combining these transfer rates with the observed capture yield in the TPC for the doped and the production data, the effective transfer rate for the production data can be extracted. This procedure is independent of the TPC detection efficiency for μN captures. Fig. 4.22-2 shows this procedure for the 2013 data. This preliminary analysis implies a correction of 79(5) s^{-1}. A possible neutron background was ignored for this result, which can modify the correction up to 20%.

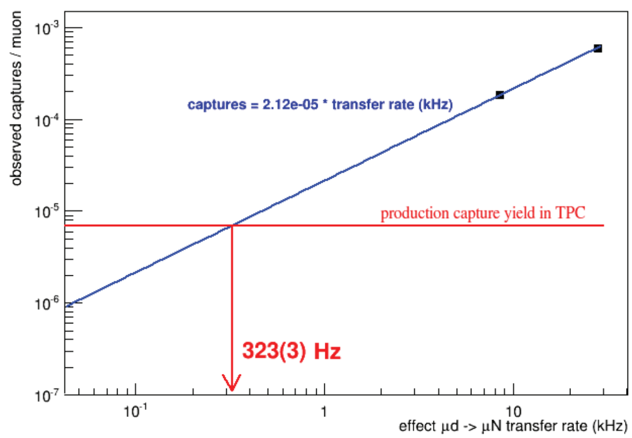

Figure 4.22-2. Extrapolation of the effective transfer rate $\mu d \rightarrow \mu N$ from the nitrogen-doped conditions to the production data level.

4.23 Muon tracking in the TPC

D. W. Hertzog, P. Kammel, M. H. Murray, D. J. Prindle, R. A. Ryan, and F. Wauters

One of the major sources of systematic error in the MuSun lifetime measurement is the interference of charged muon-catalyzed fusion products with the TPC tracking algorithms. Events selected as a fusion events have a later decay time than average and thus must not be treated differently than events without fusion. To minimize the effects of d + d fusion on the measured μ^- decay rate we make the muon stop definition as insensitive to the fusion products as possible. The most basic muon-tracking algorithm derives the muon stop coordinates from the most downstream anode pad in a cluster of pulses in the TPC. The Z and X coordinates are determined by the pad on which the charge pulse arrives, and the Y coordinate is calculated from the drift time. The deficiencies of this algorithm are that delayed fusion products can shift the reconstructed drift time (Y-coordinate) of the pulse, or deposit charge in a nearby pad, confusing the Z or X determination. A fiducial-volume cut combined with these coordinate shifts leads to acceptance or rejection due to muon-catalyzed fusion, distorting the time distribution of accepted muon decays. We have developed two tracking algorithms designed to be insensitive to the presence of fusion products, the *Threshold Tracker* and the *Upstream Tracker*.

The *Threshold Tracker* sets an energy threshold corresponding to the muon energy deposition near its Bragg peak and determines the Z-coordinate using the first pulse above this threshold. The X and Y coordinates are determined via projection of pulses upstream of this threshold pulse. This algorithm exhibits less fusion interference because the fusion products are likely to add energy to pulses that are already above threshold and because these pulses are not used to reconstruct the X or Y stop coordinates.

The *Upstream Tracker* fits the energy deposition in upstream pads to the muon Bragg curve to determine the Z-coordinate of the stop. This exploits the fact that the fusion products have a maximum range of 16 mm, which limits any extra energy deposition to the two most downstream pads. The X and Y coordinates are determined by projection in a similar manner to the *Threshold Tracker*.

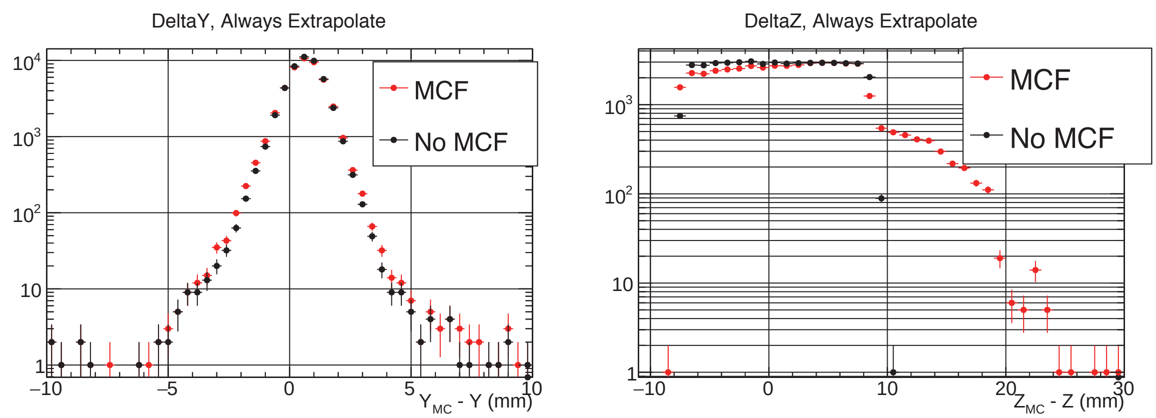

Figure 4.23-1. Comparison of reconstructed stop coordinate using the *Threshold Tracker* with truth information from simulated data that includes (red) or excludes (black) the energy deposition of muon-catalyzed fusion products. *Left:* Shows that any discrepancy due to fusion products is eliminated by projecting the stop Y-coordinate from upstream pulses. *Right:* Z-coordinate, shows the 16 mm anode pad structure and the large discrepancy introduced by fusions. The discrepancy in the X-coordinate (not shown) is also eliminated by the projection technique.

We study fusion interference in detail using Monte Carlo data samples in which we keep track of the essential Monte Carlo truth information. In particular, we run a parallel analysis on simulated data that include the energy deposition of fusion products, as well as on data that exclude this energy deposition in the TPC. Comparing the reconstruction mistakes made for data with and without fusion allows quantitative characterization of tracking algorithms. Using the event display, we develop an intuition for how fusion products influence the TPC response and the reconstruction. We compare the discrepancy between truth and reconstruction for the data with and without the response from fusion products to determine statistically how many mistakes are made because of fusion. Finally, we comprehensively examine the many ways an event can be reclassified by the fiducial-volume cut. We determine the fraction of events that change classification as a function of the time and type of the fusion reaction and the muon decay time. Using these analysis tools, we find that the improved tracking algorithms, *Threshold* and *Upstream*, reduce the fraction of fusion events affected by the fiducial-volume cut when compared to the most basic algorithm described Fig. 4.23-1. At present, these incorrectly rejected or accepted events represent a systematic error of 6 s^{-1} on the μd capture rate, which is comparable to the total precision goal for MuSun.

AlCap

4.24 Nuclear physics input in the search for charged lepton flavor violation, the AlCap experiment

D. W. Hertzog, R. Hong, P. Kammel, M. H. Murray, and F. Wauters

As the predicted charged-lepton flavor violation (CLFV) within the Standard Model including massive neutrinos is extremely small, the experimental observation of this process would be an unambiguous signal of new physics. Various extensions to the Standard Model predict CLFV rates that are within reach of next-generation experiments, probing new physics phenomena both at the grand unified theory and the TeV scale. Accordingly, searches for CLFV are high-priority programs in the worldwide searches for new physics. The Mu2e[1] (FNAL) and COMET[2] (J-PARC) experiments seek to determine the branching ratio for the charged-lepton flavor-violating process $\mu^- N \rightarrow e^- N$ to better than 10^{-16}, which is a factor of 10,000 improvement compared to the current best limit.

The AlCap experiment is a combined effort of the Mu2e and COMET collaborations to study important nuclear physics reactions in candidate target materials (Al, Ti), which are required to optimize the new muon-electron conversion experiments. Kammel is the US spokesman of this collaboration, based on his extensive experience with the relevant muon capture reactions.

The UW muon group has been a member of the Mu2e collaboration since it inception, but, because of its main commitments, has been careful to limit its involvement to targeted efforts where it has significant expertise, like the AlCap experiment. During 2013 the AlCap detector was built at CENPA, with most of the expensive detector components provided by the Mu2e and COMET projects. In 2013 the AlCap collaboration performed its first run (R2013) at PSI, focusing on work package WP1 with preliminary work done on WP2 and WP3.

Based on the analyses and good progress reported below, AlCap was approved for two more running periods at PSI in 2015. The goal of the first campaign is the measurement of gammas and neutrons from muon capture in aluminum and titanium (WP2 and WP3). The second campaign will corroborate the surprising findings of the proton experiment (WP1) in an upgraded set-up and extend the measurement to titanium.

[1] Mu2E collaboration, http://mu2e.fnal.gov.
[2] COMET collaboration: http://comet.kek.jp.

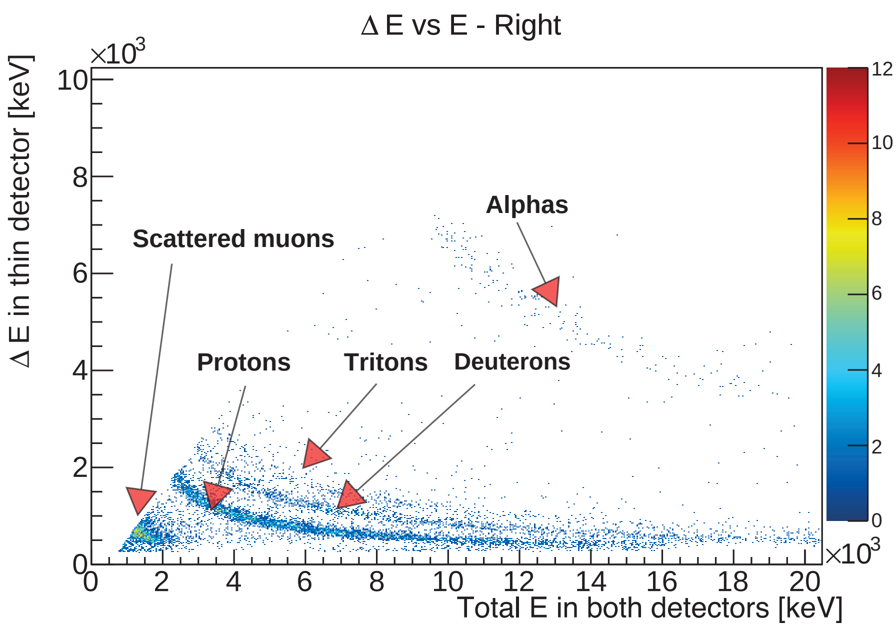

Figure 4.24-1. Particle identification of the capture products determined with the combination of the thin/thick silicon detector packages. On the y-axis is the energy deposited in the thin silicon detector and on the x-axis is the energy deposited in both the thin and the thick silicon layers. Each different particle band is annotated.

- **WP1: Charged-particle emission after muon capture.** The goal of WP1 is to measure the rate and spectrum of protons emitted after nuclear muon capture since, in both Mu2e and COMET Phase-I, the single-hit rate of these events in the tracking chamber could be significant. These protons have never had been measured in the relevant low energy regime of 2.5 to 15 MeV.

  In spite of the commissioning challenges in the 2013 run, the preliminary analysis presented in the first two AlCap Ph.D. Theses[1] led to the first physics result shown in Fig. 4.24-1. The result was both surprising and of high impact for the Mu2e and COMET Phase I designs. The preliminary emission fraction of protons after muon capture in aluminium was found to be about 2% in the energy range from 4 MeV to 8 MeV. The total proton emission fraction is estimated to be 3.5% if a simple description of the spectral shape holds.

  This is much smaller than the 15% emission measured in silicon, and smaller than the assumed 10-15% for aluminum which has been the basis for both designs up to now. If this preliminary result holds up, it will be possible to reduce the thickness of the proton absorbers in COMET and Mu2e, with a corresponding reduction in energy straggling and therefore improved energy resolution on conversion electron candidates. Indeed, no proton absorber might be needed at all for COMET Phase-I.

- **WP2: Gamma and X-ray emission after muon capture.**

  In R2013, the low energy X-ray and gamma-ray spectra were measured with a ger-

[1] Tran Nam (Osaka University, Japan) and A. W. J. Edmonds (University College London, UK).

manium detector. The measurement of the number of 2p–1s muonic X-ray transitions provides the number of stopped muons for the normalization of the spectra in R2013.

In addition, the full gamma-ray spectra can provide a wealth of information from the peaks associated with muon capture and are being evaluated for their use as alternative means of monitoring the number of stopped muons in the full Mu2e and COMET experiments.

A new INFN group joined the collaboration, and will bring a stand-alone 5×5 LYSO array calorimeter which will allow them to parasitically measure the high-energy photon spectrum produced by stopped muons. This will provide information on the spectrum that can be expected in the Mu2e and COMET calorimeters, and also will allow an evaluation of the use of high-energy photons for normalization in Mu2e or COMET.

- **WP3: Neutron emission after muon capture.** Neutron emission after muon capture, i.e. $\mu^- + N(Z, A) \rightarrow n + N(Z-1, A-1)$, is governed by the weak interaction. The distribution of neutron energies with emission greater than 10 MeV can explained by a statistical model with an effective temperature parameter. However, at lower energies the residual nuclear particle-hole states can excite giant dipole resonances, and these potentially dominate emission. Previous emission spectra were obtained on selected nuclear targets 30–40 years ago and are of low quality and low statistics. Better emission data and nuclear models are important to develop Monte Carlo codes (like FLUKA) to become predictive at the required level. Neutron emission from the stopping target is an important background to be understood and controlled. For example, the MC-predicted gamma background from neutron capture in the proton attenuation shield surrounding the target caused it to be redesigned. Also as the front-end electronic systems are placed within the detector solenoid, neutron-induced single-event-upsets in the readout electronics require detailed attention.

5 Axion searches

ADMX (Axion Dark Matter eXperiment)[1]

5.1 Status of ADMX

C. Boutan, M. Hotz, H. LeTourneau, D. Lyapustin, A. Malagon, C. Plesha,
L. J Rosenberg, G. Rybka, J.V. Sloan, A. Wagner, and D. I. Will

The Axion Dark Matter eXperiment (ADMX) is a large-scale RF-cavity search for galactic dark-matter axions. The ADMX collaboration has operated a series of dark-matter axion searches since the mid-1990s, the most recent of which was installed at CENPA in 2010. Installation of the experimental apparatus was completed in late 2013 and operation of the experiment began soon afterward, resulting in axion exclusion limits in two frequency regimes. Upgrades to install a dilution refrigerator to achieve 100 mK operating temperatures began in fall of 2014; at the time of writing, April 2015, the dilution refrigerator and associated components had arrived and were being integrated into the experiment. With the addition of the dilution refrigerator, ADMX will enter phase "Gen 2." ADMX is currently searching for dark-matter axions in the range of 10 μeV, with a series of cryogenic and amplifier upgrades planned to improve the sensitivity and search rate of the experiment over the next year.

Figure 5.1-1. Progress of ADMX experiment site at CENPA. *Left:* Experiment site April 2015, showing, clockwise from top, cleanroom with experimental insert, data-acquisition system, dunkstand for testing cryogenic amplifiers, helium liquefaction system, and black test cryostat for dilution refrigerator. *Right:* Pumps, control system, and gas handling system for dilution refrigerator in foreground. Copper ^{3}He/^{4}He mixture pumping line installed by CENPA engineer Tom Burritt visible by the ADMX main magnet in background.

The axion was postulated three decades ago to explain why QCD conserves the discrete symmetries P (parity) and CP (charge conjugation times parity). The amount of CP violation in QCD is encoded in a phase θ which appears in the QCD Lagrangian. When θ differs from zero, QCD violates P and CP. Since the strong interactions appear to be P-

[1] ADMX is supported by the DOE Office of High-Energy Physics and makes use of CENPA resources by recharge to the cost center.

and CP-symmetric in the laboratory, θ must be very small; the upper limit on the neutron electric-dipole moment requires $|\theta| < 10^{-10}$. However, in the Standard Model, P- and CP-violation by the weak interactions feeds into the strong interactions so that the expected value of θ is of order unity. The inability of the Standard Model to account for P- and CP-conservation by the strong interactions is called the "strong CP problem". Peccei and Quinn proposed a solution to this problem in which the Standard Model is modified so that θ becomes a dynamical field and relaxes to zero, thus conserving CP in a natural way[1]. The theory's underlying broken continuous symmetry dictates the existence of a particle: the axion. The axion is the quantum of oscillation of the θ field and has zero spin, zero electric charge, and negative intrinsic parity. So, like the neutral pion, the axion can decay into two photons. Soon after the initial proposal of the axion, it was realized axions of certain masses are ideal dark-matter candidates. Experiments and astronomical observations have since constrained the axion to a finite mass range in which the axion contributes a significant portion of dark matter; this mass range corresponds to microwave photons.

ADMX operates by stimulating the decay of galactic dark-matter halo axions into photons via Primakoff conversion and detecting the resulting photons. The experiment consists of a large tunable microwave cavity immersed in a static magnetic field; the resonance of the cavity further enhances the conversion, and the resonance is tuned to search for axions of varying mass. An RF receiver records the power spectrum of the cavity for each tuning configuration as ADMX scans in frequency. However, despite the prodigious predicted local density of dark-matter axions (approximately 10^{14}/cc), the expected electromagnetic signal would be extraordinarily weak, around 10^{-23} W in the ADMX apparatus. Our present ADMX collaboration (University of Washington, LLNL, University of Florida, University of Sheffield, NRAO and University of California Berkeley) has constructed and is operating a large-scale dark-matter axion experiment that is the first, and presently only, experiment sensitive to plausible dark-matter axions.

ADMX is essentially an extraordinarily low-noise radio receiver with a tunable RF cavity forming a tuned tank circuit. A short electric-field probe couples power from the cavity into a cryogenic amplifier which is cooled to near the cavity temperature.

The dominant background in ADMX comes from thermal noise; the system noise temperature is the noise temperature of the amplifier plus the cavity physical temperature. The motivation for lowering the system noise temperature is clear: (i) for a given axion-photon coupling, the frequency scan rate decreases as the square of the system temperature and (ii) for a given scan rate, the power sensitivity increases as the system temperature drops. ADMX reduces its thermal noise by using low-noise first-stage amplifiers and cooling the cavity. ADMX collaboration members developed SQUID amplifiers in the $100 - 1000$ MHz range specifically for ADMX; this development allowed more than an order-of-magnitude reduction in system noise temperature.

The previous version of ADMX, ADMX Phase 1, was located at LLNL and operated from 2002 – 2009. The Phase 1 apparatus was fitted with superconducting quantum interference device (SQUID) amplifiers and operated at about 2 K physical temperature via a pumped

[1] R. D. Peccei and H. R. Quinn, Phys. Rev. Lett. **38**, 1440 (1977).

Figure 5.1-2. *Left:* ADMX dilution refrigerator hanging next to insert in clean room. *Right:* Extraction of ADMX insert after successful commissioning, late 2013.

^{4}He system. ADMX Phase 1 completed a scan of the $1.9 - 3.5$ μeV axion-mass range and the results for conservative estimates of dark-matter density were published. After further analysis the ADMX collaboration published a search for axions assuming a non-virialized dark-matter distribution within our galaxy[1].

Starting in 2010, ADMX was entirely redesigned and rebuilt at CENPA. Over the past year, ADMX completed several data runs, set new axion coupling exclusion limits, underwent a series of site modifications to accommodate the dilution refrigerator, began installing the dilution refrigerator, and procured Josephson Parametric Amplifiers (JPAs) for use as first-stage amplifiers. ADMX collaborators at the University of California Berkeley provided the nearly quantum-limited JPAs for axion searches in higher frequency ranges currently inaccessible to SQUID amplifiers. The dilution refrigerator will cool the cavity and amplifiers to approximately 100 mK; no existing alternative refrigeration technique could achieve lower continuous temperatures for ADMX. In summer 2014, ADMX received funding for its Gen 2 operations from the DOE/NSF and, along with SuperCDMS and LUZ-Zeplin, is one of three US dark-matter experiments to receive next-generation funding. With the dilution refrigerator, ADMX will be operating in phase "Gen 2."

The 2013-2014 data runs of ADMX (hereforth referred to as the 2014 data runs, for brevity) were the first data collected by ADMX at CENPA. Throughout the 2014 data runs, ADMX employed SQUID amplification and a pumped ^{4}He system achieving physical temperatures of about 1.2 K. The 2014 data runs demonstrated full functionality of the new ADMX design and success of the closed-loop helium liquefaction system in maintaining ADMX op-

[1] J. Hoskins *et al.*, Phys. Rev. D **84**, 121302(R) (2011).

erations throughout extended data runs on the order of months. New axion exclusion limits were set in two frequency regimes: $600-720$ MHz and $1050-1400$ MHz, with KSVZ sensitivity in select frequency ranges. Data was simultaneously collected using the TM_{010} and TM_{020} modes; this is the first time an axion haloscope has taken data through two independent receiver chains simultaneously and the first time a nonfundamental cavity mode achieved sensitivity to plausible QCD axions. The 2014 data runs were carefully analyzed in the Ph.D. thesis of Dr. Dmitry Lyapustin, who successfully defended his thesis in March 2015.

In addition to the operation and improvements of the main experiment, in the previous year ADMX has expanded its R&D efforts. ADMX Sidecar, a $3.5-6$ GHz cavity designed to fit in an otherwise unused space of the main ADMX insert, is nearly constructed and will be included in the next ADMX data runs. Sidecar is tuned with piezo electric motors and uses its own independent receiver chain, and is projected to be sensitive to plausible QCD dark-matter axions. The space in which Sidecar resides in the main experiment allows a trivial extension of Sidecar to cover a range from $2-10$ GHz. The Orpheus experiment demonstrated the feasibility of a novel detector architecture consisting of an open Fabry-Pérot resonator and a series of current-carrying wire planes that generate a varying magnetic field. Results from the Orpheus experiment, as well as the projected sensitivity of the technique, were published[1]; the open resonator design is a promising candidate for higher-mass dark-matter QCD axion searches from about $50-420$ μeV, or $15-120$ GHz. Select ongoing ADMX R&D projects at UW include Ouroboros, an active feedback resonator to artificially the cavity Q, and Electric Tiger, a rectangular cavity design for use with dipole magnets.

With the addition of the dilution refrigerator, ADMX Gen 2 will take data at an unprecedented frequency scan rate, over 100 times faster than during the 2014 data runs. With the addition of JPAs for use with ADMX Sidecar and the higher frequency channel of the main ADMX cavity, ADMX is equipped for sensitivity to even the most pessimistically coupled dark-matter QCD axions over an extended frequency range. Further, ADMX will take data simultaneously in three frequency regimes. The Gen 2 data run should begin in fall 2015, and ADMX is on track to discover or exclude the dark-matter QCD axion.

[1] G. Rybka *et al.*, Phys. Rev. D **91**, 011701(R) (2015).

6 Relativistic Heavy Ions

6.1 UW URHI program overview

T. A. Trainor

The UW program has addressed the structure and interpretation of hadron yields, spectra, correlations and fluctuations from RHIC p-p and Au-Au collisions. Our consistent finding over the past decade has been that minimum-bias (MB) dijets continue to play a major role in all high-energy nuclear collisions. Almost all RHIC data near mid-rapidity are described accurately by a three-component model (TCM): (a) longitudinal dissociation of projectile nucleons (soft), (b) fragmentation of large-angle-scattered low-x partons (gluons) to dijets (hard), and (c) a nonjet (NJ) azimuth quadrupole conventionally interpreted to represent "elliptic flow." Recently we have applied our methods to LHC data with similar results. A theoretical study of trigger-associated (TA) correlations from 200 GeV p-p collisions describes the 2D TA hard component quantitatively in terms of a MB jet spectrum folded with published p-$\bar{\text{p}}$ fragmentation functions[1], buttressing spectrum and angular-correlations studies with similar conclusions: MB dijets dominate higher-multiplicity p-p collisions.

Section 6.2 reexamines the systematics of published centrality-averaged p_t-differential $v_2(p_t)$ data for identified hadrons in terms of a source-boost distribution and a quadrupole spectrum. We find that $v_2(p_t)$ data for identified hadrons reveal a source-boost (transverse-speed) distribution consistent with a *single value*, strongly contradicting hydrodynamic descriptions of a bulk medium undergoing Hubble expansion with its broad boost distribution. Section 6.3 pursues the centrality dependence of the quadrupole source boost and finds no significant boost increase with Au-Au centrality, dramatically in conflict with expectations for larger energy densities and pressure gradients in more-central A-A collisions. We find that NJ quadrupole systematics are incompatible with hydrodynamic (flow) expectations.

Section 6.4 addresses recently-reported analysis of event-wise mean p_t fluctuations from LHC p-p collisions at several energies[2]. The data are accurately described by a two-component model featuring a large dijet component. Sections 6.5 and 6.6 obtain similar results for Pb-Pb collisions, comparable to our previous analysis of 200 GeV Au-Au data from the RHIC.

Sections 6.7 and 6.8 address conventional analysis of 1D azimuth projections of 2D angular correlations in which the projected data are fitted with Fourier series interpreted as representing "harmonic flows." Bayesian-inference (BI) methods applied to several data models strongly reject Fourier-series (FS) models and strongly favor a model including peaks at 0 and π.[3] We conclude that BI preference for the latter model is based on its *predictivity*, that it can be falsified by data, whereas FS models are not predictive, that is, they cannot be falsified.

Various results over the years indicate that deliberate choices of measures and physical

[1] T. A. Trainor, arXiv:1407.6422.
[2] T. A. Trainor, arXiv:1503.02197.
[3] M. B. De Kock, H. C. Eggers and T. A. Trainor, arXiv:1502.04475.

assumptions can lead to dramatically different conclusions drawn from the same particle data, ranging from dominance of in-vacuum dijets to formation of a flowing, dense QCD medium. To resolve such confict requires careful examination of and comparisons among methods and assumptions in the context of QCD as the theory describing high-energy nuclear collisions.

6.2 Evidence against "elliptic flow" derived from $v_2(p_t)$ data

T. A. Trainor

Claims of "elliptic flow" at the SPS, RHIC and LHC are based on a hydrodynamic model of A-A collisions in which almost all hadrons emerge from "freezeout" of a thermalized flowing bulk medium quark-gluon plasma (QGP). The final-state hadron spectrum for non-central collisions then has a *quadrupole* azimuth dependence conventionally measured by parameter $v_2 \approx \langle\cos(2\phi)\rangle$ relative to the A-A reaction plane. v_2 data are used to support claims for formation of a "perfect liquid" in RHIC collisions. Fig. 6.2-1 (first) shows $v_2(p_t)$ data for three hadron species vs p_t. The p_t dependence of $v_2(p_t)$ is a critical issue. Assuming "ideal hydro" conditions (thermalized system, Maxwell-Boltzmann spectrum) and the Cooper-Frye formalism the three curves extending off the top of the panel are $v_2 \propto p_t'$ (p_t' is p_t in the boost frame) reflecting the expected ideal-hydro trend for a *single* source-boost value $\Delta y_{t0} = 0.6$ (emission from an expanding thin cylindrical shell) describing the data for $p_t < 1.5$ GeV/c. There remains the question of the boost *distribution*. For Hubble expansion of a bulk medium the boost distribution should be broad, extending from zero to some maximum. Fig. 6.2-1 (second) shows the same data divided by $p_t(lab)$ and plotted on transverse rapidity y_t with proper mass for each hadron species. All data pass through a common zero intercept at $\Delta y_{t0} = 0.6$. The curves approaching a constant value at larger y_t represent an ideal-hydro assumption.

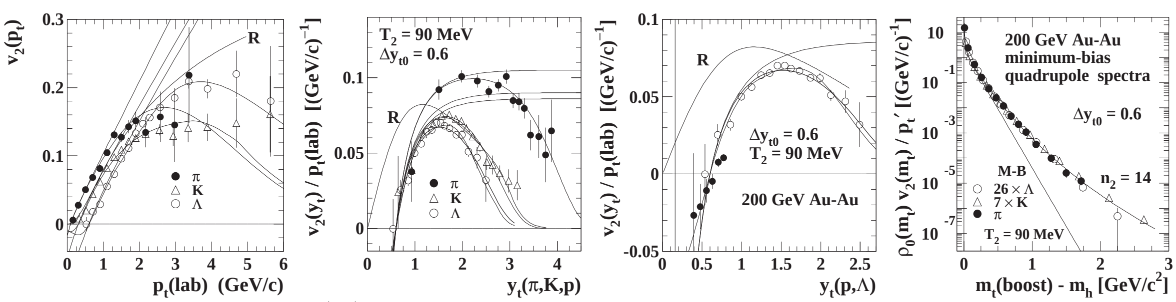

Figure 6.2-1. First: $v_2(p_t)$ data for three hadron species plotted in conventional format. Second: The same data plotted on transverse rapidity. Third: λ data and dash-dotted model curves compared to hydro theory (dotted curve R). Fourth: Quadrupole data transformed to a common m_t' spectrum modeled by a Lévy distribution (solid curve).

Fig. 6.2-1 (third) shows an expanded view for Λ hadrons compared to a viscous-hydro theory curve for protons (dotted curve R in three panels). The theory curve represents a broad boost distribution consistent with hydro assumptions for Hubble expansion and is dramatically falsified by the $v_2(p_t)$ data. The theory reduction below a flat ideal-hydro trend at larger y_t (e.g. the upper dash-dotted curve) is presumably the result of a finite viscosity in the model. Fig. 6.2-1 (fourth) shows data from the second panel multiplied by spectra $\rho_0(y_t)$ for each hadron species and divided by p_t' in the boost frame rather than p_t in the lab frame. The results are then "boosted" (shifted on y_t) from lab to boost frame, transformed to $m_t' - m_h$, and scaled with factors indicated in the plot. The solid curve is a Lévy distribution with the parameters indicated. Up to an overall constant three numbers, $\Delta y_{t0} = 0.6$, $T_2 = 90$ MeV and $n_2 = 14$ accurately describe all $v_2(p_t)$ data for three hadron species. The few hadrons associated with the azimuth quadrupole follow a unique spectrum representing not a Hubble-expanding bulk medium but rather a thin shell expanding with one radial speed.

6.3 No centrality dependence for azimuth-quadrupole source boost

D. T. Kettler*, D. J. Prindle, and T. A. Trainor

The previous article indicates that *minimum-bias* (MB) $v_2(p_t)$ data (averaged over Au-Au centrality) for several identified hadron species can be described in the boost frame by a single universal m_t spectrum in the form of a Lévy distribution $A/[1 + (m_t - m_h)/nT]^n$ and that the source boost distribution is consistent with a single boost value $\Delta y_{t0} = 0.6$ for the MB Au-Au event ensemble. Within the flow narrative a mean source boost should increase with A-A centrality, reflecting increased initial-state energy densities and pressure gradients. Fig. 6.3-1 (first) shows $B_Q\{2D\}(y_t, b) = v_2^2(y_t, b)$ data for seven centralities of 200 GeV Au-Au collisions. The second panel shows the same data in the form $v_2(y_t)/p_t(\text{lab})$ comparable to the pion data in the second panel of the previous article. The spectrum-weighted distribution for each centrality is normalized to unity. The four more peripheral centralities follow the MB shape within data uncertainties. The more-central data exhibit an increasing shift to *smaller* rapidities, and the 0-5% data (not shown) are consistent with zero with a small upper limit. Most importantly, there is no indication of an increase in the quadrupole source boost with Au-Au centrality. The data are generally consistent with the MB identified-hadron $v_2(p_t)$ data. Fig. 6.3-1 (third) shows 62 GeV data in the same format, with similar results.

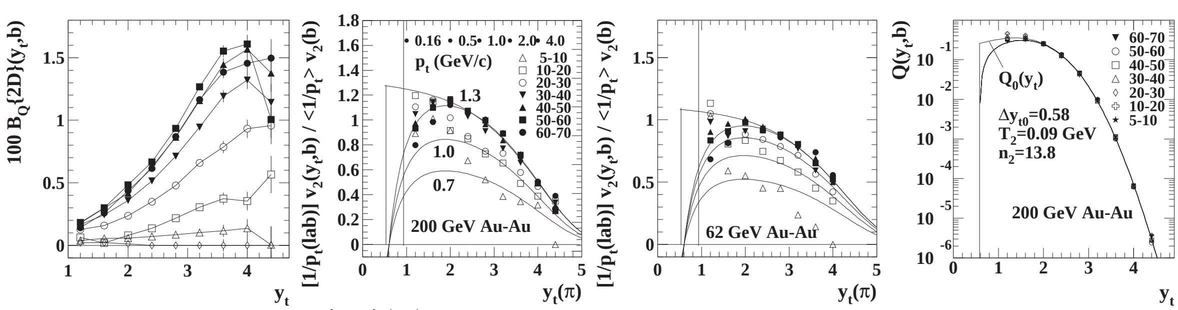

Figure 6.3-1. First: $B_Q\{2D\}(y_t)$ data obtained by 2D model fits. Second: 200 GeV Au-Au unit-normal $v_2(y_t)/p_t(\text{lab})$ distributions. Third: The same for 62 GeV Au-Au. Fourth: Unit-normal quadrupole spectra for six Au-Au centralities showing no boost variation.

Fig. 6.3-1 (fourth) shows unit-normal quadrupole spectra obtained from the $v_2(y_t, b)$ data for six 200 GeV Au-Au centralities as described in the previous article. The dashed curve labeled $Q_0(y_t)$ is the Lévy distribution from the previous article (for pions approximating

*Graduated December, 2013.

unidentified hadrons) transformed to the lab frame. The curve is not fitted to the data. The quadrupole source boost shows no dependence on Au-Au centrality. Within the hydro narrative almost all hadrons should emerge from a flowing bulk medium as the common hadron source. The transverse-velocity β_t distribution (the basic prediction of hydro theory) should manifest as a broad boost distribution on y_t. The spectrum common to almost all hadrons should correspond to the source boost distribution: approximating Hubble expansion with quadrupole modulation for non-central A-A collisions. The boost distribution should change with increasing centrality to reflect increased pressure gradients and perhaps a modified equation of state. We observe that all of those hydro expectations are contradicted by $v_2(p_t)$ data. In addition, a dramatic change (sharp transition) in dijet characteristics near 50% centrality in Au-Au collisions, which might reflect a major change in bulk-medium presence and/or properties, has no correspondence in any quadrupole v_2 data.

6.4 p-p event-wise mean-p_t fluctuations at LHC energies

T. A. Trainor

A recent LHC study of event-wise mean p_t (denoted by $\langle p_t \rangle$) fluctuations in p-p collisions vs charge multiplicity n_{ch} employed an r.m.s. ratio fluctuation measure denoted by $\sqrt{C}/\bar{p}_t$. An alternative measure is variance difference $B \equiv \sigma^2_{P_t|n_{ch}} - n_{ch}\sigma^2_{p_t}$ representing the *variance excess* of P_t (total p_t in some angular acceptance) given n_{ch} (in the same acceptance) relative to a statistical reference, with $\bar{p}_t = \bar{P}_t/n_{ch}$. Then $C \approx B/n_{ch}^2$ and $\sqrt{C}/\bar{p}_t \approx \sqrt{B}/\bar{P}_t$.

Fig. 6.4-1 (first) shows published LHC fluctuation data for p-p collisions summarized as decreasing according to a power-law trend $\propto 1/n_{ch}^{0.4}$ and with *negligible collision-energy dependence* (mpt′ denotes $\bar{p}'_t$ biased by a low-p_t acceptance cutoff). The second panel shows the same data in a format that may be compared with initial RHIC p_t fluctuation analyses. The systematics of $\bar{p}'_t$ vs n_{ch} and energy have been reported in a previous analysis[1] and can be used to transform the LHC fluctuation data to variance difference B as in the third panel.

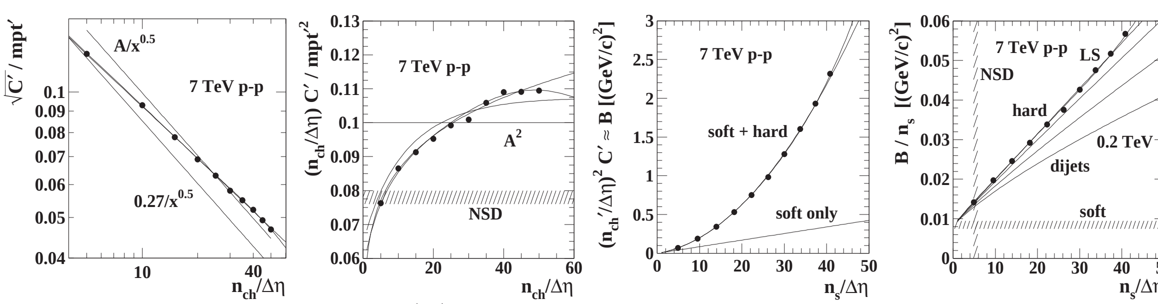

Figure 6.4-1. First: Published $\langle p_t \rangle$ fluctuation data for 7 TeV p-p collisions. Second: The same data in an alternative format. Third: The published data transformed to variance difference B. Fourth: B/n_s accurately follows a linear TCM trend.

The dashed curve in the third panel is a two-component (soft + hard) model (TCM)

[1] T. A. Trainor, Phys. Rev. C **90**, 024909 (2014).

describing fluctuation data in the B format (b_s and b_h are fixed model parameters)

$$B(n_{ch}) \;\; = \;\; n_s b_s + n_h b_h \tag{1}$$

with relations $n_{ch} = n_s + n_h$ and $n_h = 0.006\, n_s^2$ derived from a previous analysis of p-p p_t spectrum data vs n_{ch} in which n_h represents the number of *hadron fragments from minimum-bias dijets* within the angular acceptance. That expression defines the dashed curves in the four panels. The accuracy of the TCM data description is demonstrated in the fourth panel where B/n_s data closely follow the linear TCM trajectory $b_s + 0.006 n_s b_h$. The dash-dotted curves show the strong energy dependence of B implied by the previously determined energy dependence of $\bar{p}_t(n_{ch}, \sqrt{s})$. Additional energy dependence may arise from b_h in the TCM. Those results clearly demonstrate that a dijet contribution fully compatible with QCD in elementary hadronic collisions dominates p_t fluctuations in LHC p-p collisions. The data presentation in the first panel is based on the choice of an intensive r.m.s. ratio of extensive measures leading to minimization of evidence for dijets. A conventional fluctuation measure based on variances of extensive quantities clearly reveals the dominant dijet contribution. The claimed lack of energy dependence is based on a ratio of related extensive variables taken in an intensive combination that leads to near cancellation of dijet energy trends.

6.5 LHC Pb-Pb event-wise mean-p_t fluctuations at 2.76 TeV

T. A. Trainor

Fluctuation measurements in A-A collisions at the SPS, RHIC and now the LHC have been motivated by searches for "critical" fluctuations expected near the conjectured QCD phase boundary separating a quark-gluon plasma (QGP) phase from a hadron-fluid phase. Event-wise mean-p_t ($\langle p_t \rangle$) is interpreted as a proxy for local temperature T, and $C \approx \sigma^2_{\langle p_t \rangle} - \sigma^2_{p_t}/n_{ch}$ is said to measure excess fluctuations. The ratio $\sqrt{C}/\bar{p}_t$ should then represent $\delta T/\bar{T}$, an r.m.s. measure of fluctuation "strength." Fig. 6.5-1 (first) shows data for 2.76 TeV Pb-Pb collisions vs charge density $n_{ch}/\Delta\eta$. Because $\sqrt{C}/\bar{p}_t$ is found to vary approximately as a "power law" $\propto n_{ch}^{-0.5}$ (see previous article) the data have been scaled by factor $n_{ch}^{0.5}$. Relative to the power-law reference trend the Pb-Pb data seem to follow a p-p trend at lower multiplicities, increase strongly above that trend in an intermediate region and then fall off at the highest multiplicities. It is concluded that (a) there is no evidence for critical fluctuations, (b) there is no significant energy dependence (e.g. compared to RHIC data) and (c) the data are consistent with Monte Carlo models incorporating collective phenomena.

Based on previously-reported results for n_{ch} and energy dependence of $\bar{p}_t'$ (mpt$'$ in the plots) those data are first converted to a form comparable to initial p_t fluctuation measurements at the RHIC (second) and then to the form $(2/N_{part})B$ (third) vs A-A centrality measure $\nu = 2N_{bin}/N_{part}$. The latter data are found to follow a Glauber linear superposition (GLS) trend (dashed line) for more peripheral data ($\nu < 2.5$), but rise above the GLS reference for more central data and then fall slightly for the most central data. That result can be compared with RHIC measurements for 200 GeV Au-Au collisions (fourth) that show the same general trend but with an amplitude about five-fold lower. It was previously demonstrated for 200 GeV Au-Au p_t fluctuation data that the increase following the

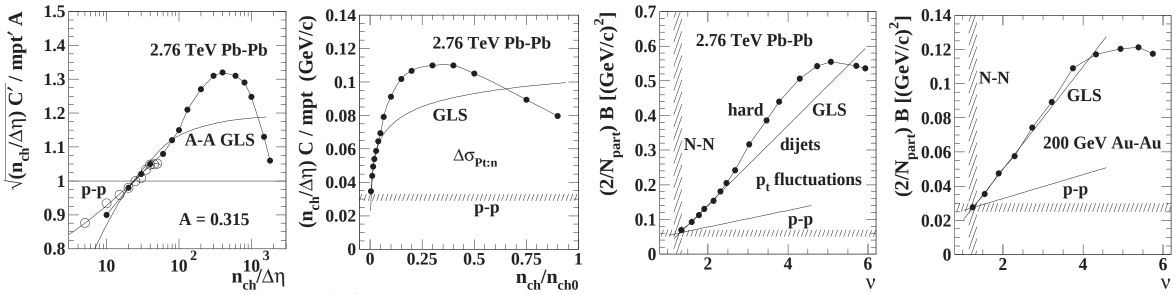

Figure 6.5-1. First: $\langle p_t \rangle$ fluctuation data for 2.76 TeV Pb-Pb collisions in the form $\sqrt{n_{ch}C}/\bar{p}_t$. Second: Those data converted to a form comparable to initial RHIC fluctuation data. Third: The same data converted to extensive fluctuation measure $(2/N_{part})B$ vs A-A centrality measure ν. Fourth: Comparable data for 200 GeV Au-Au collisions.

GLS trend is entirely due to a dominant dijet contribution in transparent A-A collisions (corresponding number and p_t angular correlations include clear dijet contributions as the dominant features). The GLS trend $\propto\nu$ for per-participant measure $(2/N_{part})B$ indicates the binary-collision scaling $B\propto N_{bin}$ expected for dijet production. As for p-p fluctuation data described in the previous article the choice of intensive ratio measure $\sqrt{C}/\bar{p}_t$ obscures the dijet contribution. The extensive fluctuation measure B reveals clear indications of the dijet contribution to Pb-Pb collisions and the strong energy dependence from RHIC to LHC collision energies.

6.6 LHC Pb-Pb p_t fluctuations vs Monte Carlo models

T. A. Trainor

Recent measurements of $\langle p_t \rangle$ fluctuations in 2.76 TeV Pb-Pb collisions at the LHC have been compared to the Monte Carlo (MC) models HIJING and AMPT. HIJING is a straightforward model of A-A collisions in which nucleon-nucleon (N-N) collisions generated by the PYTHIA MC model are linearly superposed according to a Glauber model of A-A collision geometry that assumes the eikonal approximation. In that case soft hadron production is $\propto N_{part}$ and hard hadron (dijet) production is $\propto N_{bin} \sim N_{part}^{4/3}$. The default AMPT MC incorporates HIJING to provide initial conditions [soft longitudinal strings and (semi)hard-scattered partons] and then rescatters partons and hadrons to model "collectivity" (flows).

Fig. 6.6-1 (first) shows fluctuation data in the form $B/n_{ch} \approx \Delta\sigma^2_{P_t|n_{ch}}$, where the latter "per-particle" measure was used in several previous RHIC analyses. The HIJING MC data are in the same format and disagree dramatically with the LHC data. That result can be compared with earlier RHIC analyses (second) that yield similar results, albeit with reduced overall amplitudes at the lower collision energy as expected for dijet production. The HIJING trend was explained in the RHIC analysis as follows: The HIJING Glauber model is correctly applied, but the PYTHIA model of N-N collisions is incorrect. PYTHIA produces a substantial excess of very low-energy scattered partons that contribute strongly to the hard component of n_{ch} but weakly to correlations and fluctuations as for B. The per-particle measure B/n_{ch} does not then scale strongly (or at all) with $2N_{bin}/N_{part} = \nu$ as do the data from

Pb-Pb collisions. The PYTHIA model of p-p (N-N) collisions assumes the eikonal model that is not valid for that case. The eikonal model predicts that $n_h \propto n_s^{4/3}$ instead of observed n_s^2.

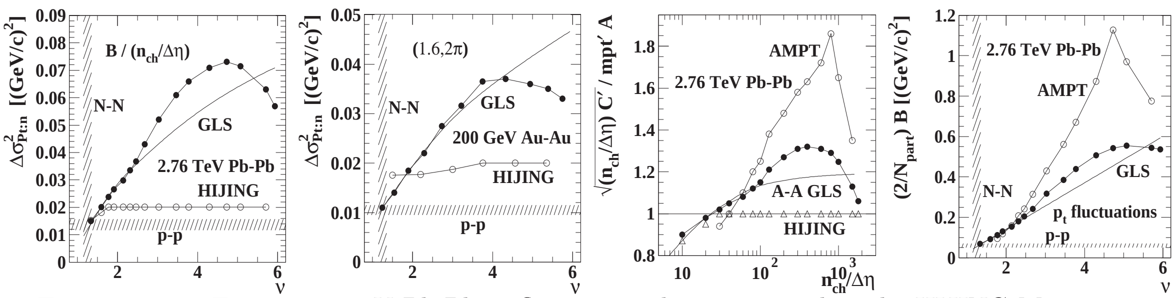

Figure 6.6-1. First: 2.76 TeV Pb-Pb p_t fluctuation data compared to the HIJING Monte Carlo. Second: The same trends for 200 GeV Au-Au collisions. Third: Comparison of AMPT and HIJING MC data to published LHC measurements. Fourth: AMPT-data comparison in a per-participant format. AMPT and HIJING have the same $\bar{p}_t(n_{ch})$ trend.

Fig. 6.6-1 (third) shows default AMPT MC results compared to Pb-Pb data. That the MC data greatly exceed the measurements for more-central Pb-Pb collisions is difficult to understand given that HIJING supplies the initial conditions for AMPT. Rescattering should act to decrease correlations. The dashed curves (GLS trend) represent the chief QCD mechanism for momentum transport from longitudinal to transverse phase space in the form of large-angle scattering of partons initially residing in projectile nucleons. For the stated reasons HIJING (PYTHIA) does not model that process correctly.

6.7 Bayesian inference and 200 GeV Au-Au azimuth-correlation models

M. B. De Kock*, H. C. Eggers*, and T. A. Trainor

Bayesian Inference (BI) addresses the problem of relating parameterized data models to available data in an optimal manner. BI model evaluation is based on *Bayes' theorem*

$$p(w|D^*H) \quad = \quad \frac{L(D^*|wH)}{E(D^*|H)} p(w|H), \tag{1}$$

read as "posterior PDF on model parameters w is derived from prior PDF given data D^*, likelihood L and evidence E." Given data values D^* the best set of parameter values $\tilde{w}$ for each model is determined based on the *likelihood* function L. Candidate models are compared based on evidence E. The most plausible model produces the largest evidence. If likelihood L is a peaked function on K-dimensional parameter space w, the evidence E is defined by

$$E(D^*|H) \quad \approx \quad L(D^*|\tilde{w}H)\sqrt{(2\pi)^K \det C_K}\, p(\tilde{w}|H), \tag{2}$$

where $L(D^*|\tilde{w}H) \propto \exp(-\chi^2/2)$ is the maximum likelihood and $C_K(D^*|\tilde{w}H)$ is the covariance matrix for data model H [function $D(w)$ with K parameters]. The information I is defined

*Stellenbosch University and National Institute for Theoretical Physics, Stellenbosch, South Africa.

by

$$I(D^*|H) \quad = \quad -\ln\left[\sqrt{(2\pi)^K \det C_K}\; p(\tilde{w}|H)\right]. \tag{3}$$

The evidence is then $E(D^*|H) \propto \exp[-(\chi^2/2 + I)]$. In general, χ^2 decreases and I increases as parameter number K increases. An alternative data representation is the power spectrum

$$P_m \quad = \quad \frac{1}{N} \sum_{n'=0}^{N-1} \cos(m\phi_{n'}) A(\phi_{n'}), \tag{4}$$

a Fourier transform of the periodic azimuth autocorrelation $A(\phi_n)$ (data histogram) wherein signal and noise components can be distinguished. A "basic model" for data is defined by

$$A(\phi_\Delta) \quad = \quad A_{1D}\left\{\exp\left[-\frac{1}{2}\left(\frac{\phi_\Delta}{\sigma_{\phi_\Delta}}\right)^2\right] - \sigma_{\phi_\Delta}/\sqrt{2\pi}\right\} - A'_{\rm D} 2\cos(\phi_\Delta), \tag{5}$$

where two model components (SS Gaussian and AS dipole defined below) integrate to zero over 2π. We first apply BI methods to the 1D azimuth projection from 0-5% central 200 GeV Au-Au collisions. We fit the data with the basic model and obtain the data power spectrum. We determine χ^2 and information I for Fourier series (FS)-only models vs parameter number K. We then evaluate evidence E for several competing models and determine the model preferred by BI methods. Fig. 6.7-1 (first) shows the $K = 3$ basic model fitted to central Au-Au data with its two peak features represented by a same-side (SS) Gaussian and away-side (AS) dipole. The power spectrum P_m in the second panel has a white-noise component fluctuating about 0.001 and a signal component consisting of a Gaussian on index m (Fourier transform of the SS Gaussian on ϕ) and a single value at $m = 1$ representing the AS dipole. The third panel shows fit results for various (FS) models with K parameters. The fit χ^2 (upper solid curve) decreases until it meets the noise trend (lower solid curve). Information I is represented by the dashed curve, and evidence $E \propto \exp[-(\chi^2/2 + I)]$ is represented on a log scale by the dotted curve. The maximum evidence (minimum negative log evidence -2LE) indicates the preferred FS model with $K = 4$. The fourth panel compares several FS models (solid curve) with the basic model (solid square) and basic model plus additional cosine terms (other symbols). Given the logarithmic scale the basic model is preferred over any FS model by at least 400-fold, and additional cosine terms are rejected as well.

Fig. 6.7-2 shows the same exercise applied to peripheral Au-Au collisions, essentially representing p-p (N-N) collisions, where we encounter a major challenge for BI analysis from two primary sources: (a) The signal amplitude is much smaller relative to statistical noise (15:1) compared to more central collisions (200:1), and (b) the SS peak is substantially broader on azimuth. The first panel shows the basic model fitted to data. The second panel shows the corresponding power spectrum. The SS-Gaussian transform is narrower and with smaller amplitude relative to the white-noise component such that only two signal degrees of freedom survive (compared to four for central collisions). We then expect a FS model with $K = 2$ to prevail as in the third panel. But in the fourth panel we find that the evidence for the $K = 3$ basic model is still substantially larger than for the $K = 2$ FS, a surprising result.

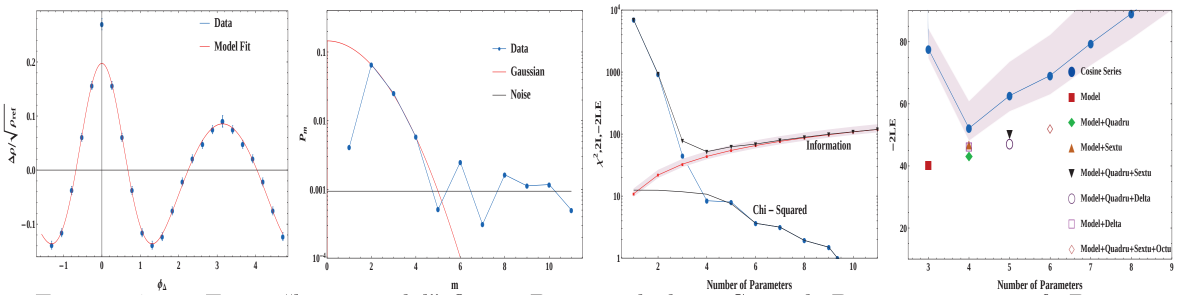

Figure 6.7-1. First: "basic model" fit to 1D azimuth data. Second: Power spectrum of 1D azimuth data. Third: BI parameters for FS models vs parameter number K. Fourth: BI evidence E for various models.

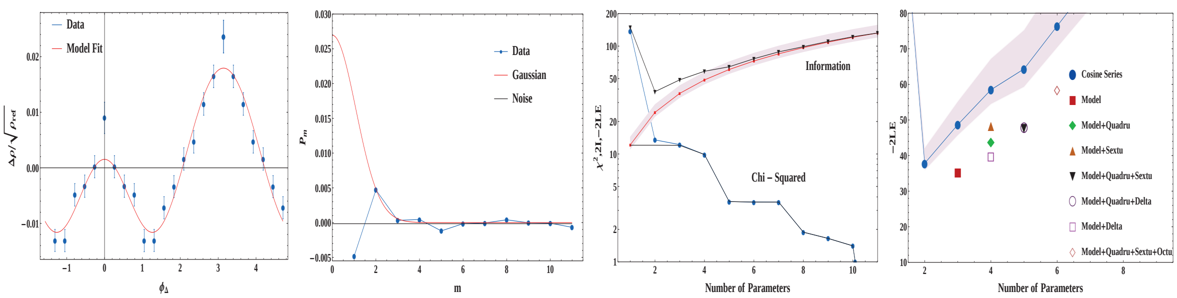

Figure 6.7-2. Same as the previous figure, but for peripheral Au-Au collisions.

Preference for the two-peak basic model despite 1D azimuth data with low S/N ratio is a significant achievement for BI analysis. The preference is buttressed by analysis of 2D data histograms where a jet-related SS 2D peak is *required* for all centralities, and a 1D FS-only model would fail dramatically for any 2D data. That is not apparent from conventional model fits to 1D projections alone, but the BI method nevertheless prefers the correct data model.

6.8 Geometric interpretation of Bayesian inference

M. B. De Kock*, H. C. Eggers*, and T. A. Trainor

Strong preference for the $K = 3$ basic model over a $K = 2$ Fourier series by BI methods in peripheral collisions (previous article) is surprising given Occam's principle that for similar fitted χ^2 values the simpler model (smaller K) should be preferred. Responding to that question leads to a better understanding of the BI method and what aspects of data models are most important. Fig. 6.8-1 (first) is a schematic representation of the joint parameter-data space $w \times D$ with vector components w_k and D_n. The data model $D(w)$ (diagonal line) maps points in parameter space w to points in data space D. A specific data set D^* with data errors σ_n is fitted with model $D(w)$ based on likelihood function $L(D^*|wH)$ resulting in optimal parameters $\tilde{w}_k$ and errors σ_k. As indicated by the bold vertical arrow the likelihood function with specific data errors effectively probes the local algebraic structure of $D(w)$ near measured data D^* by relating data errors σ_n to parameter errors σ_k. The geometric relation

*Stellenbosch University and National Institute for Theoretical Physics, Stellenbosch, South Africa.

between data and parameters is then characterized by the angles θ_{kn} defined by

$$\tan(\theta_{kn}) \quad \equiv \quad \frac{\sigma_n}{\sigma_k} \approx \frac{\partial D_n}{\partial w_k} \in J_{D(w)}. \tag{1}$$

The $\tan(\theta_{kn})$ are approximately elements of the model-function Jacobian $J_{D(w)}$ relating data and parameter spaces. The same local Jacobian elements may determine the relation between global probability density functions (PDFs) on w and D by extrapolation.

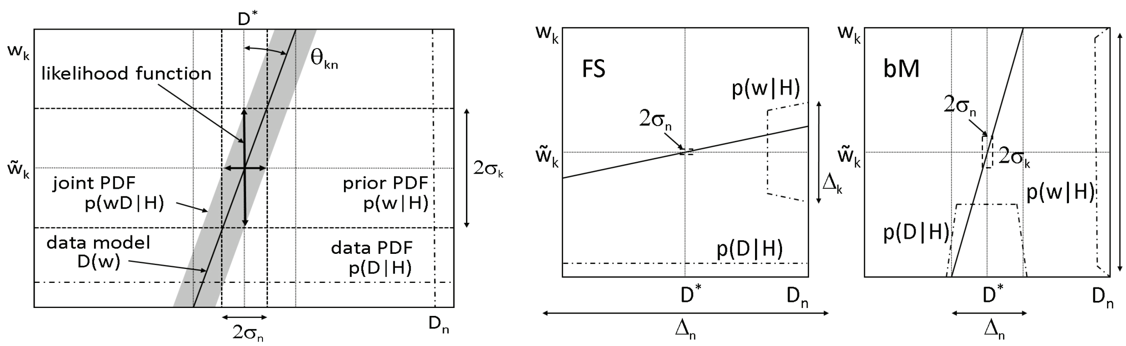

Figure 6.8-1. First: Schematic of model-data space for an arbitrary model function. Second, third: Model-data spaces for Fourier-series (FS) models and for the basic model.

Fig. 6.8-1 (second) shows the observed large $\sigma_n/\sigma_k \sim \theta_{kn}$ angles for FS models. In consequence a small prior interval Δ_k in the parameter space may be mapped to a large interval Δ_n in the data space, the ratio being determined by the model-function Jacobian. Fig. 6.8-1 (third) shows the results for the basic model. The typical θ_{kn} are much smaller than for FS models, leading to much smaller predicted data intervals Δ_n. Since it is approximately true that evidence $E \propto 1/\prod_n \Delta_n$ the inferred Jacobian structure of competing models implies that the basic model predicts a much smaller volume in data space D than FS models and hence a much larger evidence. If specific data D^* are inconsistent with the basic model it is falsified, but if they are consistent with the basic model it is most plausible. In contrast FS models cannot be falsified, *are not predictive*, and are therefore rejected by BI analysis.

7 Other research

7.1 Final report on the nonlocal quantum communication test

J. G. Cramer

Since 2007, we have conducted an ongoing experimental and theoretical investigation into the possibility of observer-to-observer communication using quantum nonlocality. The scheme investigated involves selecting particle-like or wave-like behavior of one member of an entangled photon pair in order to switch off and on, as a signal, an interference pattern generated by the other photon member of the entangled pair. The yearly progress of this work has been described in CENPA Annual Reports for the past eight years[1,2,3,4,5,6,7,8]. We have tested a number of experimental configurations with three pump lasers, three nonlinear crystals, and two single-photon detectors, with the general result that the measurements were limited by detector noise and the low intensity of entangled photon pairs from the source, and no switchable interference pattern was observed in non-coincident counting.

In the course of this work, we have gained an understanding of the "show stopper" within the quantum formalism that prevents such nonlocal signaling between observers. It is the intrinsic complementarity between one- and two-photon interference,[9] an effect that "erases" potential signals by superimposing two interference patterns that complement each other, resulting in no perceptible interference pattern. Operations on one photon can dramatically modify the interference pattern generated by the other photon, but always so that this erasure occurs.

The underlying cause of this suppression of one-particle interference is that optics geometry always produces a 180° switch in the relative phase between the two waves arriving at the detectors, which reverses the interference pattern. In optics, a 90° deflection causes a phase shift of $\pi/2$ in the reflected beam, a 180° deflection causes a phase shift of π, etc. When the opposed interference patterns are added, the result is always no pattern at all. This correlation of deflection angle with phase shift is an inescapable feature of quantum optics, and it provides the mechanism that "builds in" the observed interference complementarity. In this way, Nature is protected from the possibility of retrocausal signaling and its consequences and paradoxes.

These results have been described in a paper submitted for publication to *Foundations of Physics*, and it is presently under review. The paper has also been posted in the arXiv[10]. We consider this project to be completed and plan no further work in this area unless a new idea emerges.

---

[1] CENPA Annual Report, University of Washington (2007) p. 52.
[2] CENPA Annual Report, University of Washington (2008) p. 42.
[3] CENPA Annual Report, University of Washington (2009) p. 41.
[4] CENPA Annual Report, University of Washington (2010) p. 93.
[5] CENPA Annual Report, University of Washington (2011) p. 94.
[6] CENPA Annual Report, University of Washington (2012) p. 89.
[7] CENPA Annual Report, University of Washington (2013) p. 89.
[8] CENPA Annual Report, University of Washington (2014) p. 114.
[9] G. Jaeger, M. A. Horne, and A. Shimony, Phys. Rev. A **48**, 1023 (1993).
[10] J.Ġ. Cramer and N. Herbert, arXiv:1409.5098.

8 Education

8.1 Use of CENPA facilities in education and course work at UW

G. C. Harper* and E. B. Smith

CENPA has always maintained a prominent role in broad-scope, practical, hands-on training for both undergraduate and graduate students at the University of Washington. One of the most significant and unique advantages that our students enjoy is direct participation in the ongoing local research at CENPA and in the engineering contributions to our off-site collaborations.

We have been increasing our presence in undergraduate and graduate education and since spring 2011 we have provided an accelerator-based laboratory course in nuclear physics. This began as an undergraduate special-topics course in physics, course number 499, and has evolved into Physics 575, Nuclear Physics: Sources, Detectors, and Safety (Sec. 8.3).

We continue to provide extensive hands-on training for both undergraduate and graduate students. Our electronics shop is available for use by the students (Sec. 9.4) where they can learn electronic design and assembly. In the student shop (Sec. 9.5) all users are trained in machine-tool operation and safety. Finally, CENPA has a long history of teaching students accelerator and ion-source operation (Sec. 8.2).

8.2 Student training

G. C. Harper*, D. R. Hyde, D. A. Peterson, E. B. Smith, and D. I. Will

Students at CENPA receive training in a variety of technical laboratory skills that include accelerator operation, machining, and electronics. Seven students received accelerator operation training (a.k.a. "crew training") in which the students are taught to operate the ion sources and the tandem Van de Graaff accelerator. These students practice generating an ion beam, charging the tandem, and tuning the beam through the accelerator. Frequently, these individuals also gain experience with vacuum systems and cryogenics as dictated by the needs of their experiment.

CENPA student-shop training is received by incoming staff, RAs, REU students, and undergraduate students and on a continuing basis. These individuals are instructed on how to safely operate a variety of machines including lathes, milling machines, drill presses, saws, grinders, metal shears and breaker, hand tools, and power tools. Some are even trained to use an oxygen/acetylene cutting torch. Additionally, training is given on the student-shop NC 2-Axis Trak milling machine and laser cutter in order to make complicated parts for research projects.

*Retired August, 2014.

In the electronics shop, instruction is provided in soldering, wiring, and the use of basic electrical and electronic components. Training in the use of a new UV ProtoLaser is given to individuals wanting to fabricate prototype circuit boards for research projects.

8.3 Accelerator-based lab class in nuclear physics

A. García, G. C. Harper*, E. B. Smith, and D. I. Will

We have developed a graduate-level lecture and laboratory class for the purpose of teaching aspects of nuclear theory and techniques for nuclear physics experiments, including student operation of the tandem accelerator system to achieve beam on an experimental target[1].

The class met twice a week during the Spring 2014 quarter, once for a 1-1/2 hour lecture and again in groups for a 1-1/2 hour lab session. The list of subjects we covered were:

1. Atomic nucleus. Basics of nuclear physics, nuclear energy, orders of magnitude.
2. Attenuation of photon radiation. Solid-state detectors (Ge and Si).
3. Ranges of ions and electrons. The weak interaction. Radioactivity and radiation damage and health risks (α, β, γ, and neutron activity).
4. Deciphering a mystery γ spectrum. Gauging the level of radioactivity and assessing health risks.
5. Tandem-accelerator function and ion optics. Tuning beam in CENPA accelerator.
6. Rutherford back-scattering (RBS). Deciphering a mystery spectrum and the contents of a mystery foil.
7. Fission and fusion. The functioning of reactors.
8. Nuclear astrophysics: nucleosynthesis in stars.
9. Sources of positrons for positron emission tomography.

Nine students attended the Spring quarter 2014 sessions. Students engaged enthusiastically in discussions during lectures and in laboratory sessions.

---

*Retired August, 2014.

[1] Phys 575, Nuclear Physics: Sources, Detectors, and Safety, http://faculty.washington.edu/agarcia3/phys575.

9 Facilities

9.1 Facilities overview

G. C. Harper*, E. B. Smith, and D. I. Will

CENPA constantly updates and improves its facilities and provides the best possible resources and research environment for its users as new experiments emerge and as the demands of research change with time. In addition we maintain high-quality shop services that are available to the faculty, staff, and students.

The computational facilities at CENPA remain at the front edge of technology. As always, personal desktop and portable computers are maintained and the technology kept current. The NPL Data Center (NPLDC), which previously contained a single high-performance cluster, ATHENA, now provides the infrastructure to multiple clusters and department appliances (Sec. 9.3).

The laboratory facilities that surround, support, and include the FN tandem Van de Graaff accelerator are constantly evolving, and provide hands-on training for students in operation of the accelerator and ion sources (Sec. 9.2). A graduate physics course using the accelerator to perform nuclear-physics experiments has been developed (Sec. 8.3). Additionally, we have begun an upgrade project to replace the existing control hardware and software used by the accelerator system.

The CENPA electronics shop provides modern surface-mount technology and miniature cable-manufacturing equipment on site and in appropriately clean areas. The shop continues to do custom design work for specialty preamplifiers as well as dedicated multichannel data-acquisition (DAQ) systems. The shop also interacts with the on-campus Washington Technology Center, taking advantage of much of the capital-intensive, high-tech equipment there that is more effectively used as a cost-shared facility. The electronics-shop staff also provides training for students and other staff members (Sec. 9.4).

The CENPA instrument shop (main instrument shop) is manned by three highly skilled instrument makers with vast knowledge of metallurgy, welding, and fabrication (Sec. 9.5). This shop has CNC machines, mills, lathes, and large-capacity machines. The instrument shop can provide engineering for all research projects. The CENPA student shop is headed by an instrument maker who provides safety training and instruction to students, staff, and faculty. This shop includes mills, lathes, drill presses, a laser cutter, and a 3D printer.

The ADMX experiment is now fully installed, operational and taking data at the east end of our accelerator tunnel. Their completed pump shed houses two Bauer helium-recovery compressors, a large Edwards roughing pump, and a large Welch pump for the 1-K helium pot. The ADMX group is running a new Linde 1410 helium liquefier successfully at weekly intervals. Initial data suggest 96% of boil-off is reliquefied with the automated purge cycle of the purifier stage being the major helium loss. The liquefier has reduced helium purchases

*Retired August, 2014.

for this experiment from an estimated $500,000 to about $20,000 per year.

The MAJORANA and muon groups are now using their new laboratory space in rooms 108 and 110, respectively, for detector testing and development. (Sec. 9.6).

9.2 Van de Graaff accelerator and ion-source operations and development

A. T. Eberhardt*, B. E. Hamre†, G. C. Harper‡, G. H. Leum, S. D. MacDonald, J. R. Pedersen§, D. A. Peterson, S. S. Sexton, E. B. Smith, T. D. Van Wechel, and D. I. Will

There were four tandem entries required during this annual report period. An entry to replace a broken HE charging chain was performed on June 19, 2014. This was the first pelletron charging chain to break since the pelletron chains were installed in December 1993 (32,730 hours of operation). Two terminal-voltage charging pickup wheels were replaced (HE upper & LE lower) due to excessive drag, and all chain idlers were cleaned on both the LE and HE sides.

On July 11, 2014, an entry due to poor beamline vacuum resulted in the machining modification of another HV feedthrough position ("T" top) of the terminal steerer flange. Replacement of the charging cable (RG-8 core) to the lower HE charging shoe was performed, due to visible breakdown areas. After a short period of operation, the tandem beamline vacuum was poor and the entry on July 26, 2014, determined a HV feedthrough position ("L" left) on the terminal steerer flange, which had been remachined and replaced in April 2013, was leaking. The terminal steerer HV feedthrough flange was removed and all remaining positions ("R", "B", "+", "-") were machined to accept the newly (as of April 2013) CENPA designed and fabricated HV feedthrough with a threaded base and o-ring seal. The "+" and "-" positions were fitted with simple o-ring seal plugs. Although the installed flange and feedthroughs passed a leak check, the tandem beamline vacuum began to indicate a leak when the tank reached 80 psig during the fill.

A final entry on August 1, 2014, could not locate the source of the vacuum leak anywhere along the columns or terminal in the tandem tank. Therefore, all o-rings at every port of the terminal stripper box were replaced, and the terminal steerer HV feedthrough flange was replaced with a older flange having only the four feedthroughs needed for non-TIS operation ("T", "B", "L", "R") and utilizing modified spark plugs heavily sprayed with leak sealant (xylene). The charging cable (RG-8 core) from LE bulkhead to resistor for the upper charging shoe was replaced, because of visible breakdown areas.

During the 12 months from April 1, 2014, to March 31, 2015, the tandem pellet chains operated 594 hours, the sputter-ion source (SpIS) operated 0 hours, and the direct-extraction

*Arrived May, 2014.
†Arrived June, 2014.
‡Retired August, 2014.
§Departed October, 2014.

ACTIVITY SCHEDULED	DAYS SCHEDULED	PERCENT of TIME
Nuclear-physics research, accelerator	50	14
Development, maintenance, or crew training	23	6
Grand total	73	20

Table 9.2-1. Tandem accelerator operations April 1, 2014, to March 31, 2015.

ion source (DEIS) operated 629 hours. Additional statistics for accelerator operations are given in Table 9.2-1.

Ion beams produced using the DEIS this year included 15.0–17.8-MeV ^{2}H for the ^{6}He experiment, 17.5-MeV ^{1}H for the TRIMS experiment (^{83m}Kr generator), and 2.0-MeV ^{1}H for the Physics 575 class.

9.3 Laboratory computer systems

G. T. Holman

CENPA is a mixed shop of Windows 7, XP, Mac OS X and various Linux distributions. Windows 7 is installed on new systems but we are still running a few Windows XP systems for data acquisition. In previous years the IT focus was directed toward server consolidation, network security, process documentation and removal of redundant processes. We continue to utilize Xen virtualization to drive most web pages, Elogs, wiki, calendar, tracking, and document servers. The CENPA website and research group web pages are run on a virtual Debian server and utilize the Drupal web framework. The NPL mail server still provides NPL presence but all email is relayed to UW email hardware. This year we synchronized users on multiple Linux and Windows systems to UW active directory via a delegated organizational unit (OU), which removes the need to run a dedicated domain or LDAP server.

Two Dell 510 20-TB servers (Lisa and Marie) continue to offer user storage, print server capability, and improved backup policy. Linux, Windows and Mac workstations are backed up to the Lisa 20-TB raid farm from which they are written to LTO tape by the Physics Computer Center on a three-month backup retention plan. Lisa runs the Crash Plan Pro backup application which supports all operating systems and provides differential and encrypted backups. Whereas workstations rely on Crash Plan Pro for backups, all servers utilize rsync. Marie provides 20 TB for research, user, and shared group data.

The NPL Data Center (NPLDC) provides critical infrastructure supporting high-performance scientific-computing applications that cannot be efficiently executed on typical commodity server infrastructures (e.g., the Amazon EC2 Cloud). In previous years the space housed a single cluster that was treated as one computational resource, also known as Athena. Today, to meet the wide and highly specialized array of research requirements, the cluster has been separated into two specific cluster instances. The first cluster instance leverages Infiniband interconnects (classified as HPC clusters) and runs the latest open-source Rocks software[1], runs the cvmfs (Cern-VM file system) client, and Frontier local squid cache server. The second cluster that primarily runs single-threaded applications (non-HPC clusters) uses Rocks version 5.4, and most notably runs COMSOL, root[2], and Geant. Both cluster instances use Torque/Maui via dedicated front ends.

Approximately one third of the rack space is dedicated to non-cluster hardware: scratch storage, SQL, elogs, web applications, CAD workstations, and backup storage. These servers constitute over 200 TB of raw disk space.

Our computing and analysis facility consists of:

- The NPL data center as a shared resource with Physics, the Institute for Nuclear Theory (INT), and the Astronomy department.
- A mix of Linux servers: Debian, Redhat, and Ubuntu distributions.
- One VMS/VAXstation for legacy computing.
- Macintosh systems for the SNO+, KATRIN, MAJORANA, and emiT groups.
- A VAXstation for the linac and vacuum systems control and display system.
- Various Windows XP desktop JAM systems (Java-based software for acquisition and analysis), plus two laptops for transport to other installations.
- A Shorewall Linux-based logical firewall to protect the bulk of CENPA's PCs and servers.
- We provide additional legacy co-location services for the INT and the Physics Nuclear Theory group in the form of one VMS Alphastation 500, which is not directly used by lab personnel.

9.4 Electronic equipment

D. A. Peterson and T. D. Van Wechel

The electronics shop is responsible for the design and construction of new laboratory electronic equipment as well as the maintenance and repair of existing CENPA electronics. Projects undertaken by the electronics shop in the past year include the following:

1. Development and testing of the low-noise forward-biased reset preamplifier continued. In March it was tested, connected to a Mini-PPC Ge detector at Berkeley.
2. Designed and built a cable tester for the MAJORANA Demonstrator.
3. Continued clean-room soldering of the new MAJORANA Vespel connectors.
4. Designed and built a 10-Watt RF amplifier for the $g-2$ NMR system.
5. Designed and built a prototype 24 channel NMR probe multiplexer for $g-2$.
6. Designed and built SiPM readout board for the $g-2$ PbF_2 calorimeter.

[1]http://www.rocksclusters.org/
[2]http://root.cern.ch/

7. Designed and built a prototype SiPM readout board with programmable gain for the $g-2$ In-Beam monitoring system.
8. Designed and built a prototype 2-channel SiPM readout board and an FPGA-based controller board for the KATRIN veto upgrade.

9.5 CENPA instrument shops

T. H. Burritt, J. H. Elms, D. R. Hyde, and H. Simons

The CENPA instrument shop has given support to CENPA and several UW research groups. Projects completed this year include:

1. Designed and fabricated veto shield for KATRIN including tooling for polishing the fiber optics.
2. Made components to polish optical fibers.
3. Built mock up of existing KATRIN magnet and shielding components.
4. Started design on a new pre-spectrometer valve for KATRIN time-of-flight mode.
5. Modified, fabricated, and in-place soldered ADMX parts, gas lines, and equipment.
6. Prototyped the three new $g-2$ detectors.
7. Spun mu metal and machined components for the Gravity group.
8. Modified Van de Graaff accelerator parts.

The student shop produced several small projects in addition to providing machine-tool training and safety training for the faculty, staff, and students.

1. Manufactured adapter plate for the ^{6}He photo-multiplier tube assembly.
2. Manufactured a Cu source holder (Li Ion) for the ^{6}He experiment.
3. Made protective-copper screens for the 24" vacuum chamber.
4. Modified PVC blocks for the calorimeter used for the $g-2$ project.
5. Trained student to make heat reservoirs for the $g-2$ pulsed NMR probes.

9.6 Building maintenance and upgrades

D. I. Will

This year included two major capital projects funded by the University of Washington: the NPL Roof Project and the NPL 2400 VAC Transformer Replacement Project. The re-roofing of above-ground areas of the Van de Graaff building, planned during the latter half of 2013 and first half of 2014, began construction in June 2014 and was scheduled for completion in September or October 2014. Portions of this project have stretched well into 2015 and the final closeout checklist (already attempted several times) will likely occur in May 2015.

The Van de Graaff roof is complete. The two small pieces of the Cyclotron building roof included in this project are also complete. These appear leak-tight. Unfortunately, the building envelope architect and the general contractor made a less-than-successful attempt to stabilize the badly deteriorated bituminous waterproofing of the old shielding pond over the Cyclotron circleroom. The plan was to drain the pond, abate loose portions of the old lining and install a 40-mil pond liner. Fastening the pond liner securely over the top of the circleroom parapet wall required removing an old, crude, existing retaining wall and replacing it with a double row of 2'x2'x4' concrete ecology blocks placed back about 18 from the existing parapet which encircles the pond. The new retaining wall stretches for about 120° along the west edge of the pond. The architect called for a French drain system outside the foot of the new retaining wall. From the westernmost point, separate French drains slope downward in 60° arcs both north and south, each for about 60° to separate drywells. The architect drew the drywells about six feet away from the circleroom wall, but the contractor mistakenly installed them adjacent to the wall. During a three-day period of intense rains this winter, the southern drywell caused extensive leakage through the nearly 70-year-old concrete wall. Leakage flows between 5 and 10 gallons per hour caused nearly $40,000 damage to electronics and other equipment, mostly repaired now. We did get the contractor to reroute the southern french drain into a section of 4" drain line leading downhill away from the pond atop the circleroom. We have had no more leakage during the times this drain was intact, but did see leakage during a rainy period when the drain line had been disconnected to install the parapet cap. We have requested, and been promised, that as part of a new, much smaller, remediation project, water from both French drains and from the 18 trough between parapet and retaining wall will be collected at both north and south ends and routed downhill to an asphalt walkway/gutter running along the west edge of exposed portions of the Cyclotron building, which will carry this water south to a large existing large storm drain catch basin.

Planning and exploration for the 2400 VAC transformer replacement project also started in 2013. When the Cyclotron building was constructed in about 1947, electrical power consumption was much lower and the University used 2400 VAC power mains to supply major campus buildings and even clusters of buildings. The University now uses 13.8-KV mains for distribution. The Cyclotron building and its associated shop had roughly 1,000 KVA of 240-VAC delta (stepped down from the 2400 VAC) for magnet and oscillator supplies as well as the shop's large lathes and mills. For lighting and building mechanical systems 150 KVA of 120/208VAC wye was also provided from the 2400 VAC mains. The impetus for this replacement included the age of the equipment, the desire to remove and abate the six oil-filled, PCB-era transformers (one for each leg of each voltage) and the dangers of the underground vault which contained partially exposed 2400 VAC wiring. The actual replacement began January of 2015 and is going smoothly. The final power outage to reconnect the Cyclotron building to permanent power is scheduled for Saturday, May 16th, 2015. We have worked with both the electrical engineering design firm and the electrical contractor selected for this project and fully expect this electrical upgrade to finish fully satisfactorily and on schedule.

Again this year, numerous, smaller, routine and non-routine work orders have been placed and the work completed by the University's maintenance shops.

10 CENPA Personnel

10.1 Faculty

Eric G. Adelberger[1]	Professor Emeritus
Hans Bichsel[1]	Affiliate Professor
John G. Cramer[1]	Professor Emeritus
Jason Detwiler	Assistant Professor
Peter J. Doe	Research Professor
Sanshiro Enomoto	Research Assistant Professor; CENPA Fellow
Svenja Fleischer[1]	Research Assistant Professor
Alejandro García	Professor
Fred Gray[2]	Visiting Associate Professor
Jens H. Gundlach[1]	Professor
Blayne R. Heckel[1]	Professor; Chair
David W. Hertzog	Professor
C. D. Hoyle[1,3]	Affiliate Associate Professor
Peter Kammel	Research Professor
Jarek Kaspar[4]	Acting Assistant Professor
Michael L. Miller[1,5]	Affiliate Research Assistant Professor
Diana Parno[6]	Acting Assistant Professor; Associate Director
R. G. Hamish Robertson	Professor; Director
Leslie J Rosenberg[1]	Professor
Gray Rybka	Research Assistant Professor
Derek W. Storm[1]	Research Professor Emeritus
Nikolai R. Tolich	Assistant Professor
Thomas A. Trainor[7,8]	Research Professor Emeritus
John F. Wilkerson[1,9]	Affiliate Professor

10.2 CENPA External Advisory Committee

Robert McKeown[10]	Jefferson Laboratory
Daniel McKinsey[10]	Yale University
Michael Ramsey-Musolf[10]	University of Massachusetts, Amherst

[1] Not supported by DOE CENPA grant.
[2] Departed May, 2014, Sabbatical visitor, Regis University, Denver, CO.
[3] Affiliated faculty, Humboldt State University, Arcata, CA.
[4] Not supported by DOE CENPA grant except April 1-15, 2014.
[5] Affiliated faculty.
[6] DOE supported through August, 2014.
[7] Retired December, 2014.
[8] DOE supported through November, 2014.
[9] Affiliated faculty, University of North Carolina, Chapel Hill, NC.
[10] CENPA External Advisory Committee formed January, 2014.

10.3 Postdoctoral Research Associates

L. Peter Alonzi[1]
Jason Crnkovic[2]
Clara Cuesta[3]
Martin Fertl
Michael Hotz[3,4]
Kim Siang Khaw[5]
Jared Kofron[6]
Andreas Kraft[3,7]
Arnaud Leredde[3,8]
Dmitry Lyapustin[3,9]
Ana Malagon[10]
Matthew Sternberg
Joulien Tatar[3,11]
Krishna Venkateswara[3]
Andrew Wagner[3,4]
Frederik Wauters

10.4 Predoctoral Research Associates

Yelena Bagdasarova[3,8]
Laura Bodine
Christian Boutan[3]
Micah Buuck
Aaron Fienberg
Nathan Froemming
Brent Graner
Julieta Gruszko[3]
Ian Guinn
Charles Hagedorn[3]
Ran Hong
Luke Kippenbrock
Jared Kofron[12]
John G. Lee[3]
Jonathan Leon[3]
Dmitry Lyapustin[3,12]
Timothy Major
Eric Martin
Michael Murray
Rachel Osofsky[13]
Rachel Ryan
James Sloan[3]
Erik Shaw[3,13]
Matthias Smith
William Terrano[3]
Matthew Turner[3]
Todd Wagner[14]
David Zumwalt[3]

---

[1]Departed September, 2014. Currently at University of Virginia.
[2]Departed April, 2014. Currently a research associate at Brookhaven National Lab.
[3]Not supported by DOE CENPA grant.
[4]Departed December, 2014.
[5]Arrived March, 2015.
[6]Commenced Visiting Scientist position March, 2015.
[7]Departed September, 2014.
[8]Supported by Argonne National Laboratory.
[9]Commenced postdoctoral position March, 2015.
[10]Arrived September, 2014.
[11]Arrived April, 2014. Departed January, 2015. Currently at UC Berkeley.
[12]Graduated March, 2015.
[13]Arrived June, 2014.
[14]Graduated December, 2014.

10.5 NSF Research Experience for Undergraduates participants

Aryeh Brill	Yale University	Gray Rybka, Leslie Rosenberg, Advisors
Audrey K. Kvam	University of Puget Sound	Alejandro García, Advisor

10.6 University of Washington graduates taking research credit

Ting Lin[1]	Diana Parno, Advisor
Rachel Morris	Alejandro García, Advisor
Matthew Noakes	Nikolai Tolich, Advisor
Diana Thompson	Alejandro García, Advisor

10.7 University of Washington undergraduates taking research credit

Justin Jachette Devault	Alejandro García, Advisor
Cole Helling	Alejandro García, Advisor
Andrew Hillman	Alejandro García, Advisor
Dustin Kasparek	Gray Rybka, Advisor
Aobo Li	Jason Detwiler, Advisor
Ronaldo Ortez	Alejandro García, Advisor
Wade Shaffer	Alejandro García, David W. Hertzog, Advisors
David Smith	Martin Fertl, Advisor
Jordan Stiebnitz	Alejandro García, Advisor
Alex Thompson	Jason Detwiler, Advisor
Khang Ton	Jason Detwiler, Advisor
Maarten Van Genabeek	Alejandro García, Advisor
Alex Zderic	Jason Detwiler, Advisor

10.8 Visiting students taking research credit

Julian Becker	Peter J. Doe, Advisor

[1] Arrived January, 2015.

10.9 Professional staff

John F. Amsbaugh	Research Engineer	Engineering, vacuum, cryogenics design
Tom H. Burritt	Shop supervisor	Precision design, machining
Gregory C. Harper[1]	Associate Director	Accelerator, ion sources
Gary T. Holman	Systems Manager	Computer systems
Hannah LeTourneau	Research Engineer	Helium liquefier
Clifford Plesha	Research Engineer	Helium liquefier
Duncan J. Prindle, Ph.D.	Research Scientist	Heavy ion, muon research
Eric B. Smith	Research Engineer	Accelerator, ion sources
H. Erik Swanson, Ph.D.	Research Physicist	Precision experimental equipment
Timothy D. Van Wechel	Research Engineer	Analog and digital electronics design
Douglas I. Will	Senior Engineer	Cryogenics, ion sources, buildings

10.10 Technical staff

James H. Elms	Instrument Maker
David R. Hyde	Instrument Maker
David A. Peterson	Electronics Technician

10.11 Administrative staff

Victoria A. Clarkson	Administrator
Robert S. Shupe[1]	Fiscal Specialist 2
Nomie Torres[2]	Fiscal Specialist 2

10.12 Part-time staff and student helpers

Andrew Eberhardt[3]
Farah Fahim[4]
Brett Hamre[5]
Rigel Ifland[6]
Christopher Jantzi[7]
Grant Leum
Sean MacDonald
Elizabeth McBride
Ronaldo Ortez
Joben Pedersen[8]
Robert Percival[9]
Gary Plunkett[10]
Samuel Sexton
Wade Shaffer[5]
Hendrik Simons
Joseph Toles[11]
Megan Wachtendonk[2]
Kazimir Wall
Natasha Woods[11]

[1] Retired August, 2014.
[2] Arrived December, 2014.
[3] Arrived May, 2014.
[4] Arrived September, 2014. Departed November, 2015.
[5] Arrived June, 2014.
[6] Arrived October, 2014. Departed March, 2015.
[7] Arrived May, 2014. Departed June, 2015.
[8] Departed October, 2014.
[9] Arrived January, 2014. Departed May, 2014.
[10] Arrived June, 2014. Departed July, 2014.
[11] Departed June, 2014.

11 Publications

Publications and presentations with a date of 2014 or 2015 are included below. Some entries from early 2014 may therefore also appear in the 2014 Annual Report.

11.1 Published papers

1. "A Precision Measurement of the Neutron Twist-3 Matrix Element d_2^n: Probing Color Forces," M. Posik, D. Flay, D. S. Parno*, K. Allada, W. Armstrong, T. Averett, F. Benmokhtar, W. Bertozzi, A. Camsonne, M. Canan, G. D. Cates, C. Chen, J.-P. Chen, S. Choi, E. Chudakov, F. Cusanno, M. M. Dalton, W. Deconinck, C. W. de Jager, X. Deng, A. Deur, C. Dutta, L. El Fassi, G. B. Franklin, M. Friend, H. Gao, F. Garibaldi, S. Gilad, R. Gilman, O. Glamazdin, S. Golge, J. Gomez, L. Guo, O. Hansen, D. W. Higinbotham, T. Holmstrom, J. Huang, C. Hyde, H. F. Ibrahim, X. Jiang, G. Jin, J. Katich, A. Kelleher, A. Kolarkar, W. Korsch, G. Kumbartzki, J. J. LeRose, R. Lindgren, N. Liyanage, E. Long, A. Lukhanin, V. Mamyan, D. McNulty, Z.-E. Meziani, R. Michaels, M. Mihovilovič, B. Moffit, N. Muangma, S. Nanda, A. Narayan, V. Nelyubin, B. Norum, Nuruzzaman, Y. Oh, J. C. Peng, X. Qian, Y. Qiang, A. Rakhman, S. Riordan, A. Saha, B. Sawatzky, M. H. Shabestari, A. Shahinyan, S. Širca, P. Solvignon, R. Subedi, V. Sulkosky, W. A. Tobias, W. Troth, D. Wang, Y. Wang, B. Wojtsekhowski, X. Yan, H. Yao, Y. Ye, Z. Ye, L. Yuan, X. Zhan, Y. Zhang, Y.-W. Zhang, B. Zhao, and X. Zheng, Phys. Rev. Lett. **113**, 022002 (2014); arXiv:1404.4003.

2. "Precision Measurements of A_1^n in the Deep Inelastic Regime," D. S. Parno*, D. Flay, M. Posik, K. Allada, W. Armstrong, T. Averett, F. Benmokhtar, W. Bertozzi, A. Camsonne, M. Canan, G. D. Cates, C. Chen, J.-P. Chen, S. Choi, E. Chudakov, F. Cusanno, M. M. Dalton, W. Deconinck, C. W. de Jager, X. Deng, A. Deur, C. Dutta, L. El Fassi, G. B. Franklin, M. Friend, H. Gao, F. Garibaldi, S. Gilad, R. Gilman, O. Glamazdin, S. Golge, J. Gomez, L. Guo, O. Hansen, D. W. Higinbotham, T. Holmstrom, J. Huang, C. Hyde, H. F. Ibrahim, X. Jiang, G. Jin, J. Katich, A. Kelleher, A. Kolarkar, W. Korsch, G. Kumbartzki, J. J. LeRose, R. Lindgren, N. Liyanage, E. Long, A. Lukhanin, V. Mamyan, D. McNulty, Z.-E. Meziani, R. Michaels, M. Mihovilovič, B. Moffit, N. Muangma, S. Nanda, A. Narayan, V. Nelyubin, B. Norum, Nuruzzaman, Y. Oh, J. C. Peng, X. Qian, Y. Qiang, A. Rakhman, S. Riordan, A. Saha, B. Sawatzky, M. H. Shabestari, A. Shahinyan, S. Širca, P. Solvignon, R. Subedi, V. Sulkosky, W. A. Tobias, W. Troth, D. Wang, Y. Wang, B. Wojtsekhowski, X. Yan, H. Yao, Y. Ye, Z. Ye, L. Yuan, X. Zhan, Y. Zhang, Y.-W. Zhang, B. Zhao, and X. Zheng; Phys. Lett. B **744**, 309 (2015); arXiv:1406.1207.

3. "A critical review of RHIC experimental results," T. A. Trainor*, Int. J. Mod. Phys. E **23**, 1430011 (2014); arXiv:1303.4774.†

An * denotes a CENPA author who is the lead author of or major contributor to a publication.
A † denotes a publication describing work fully or partially supported by the DOE grant.

4. "A Search for Astrophysical Burst Signals at the Sudbury Neutrino Observatory," B. Aharmim, S. N. Ahmed, A. E. Anthony, N. Barros, E. W. Beier, A. Bellerive, B. Beltran, M. Bergevin, S. D. Biller, K. Boudjemline, M. G. Boulay, T. H. Burritt, B. Cai, Y. D. Chan, D. Chauhan, M. Chen, B. T. Cleveland, G. A. Cox, X. Dai, H. Deng, J. A. Detwiler, M. Diamond, M. DiMarco, P. J. Doe, G. Doucas, P.-L. Drouin, C. A. Duba, F. A. Duncan, M. Dunford, E. D. Earle, S. R. Elliott, H. C. Evans, G. T. Ewan, J. Farine, H. Fergani, F. Fleurot, R. J. Ford, J. A. Formaggio, N. Gagnon, J. TM. Goon, K. Graham, E. Guillian, S. Habib, R. L. Hahn, A. L. Hallin, E. D. Hallman, P. J. Harvey, R. Hazama, W. J. Heintzelman, J. Heise, R. L. Helmer, A. Hime, C. Howard, M. A. Howe, M. Huang, P. Jagam, B. Jamieson, N. A. Jelley, K. J. Keeter, J. R. Klein, L. L. Kormos, M. Kos, C. Kraus, C. B. Krauss, A. Krueger, T. Kutter, C. C. M. Kyba, R. Lange, J. Law, I. T. Lawson, K. T. Lesko, J. R. Leslie, I. Levine, J. C. Loach, R. MacLellan, S. Majerus, H. B. Mak, J. Maneira, R. Martin, N. McCauley, A. B. McDonald, S. McGee, M. L. Miller, B. Monreal, J. Monroe, B. Morissette, B. G. Nickel, A. J. Noble, H. M. O'Keeffe, N. S. Oblath, R. W. Ollerhead, G. D. Orebi Gann, S. M. Oser, R. A. Ott, S. J. M. Peeters, A. W. P. Poon, G. Prior, S. D. Reitzner, K. Rielage, B. C. Robertson, R. G. H. Robertson, M. H. Schwendener, J. A. Secrest, S. R. Seibert, O. Simard, D. Sinclair, P. Skensved, T. J. Sonley, L. C. Stonehill, G. Tesic, N. Tolich, T. Tsui, C. D. Tunnell, R. Van Berg, B. A. VanDevender, C. J. Virtue, B. L. Wall, D. Waller, H. Wan Chan Tseung, D. L. Wark, J. Wendland, N. West, J. F. Wilkerson, J. R. Wilson, J. M. Wouters, A. Wright, M. Yeh, F. Zhang, and K. Zuber (SNO Collaboration), Astropart. Phys. **55**, 1 (2014); arXiv:1309.0910.**†**

5. "Focal-plane detector system for the KATRIN experiment," J. F. Amsbaugh, J. Barrett, A. Beglarian, T. Bergmann, H. Bichsel, L. I. Bodine, J. Bonn, N. M. Boyd, T. H. Burritt, Z. Chaoui, S. Chilingaryan, T. J. Corona, P. J. Doe, J. A. Dunmore, S. Enomoto, J. Fischer, J. A. Formaggio, F. M. Fraenkle, D. Furse, H. Gemmeke, F. Glueck, F. Harms, G. C. Harper, J. Hartmann, M. A. Howe, A. Kaboth, J. Kelsey, M. Knauer, A. Kopmann, M. L. Leber, E. L. Martin, K. J. Middleman, A. W. Myers, N. S. Oblath, D. S. Parno*****, D. A. Peterson, L. Petzold, D. G. Phillips II, P. Renschler, R. G. H. Robertson, J. Schwarz, M. Steidl, D. Tcherniakhovski, T. Thuemmler, T. D. Van Wechel, B. A. VanDevender, S. Voecking, B. L. Wall, K. L. Wierman, J. F. Wilkerson, and S. Wuestling, Nucl. Inst. Meth. A **778**, 40 (2015); arXiv:1404.2925.**†**

6. "Examination of the calorimetric spectrum to determine the neutrino mass in low-energy electron capture decay," R. G. H. Robertson*****, Phys. Rev. C **91**, 035504 (2015); arXiv:1411.2906.**†**

7. "Copper coated carbon fiber reinforced plastics for high and ultra high vacuum applications," F. Burri, M. Fertl, P. Feusi, R. Henneck, K. Kirch, B. Lauss, P. Rüttimann, P. Schmidt-Wellenburg, A. Schnabel, J. Voigt, J. Zenner, and G. Zsigmond, Vacuum **101**, 212 (2014); arXiv:1308.2563.

An ***** denotes a CENPA author who is the lead author of or major contributor to a publication.
A **†** denotes a publication describing work fully or partially supported by the DOE grant.

8. "New source for ultracold neutrons at the Institut Laue-Langevin," F. M. Piegsa, M. Fertl, S. N. Ivanov, M. Kreuz, K. K. H. Leung, P. Schmidt-Wellenburg, T. Soldner, and O. Zimmer, Phys. Rev. C **90**, 015501 (2014); arXiv:1404.3527.

9. "Dynamic stabilization of the magnetic field surrounding the neutron electric dipole moment spectrometer at the Paul Scherrer Institute," S. Afach, G. Bison, K. Bodek, F. Burri, Z. Chowdhuri, M. Daum, M. Fertl, B. Franke, Z. Grujic, V. Hélaine, R. Henneck, M. Kasprzak, K. Kirch, H. C. Koch, A. Kozela, J. Krempel, B. Lauss, T. Lefort, Y. Lemière, M. Meier, O. Naviliat-Cuncic, F. M. Piegsa, G. Pignol, C. Plonka-Spehr, P. N. Prashanth, G. Quéméner, D. Rebreyend, S. Roccia, P. Schmidt-Wellenburg, A. Schnabel, N. Severijns, J. Voigt, A. Weis, G. Wyszynski, J. Zema, J. Zenner, and G. Zsigmond, J. Appl. Phys. **116**, 084510 (2014); arXiv:1408.6752.

10. "A measurement of the neutron to ^{199}Hg magnetic moment ratio," S. Afach, C. A. Baker, G. Ban, G. Bison, K. Bodek, M. Burghoff, Z. Chowdhuri, M. Daum, M. Fertl, B. Franke, P. Geltenbort, K. Green, M. G. D. van der Grinten, Z. Grujic, P. G. Harris, V. Hélaine, R. Henneck, M. Horras, P. Iaydjiev, S. N. Ivanov, M. Kasprzak, Y. Kermaïdic, K. Kirch, A. Knecht, H. C. Koch, J. Krempel, M. Kuźniak, B. Lauss, T. Lefort, Y. Lemiére, A. Mtchedlishvili, O. Naviliat-Cuncic, J. M. Pendlebury, M. Perkowski, E. Pierre , F. M. Piegsa, G. Pignol, P. N. Prashanth, G. Quéméner, D. Rebreyend, D. Ries, S. Roccia, P. Schmidt-Wellenburg, A. Schnabel, N. Severijns, D. Shiers, K. F. Smith, J. Voigt, A. Weis, G. Wyszynski, J. Zema, J. Zenner, and G. Zsigmond, Phys. Lett. B **739**, 128 (2014).

11. "Neutron production and thermal moderation at the PSI UCN source," H. Becker, G. Bison, B. Blau, Z. Chowdhuri, J. Eikenberg, M. Fertl, K. Kirch, B. Lauss, G. Perret, D. Reggiani, D. Ries, P. Schmidt-Wellenburg, V. Talanov, M. Wohlmuther, and G. Zsigmond, Nucl. Inst. Meth. A **777**, 20 (2014); arXiv:1408.3217.

12. "Challenging claims of 'elliptic flow' by comparing azimuth quadrupole and jet-related angular correlations from Au-Au collisions at $\sqrt{s_{NN}} = 62$ and 200 GeV," T. A. Trainor*, D. T. Kettler, D. J. Prindle, and R. L. Ray, J. Phys. G **42**, 025102 (2015); arXiv:1302.0300.†

13. "Ensemble mean p_t vs charged-hadron multiplicities in high energy nuclear collisions," T. A. Trainor*, Phys. Rev. C **90**, 024909 (2014); arXiv:1403.6494.†

14. "Universal parametrization of jet production based on parton and fragment rapidities," T. A. Trainor*, Phys. Rev. D **89**, 094011 (2014); arXiv:1403.3685.†

15. "Limits on tensor-type weak currents from nuclear and neutron β decays," F. Wauters*, A. García*, and R. Hong, Phys. Rev. C **89**, 025501 (2014); arXiv:1306.2608.†

An * denotes a CENPA author who is the lead author of or major contributor to a publication.
A † denotes a publication describing work fully or partially supported by the DOE grant.

16. "A high-pressure hydrogen time projection chamber for the MuCap experiment," J. Egger, D. Fahrni, M. Hildebrandt, A. Hofer, L. Meier, C. Petitjean, V. A. Andreev, T. I. Banks, S. M. Clayton, V. A. Ganzha, F. E. Gray, P. Kammel*****, B. Kiburg, P. A. Kravtsov, A. G. Krivshich, B. Lauss, E. M. Maev, O. E. Maev, G. Petrov, G. G. Semenchuk, A. A. Vasilyev, A. A. Vorobyov, M. E. Vznuzdaev, and P. Winter, Eur. Phys. J. A. **50**, 163 (2014); arXiv:1405.2853.**†**

17. "Design and operation of a cryogenic charge-integrating preamplifier for the MuSun experiment," R. A. Ryan*****, F. Wauters*****, F. E. Gray, P. Kammel*****, A. Nadtochy, D. Peterson, T. van Wechel, E. Gross, M. Gubanich,L. Kochenda, P. Kravtsov, D. Orozco, R. Osofsky, M. H. Murray, G. E. Petrov, J. D. Phillips, J. Stroud, V. Trofimov, A. Vasilyev, and M. Vznuzdaev, J. Instrum. **9**, P07029 (2014); arXiv:1404.3251.**†**

18. "Measurement of the beta-asymmetry parameter of Cu-67 in search for tensor-type currents in the weak interaction," G. Soti, F. Wauters*****, M. Breitenfeldt, P. Finlay, P. Herzog, A. Knecht, U. Köster, I. S. Kraev, T. Porobic, P. N. Prashanth, I. S. Towner, C. Tramm, D. Zákoucký, and N. Severijns, Phys. Rev. C **90**, 035502 (2014); arXiv:1409.1824.

19. "The Majorana Parts Tracking Database," N. Abgrall, E. Aguayo, F. T. Avignone III, A. S. Barabash, F. E. Bertrand, V. Brudanin, M. Busch, D. Byram, A. S. Caldwell, Y-D. Chan, C. D. Christofferson, D. C. Combs, C. Cuesta, J. A. Detwiler, P. J. Doe, Yu. Efremenko, V. Egorov, H. Ejiri, S. R. Elliott, J. Esterline, J. E. Fast, P. Finnerty, F. M. Fraenkle, A. Galindo-Uribarri, G. K. Giovanetti, J. Goett, M. P. Green, J. Gruszko, V. E. Guiseppe, K. Gusev, A. L. Hallin, R. Hazama, A. Hegai, R. Henning, E. W. Hoppe, S. Howard, M. A. Howe, K. J. Keeter, M. F. Kidd, O. Kochetov, S. I. Konovalov, R. T. Kouzes, B. D. LaFerriere, J. Leon, L. E. Leviner, J. C. Loach, J. MacMullin, R. D. Martin, S. J. Meijer, S. Mertens, M. L. Miller, L. Mizouni, M. Nomachi, J. L. Orrell, C. OShaughnessy, N. R. Overman, R. Petersburg, D. G. Phillips II, A. W. P. Poon, K. Pushkin, D. C. Radford, J. Rager, K. Rielage, R. G. H. Robertson, E. Romero-Romero, M. C. Ronquest, B. Shanks, T. Shima, M. Shirchenko, K. J. Snavely, N. Snyder, A. Soin, A. M. Suriano, D. Tedeschi, J. Thompson, V. Timkin, W. Tornow, J. E. Trimble, R. L. Varner, S. Vasilyev, K. Vetter, K. Vorren, B. R. White, J. F. Wilkerson, C. Wiseman, W. Xu, E. Yakushev, A. R. Young, C.-H. Yu, and V. Yumatov, I. Zhitnikov, Nucl. Inst. Meth. A **779**, 52 (2015); arXiv:1502.01748.**†**.

20. "Cosmogenic radionuclide production in NaI(Tl) crystals," J. Amaré, S. Cebrián, C. Cuesta, E. García, C. Ginestra, M. Martínez, M. A. Oliván, Y. Ortigoza, A. Ortiz de Solórzano, C. Pobes, J. Puimedón, M. L. Sarsa, J. A. Villar, and P. Villar, J. Cosmol. Astropart. Phys. **2015**, 46 (2015); arXiv:1411.0106.

21. "Questioning tests of hadron production models based on minimum-bias distributions on transverse energy," T. A. Trainor*****, Phys. Rev. C **91**, 044905 (2015).**†**

An ***** denotes a CENPA author who is the lead author of or major contributor to a publication.
A **†** denotes a publication describing work fully or partially supported by the DOE grant.

22. "Bulk NaI(Tl) scintillation low energy events selection with the ANAIS-0 module," C. Cuesta*, J. Amaré, S. Cebrián, E. García, C. Ginestra, M. Martínez, M. A. Oliván, Y. Ortigoza, A. Ortiz de Solórzano, C. Pobes, J. Puimedón, M. L. Sarsa, J. A. Villar, and P. Villar, Eur. Phys. J. C **74**, 3150 (2014); arXiv:1407.5125.

23. "Analysis of the ^{40}K contamination in NaI(Tl) crystals from different providers in the frame of the ANAIS project," C. Cuesta*, J. Amaré, S. Cebrián, E. García, C. Ginestra, M. Martínez, M. A. Oliván, Y. Ortigoza, A. Ortiz de Solórzano, C. Pobes, J. Puimedón, M. L. Sarsa, J. A. Villar, and P. Villar, Int. J. Mod. Phys. A **29**, 1443010 (2014); arXiv:1403.3580.

24. "Scintillating bolometers: a key for determining WIMP parameters," D. G. Cerdeño, C. Cuesta, M. Fornasa, E. García, C. Ginestra, C. Marcos, M. Martínez, Y. Ortigoza, M. Peiró, J. Puimedón, and M. L. Sarsa, Int. J. Mod. Phys. A **29**, 1443009 (2014); arXiv:1403.3539.

25. "EURECA Conceptual Design Report," G. Angloher, E. Armengaud, C. Augier, A. Benoit , T. Bergmann, J. Blümer, A. Broniatowski, V. Brudanin, P. Camus, M. Chapellier, N. Coron, G. A. Cox, C. Cuesta, F. A. Danevich, L. Dumoulin, K. Eitel, A. Erb, A. Ertl, F. von Feilitzsch, D. Filosofovh, E. García, J. Gascon, G. Gerbier, C. Ginestra, J. Gironnet, A. Giuliani, M. Gros, A. Gütlein, D. Hauff, S. Henry, G. Heuermann, J. Jochum, S. Jokisch, A. Juillard, C. Kister, M. Kleifges, H. Kluck, E. V. Korolkova, V. Y. Kozlov, H. Kraus, V. A. Kudryavtsev, J. C. Lanfranchi, P. Loaiza, J. Loebell, I. Machulin, S. Marnieros, M. Martínez, A. Menshikov, A. Münster, X. F. Navick, C. Nones, Y. Ortigoza, P. Pari, F. Petricca, W. Potzel, P. P. Povinect, F. Pröbst, J. Puimedón, F. Reindl, M. Robinson, T. Rolón, S. Roth, K. Rottler, S. Rozov, C. Sailer, A. Salinas, V. Sanglard, M. L. Sarsa, K. Schäffner, B. Schmidt, S. Scholl, S. Schönert, W. Seidel, B. Siebenborn, M.v. Sivers, C. Strandhagen, R. Strauß, A. Tanzke, V. I. Tretyak, M. Turad, A. Ulrich, I. Usherov, P. Veber, M. Velazquez, J. A. Villar, O. Viraphong, R. J. Walker, S. Wawoczny, M. Weber, M. Willers, M. Wüstrich, E. Yakushev, X. Zhang, and A. Zöller, Phys. of the Dark Universe **3**, 41 (2014).

26. "Study of scintillation in natural and synthetic quartz and methacrylate," J. Amaré, S. Borjabad, S. Cebrián, C. Cuesta, D. Fortuño, E. García, C. Ginestra, H. Gómez, D. C. Herrera, M. Martínez, M. A. Oliván, Y. Ortigoza, A. Ortiz de Solórzano, C. Pobes, J. Puimedón, M. L. Sarsa, J. A. Villar, and P. Villar, Opt. Mat. **36**, 1408 (2014); arXiv:1401.3118.

27. "Test of candidate light distributors for the muon $(g-2)$ laser calibration system," A. Anastasi, D. Babusci, F. Baffigi, G. Cantatore, D. Cauz, G. Corradi, S. Dabagov, G. Di Sciascio, R. Di Stefano, C. Ferrari, A. T. Fienberg, A. Fioretti, L. Fulgentini, C. Gabbanini, L. A. Gizzi, D. Hampai, D. W. Hertzog, M. Iacovacci, M. Karuza, J. Kaspar, P. Koester, L. Labate, S. Mastroianni, D. Moricciani, G. Pauletta, L. Santi, and G. Venanzoni, Nucl. Inst. Meth. A **788**, 43 (2015); arXiv:1504.00132.†

An * denotes a CENPA author who is the lead author of or major contributor to a publication.
A † denotes a publication describing work fully or partially supported by the DOE grant.

28. “A Compact Ultra-Clean System for Deploying Radioactive Sources Inside the KamLAND Detector,” T. I. Banks, S. J. Freedman, J. Wallig, N. Ybarrolaza, A. Gando, Y. Gando, H. Ikeda, K. Inoue, Y. Kishimoto, M. Koga, T. Mitsui, K. Nakamura, I. Shimizu, J. Shirai, A. Suzuki, Y. Takemoto, K. Tamae, K. Ueshima, H. Watanabe, B. D. Xu, H. Yoshida, S. Yoshida, A. Kozlov, C. Grant, G. Keefer, A. Piepke, T. Bloxham, B. K. Fujikawa, K. Han, K. Ichimura, H. Murayama, T. O'Donnell, H. M. Steiner, L. A. Winslow, D. A. Dwyer, R. D. McKeown, C. Zhang, B. E. Berger, C. E. Lane, J. Maricic, T. Miletic, M. Batygov, J. G. Learned, S. Matsuno, M. Sakai, G. A. Horton-Smith, K. E. Downum, G. Gratta, Y. Efremenko, O. Perevozchikov, H. J. Karwowski, D. M. Markoff, W. Tornow, K. M. Heeger, J. A. Detwiler, S. Enomoto, and M. P. Decowski, Nucl. Inst. Meth. A **769**, 88 (2014); arXiv:1407.0413.

29. “Studies of an array of PbF2 Cherenkov crystals with large-area SiPM readout,” A. T. Fienberg*, L. P. Alonzi, A. Anastasi, R. Bjorkquist, D. Cauz, R. Fatemi, C. Ferrari, A. Fioretti, A. Frankenthal, C. Gabbanini, L. K. Gibbons, K. Giovanetti, S. D. Goadhouse, W. P. Gohn, T. P. Gorringe, D. W. Hertzog*, M. Iacovacci, P. Kammel, J. Kaspar*, B. Kiburg, L. Li, S. Mastroianni, G. Pauletta, D. A. Peterson, D. Pocanic, M. W. Smith, D. A. Sweigart, V. Tishchenko, G. Venanzoni, T. D. Van Wechel, K. B. Wall, P. Winter, and K. Yai, Nucl. Inst. Meth. A **783**, 12 (2015); arXiv:1412.5525.†

30. “Laboratory Studies on the Removal of Radon-Born Lead from KamLAND's Organic Liquid Scintillator,” G. Keefer, C. Grant, A. Piepke, T. Ebihara, H. Ikeda, Y. Kishimoto, Y. Kibe, Y. Koseki, M. Ogawa, J. Shirai, S. Takeuchi, C. Mauger, C. Zhang, G. Schweitzer, B. E. Berger, S. Dazeley, M. P. Decowski, J. A. Detwiler, Z. Djurcic, D. A. Dwyer, Yu. Efremenko, S. Enomoto, S. J. Freedman, B. K. Fujikawa, K. Furuno, A. Gando, Y. Gando, G. Gratta, S. Hatakeyama, K. M. Heeger, L. Hsuh, K. Ichimura, K. Inoue, T. Iwamoto, and Y. Kamyshkov, Nucl. Inst. Meth. A **769**, 79 (2014); arXiv:1312.0977.

31. “Assessment of molecular effects on neutrino mass measurements from tritium beta decay,” L. I. Bodine*, D. S. Parno, and R. G. H. Robertson, Phys. Rev. C **91**, 035505 (2015); arXiv:1502.03497.†

11.2 Invited talks at conferences

1. “Beta decay: A physics garden of earthly delights,” R. G. H. Robertson, Plenary talk, APS April meeting, Savannah, GA, April 4-8, 2014.

2. “Project 8: the future of neutrino mass measurement?,” R. G. H. Robertson, Invited talk, International Symposium on Astroparticle Physics, Kingston, Ontario, May 30-31, 2014.

An * denotes a CENPA author who is the lead author of or major contributor to a publication.
A † denotes a publication describing work fully or partially supported by the DOE grant.

3. "Underground Physics: Neutrinos and Dark Matter," C. Cuesta, Invited talk, Green River Community College, Auburn, WA, March, 2015.

4. "QCD prediction of jet structure in 2D trigger-associated momentum correlations and implications for multiple parton interactions," T. A. Trainor, XLIV International Symposium on Multiparticle Dynamics, Bologna, Italy, September 8-12, 2014; arXiv:1412.0082.

5. "Muon capture experiments and possible search for light exotics," P. Kammel, Invited talk, Theoretical Perspectives on New Physics at the Intensity Frontier Workshop, Victoria, BC, September 12, 2014.

6. "Towards a Ton-Scale Neutrinoless Double-Beta Decay Experiment: Recent Progress on the MAJORANA DEMONSTRATOR," M. Buuck, Invited talk, Lake Louise Winter Institute, Lake Louise, Alberta, Canada, February 20, 2015.

7. "Tensor current limits," F. Wauters, Invited talk, Solvay Workshop on "Beta-Decay Weak Interaction Studies in the Era of the LHC," Université libre de Bruxelles, Brussels, Belgium, September 4, 2014.

8. "Direct probes of neutrino mass," R. G. H. Robertson, Plenary talk, Neutrino Oscillation Workshop, Otranto, Lecce, Italy, September 7-14, 2014; to be published in Nucl. Phys. B-Proc. Sup.; arXiv:1502.00144.

9. "Testing the Majorana Nature of the Neutrino with Germanium Detectors," J. A. Detwiler, Invited talk, 15th Annual Meeting of the Northwest Section of the American Physical Society, University of Washington, Seattle, WA, May, 2014.

10. "Simulations of HPGe Detector Arrays," Applications of Ge Detectors in Fundamental Research, J. A. Detwiler, Invited talk, Beijing, PRC, May, 2014.

11. "Testing the Majorana Nature of the Neutrino with Ge Detectors," J. A. Detwiler, Invited talk, Workshop on Germanium-Based Detectors and Technologies, Vermillion, SD, September, 2014.

12. "Precision Muon Physics," D. W. Hertzog, Invited talk, Fundamental Symmetries and Neutrinos Town Meeting, Chicago, IL, September 29, 2014.

13. "Next-Generation Muon $g-2$," D. W. Hertzog, Seminar, Ohio State University, Columbus, OH, November 6, 2014.

14. "Next-Generation Muon $g-2$," D. W. Hertzog, Colloquium, Ohio University, Athens, OH, November 7, 2014.

15. "Precision tests of Newton's inverse-square law and Einstein's equivalence principle," E. G. Adelberger, Invited colloquium speaker, Frascati National Lab, Frascati, Italy, April 21, 2014.

16. "Precision tests of Newton's inverse-square law and Einstein's equivalence principle," E. G. Adelberger, Invited colloquium speaker, University of L'Aquila, L'Aquila, Italy, April 23, 2014.

17. "Laboratory Tests of Gravity: an extremely low-energy frontier of particle physics," E. G. Adelberger, Invited Physics/Astronomy Colloquium speaker, UCLA, Los Angeles, CA, May 22, 2014.

18. "Laboratory Tests of Gravity: an extremely low-energy frontier of particle physics," E. G. Adelberger, Invited talk, Joint Meeting of the Nuclear Physics Divisions of the APS and The Physical Society of Japan, Waikoloa, HI, October 7-11, 2014.

19. "Table-top tests of Gravity," E. G. Adelberger, Invited talk, Testing Gravity 2015 Conference, Vancouver, BC, Canada, January 15-17, 2015.

20. "Status of the Fermilab $g-2$ experiment," J. Kaspar, Invited talk, The 13th International Workshop on Tau Lepton Physics (TAU2014), Aachen, Germany, September, 2014. Proceedings published in Nucl. Part. Phys. Proc. (2015); arXiv:1504.01201.

21. "Background Model for the Majorana Demonstrator," C. Cuesta, N. Abgrall, E. Aguayo, F. T. Avignone III, A. S. Barabash, F. E. Bertrand, M. Boswell, V. Brudanin, M. Busch, D. Byram, A. S. Caldwell, Y-D. Chan, C. D. Christofferson, D. C. Combs, J. A. Detwiler, P. J. Doe, Yu. Efremenko, V. Egorov, H. Ejiri, S. R. Elliott, J. E. Fast, P. Finnerty, F. M. Fraenkle, A. Galindo-Uribarri, G. K. Giovanetti, J. Goett, M. P. Green, J. Gruszko, V. E. Guiseppe, K. Gusev, A. L. Hallin, R. Hazama, A. Hegai, R. Henning, E. W. Hoppe, S. Howard, M. A. Howe, K. J. Keeter, M. F. Kidd, O. Kochetov, S. I. Konovalov, R. T. Kouzes, B. D. LaFerriere, J. Leon, L. E. Leviner, J. C. Loach, J. MacMullin, S. MacMullin, R. D. Martin, S. Meijer, S. Mertens, M. Nomachi, J. L. Orrell, C. OShaughnessy, N. R. Overman, D. G. Phillips II, A. W. P. Poon, K. Pushkin, D. C. Radford, J. Rager, K. Rielage, R. G. H. Robertson, E. Romero-Romero, M. C. Ronquest, A. G. Schubert, B. Shanks, T. Shima, M. Shirchenko, K. J. Snavely, N. Snyder, A. M. Suriano, J. Thompson, V. Timkin, W. Tornow, J. E. Trimble, R. L. Varner, S. Vasilyev, K. Vetter, K. Vorren, B. R. White, J. F. Wilkerson, C. Wiseman, W. Xu, E. Yakushev, A. R. Young, C.-H. Yu, and V. Yumatov, accepted for publication in Phys. Procedia; arXiv:1405.1370.

22. "Status of the Majorana Demonstrator," C. Cuesta, N. Abgrall, I. J. Arnquist, F. T. Avignone III, A. S. Barabash, F. E. Bertrand, V. Brudanin, M. Busch, M. Buuck, D. Byram, A. S. Caldwell, Y-D. Chan, C. D. Christofferson, J. A. Detwiler, Yu. Efremenko, H. Ejiri, S. R. Elliott, A. Galindo-Uribarri, G. K. Giovanetti, J. Goett, M. P. Greenn, J. Gruszko, I. S. Guinn, V. E. Guiseppe, R. Henning, E. W. Hoppe, S. Howard, M. A. Howe, B. R. Jasinski, K. J. Keeter, M. F. Kidd, S. I. Konovalov, R. T. Kouzes, B. D. LaFerriere, J. Leon, J. MacMullin, R. D. Martin, S. J. Meijer, S. Mertens, J. L. Orrell, C. O'Shaughnessy, N. R. Overman, A. W. P. Poon, D. C. Radford, J. Rager, K. Rielage, R. G. H. Robertson, E. Romero-Romero, C. Schmitt, B. Shanks, M. Shirchenko, N. Snyder, A. M. Suriano, D. Tedeschi, V. Timkin, J. E. Trimble, R. L. Varner, S. Vasilyev, K. Vetter, K. Vorren, B. R. White, J. F. Wilkerson, C. Wiseman, W. Xu, E. Yakushev, C.-H. Yu, V. Yumatov, submitted for publication in Nucl. Phys. B-Proc. Sup.; arXiv:1412.5682.

23. "Next generation $g-2$," J. Kaspar, Colloquium, Linfeld College, McMinnville, OR, April, 2014.

11.3 Abstracts and contributed talks

1. "KATRIN Progress Toward a Neutrino-Mass Measurement," D. S. Parno, 15th Annual Meeting of the Northwest Section of the APS, Seattle, WA, May, 2014.
2. "Project 8: Single electron spectroscopy with relativistic cyclotron radiation," M. Fertl, 20th Particle & Nuclei International Conference, Hamburg, Germany, August 25, 2014.
3. "Progress on the stationary pNMR array of the new muon $g-2$ experiment at FNAL," M. Fertl, 15th Annual Meeting of the Northwest Section of the APS, Seattle, WA, May 2, 2014.
4. "Development of a Position Sensitive Beta and Recoil Ion Detectors for the ^{6}He $\beta-\nu$ Angular Correlation Measurement," R. Hong, 4th Joint Meeting of the APS DNP and the JPS, Waikoloa, HI, October, 2014.
5. "Weak interaction studies with laser trapped ^{6}He," A. Leredde, 45th annual DAMOP meeting 2014, Madison, WI, May, 2014.
6. "Measuring $\beta-\nu$ angular correlation with laser trapped ^{6}He," A. Leredde, 4th Joint Meeting of the APS DNP and the JPS, Waikoloa Village, HI, October, 2014.
7. "Laser trapped ^{6}He atoms for beyond the Standard Model searches," A. Leredde, Midwest Cold Atom Workshop 2014, Argonne National Laboratory, Argonne, IL, November, 2014.
8. "Analysis techniques for background rejection at the Majorana Demonstrator," C. Cuesta on behalf of the Majorana Collaboration, Poster, Low Radioactivity Techniques 2015, University of Washington, Seattle, WA, March, 2015.
9. "Background analysis and status of the ANAIS dark matter project," C. Cuesta, Contributed talk, Low Radioactivity Techniques 2015, University of Washington, Seattle, WA, March, 2015.
10. "Studying neutrinos with the Majorana Demonstrator," C. Cuesta on behalf of the Majorana Collaboration, Contributed talk, UWPA Research Symposium, University of Washington, Seattle, WA, November, 2014.
11. "Status of the Majorana Demonstrator," C. Cuesta on behalf of the Majorana Collaboration, Contributed talk, Neutrino Oscillation Workshop, Otranto, Italy, September, 2014.
12. "SiPMs for solar neutrino detector," J. Kaspar, Contributed talk, Solar Neutrinos at JinPing workshop, Lawrence Berkeley National Laboratory, Berkeley, CA, June, 2014.

13. "The MAJORANA DEMONSTRATOR status and prospects," C. Cuesta on behalf of the MAJORANA Collaboration, Contributed talk, 15th Annual Meeting of the Northwest Section of the American Physical Society, University of Washington, Seattle, WA, May, 2014.

14. "A Single-Site Pulse-Basis Technique for Multi-Site Event Tagging with the MAJORANA DEMONSTRATOR," M. Buuck, Poster presentation, Low Radioactivity Techniques 2015, University of Washington, Seattle, WA, March 18, 2015.

15. "Pulse Shape Analysis Studies for the MAJORANA DEMONSTRATOR," C. Cuesta on behalf of the MAJORANA Collaboration, Poster, XXVI Conference on Neutrino Physics and Astrophysics (Neutrino 2014), Boston, MA, June, 2014.

11.4 Papers submitted or to be published

1. "Single electron detection and spectroscopy via relativistic cyclotron radiation," D. M. Asner, R. F. Bradley, L. de Viveiros, P. J. Doe, J. L. Fernandes, M. Fertl*, E. C. Finn, J. A. Formaggio, D. Furse, A. M. Jones, J. N. Kofron*, B. H. LaRoque, M. Leber, E. L. McBride, M. L. Miller, P. Mohanmurthy, B. Monreal, N. S. Oblath, R. G. H. Robertson*, L. J Rosenberg, G. Rybka*, D. Rysewyk, M. G. Sternberg, J. R. Tedeschi, T. Thmmler, B. A. VanDevender, and N. L. Woods, accepted by Phys. Rev. Lett.; arXiv:1408.5362.†

2. "A device for simultaneous spin analysis of ultracold neutrons," S. Afach, G. Ban, G. Bison, K. Bodek, Z. Chowdhuri, M. Daum, M. Fertl, B. Franke, P. Geltenbort, Z. D. Grujić, L. Hayen, V. Hélaine, R. Henneck, M. Kasprzak, Y. Kermaïdic, K. Kirch, S. Komposch, A. Kozela, J. Krempel, B. Lauss, T. Lefort, Y. Lemière, A. Mtchedlishvili, O. Naviliat-Cuncic, F. M. Piegsa, G. Pignol, P. N. Prashanth, G. Quéméner, M. Rawlik, D. Ries, D. Rebreyend, S. Roccia, D. Rozpedzik, P. Schmidt-Wellenburg, N. Severijns, A. Weis, E. Wursten, G. Wyszynski, J. Zejma, and G. Zsigmond; arXiv:1502.06876.

3. "Constraining interactions mediated by axion-like particles with ultracold neutrons," S. Afach, G. Ban, G. Bison, K. Bodek, M. Burghoff, M. Daum, M. Fertl, B. Franke, Z. D. Grujić, V. Hélaine, M. Kasprzak, Y. Kermaïdic, K. Kirch, P. Knowles, H.-C. Koch, S. Komposch, A. Kozela, J. Krempel, B. Lauss, T. Lefort, Y. Lemière, A. Mtchedlishvili, O. Naviliat-Cuncic, F. M. Piegsa, G. Pignol, P. N. Prashanth, G. Quéméner, D. Rebreyend, D. Ries, S. Roccia, P. Schmidt-Wellenburg, A. Schnabel, N. Severijns, J. Voigt, A. Weis, G. Wyszynski, J. Zejma, J. Zenner, and G. Zsigmond; submitted to Phys. Lett. B; arXiv:1412.3679.

4. "Event-wise mean-pt fluctuations vs minimum-bias jets (minijets) at the LHC," T. A. Trainor; submitted to Phys. Rev. C; arXiv:1503.02197.†

An * denotes a CENPA author who is the lead author of or major contributor to a publication.
A † denotes a publication describing work fully or partially supported by the DOE grant.

5. "Optimal modeling of 1D azimuth correlations in the context of Bayesian inference," M. B. De Kock, H. C. Eggers and T. A. Trainor*; submitted to Phys. Rev. C; arXiv:1502.04475.†

6. "Predicting minimum-bias trigger-associated dijet correlations in p-p collisions," T. A. Trainor; submitted to J. Phys. G.; arXiv:1407.6422.†

7. "Neutron spectrometry with scintillating bolometers of LiF and sapphire," N. Coron, C. Cuesta, E. García, C. Ginestra, J. Gironnet, P. de Marcillac, M. Martínez, Y. Ortigoza, A. Ortiz de Solórzano, J. Puimedón, T. Redon, T. Rolón, M. L. Sarsa, L. Torres, and J. A. Villar, submitted for publication in IEEE.

8. "Study of electron anti-neutrinos associated with gamma-ray bursts using KamLAND," K. Asakura, A. Gando, Y. Gando, T. Hachiya, S. Hayashida, H. Ikeda, K. Inoue, K. Ishidoshiro, T. Ishikawa, S. Ishio, M. Koga, S. Matsuda, T. Mitsui, D. Motoki, K. Nakamura, S. Obara, Y. Oki, T. Oura, I. Shimizu, Y. Shirahata, J. Shirai, A. Suzuki, H. Tachibana, K. Tamae, K. Ueshima, H. Watanabe, B. D. Xu, H. Yoshida, A. Kozlov, Y. Takemoto, S. Yoshida, K. Fushimi, A. Piepke, T. I. Banks, B. E. Berger, T. O'Donnell, B. K. Fujikawa, J. Maricic, J. G. Learned, M. Sakai, L. A. Winslow, Yu. Efremenko, H. J. Karwowski, D. M. Markoff, W. Tornow, J. A. Detwiler, S. Enomoto, and M. P. Decowski, submitted to Astrophys. J; arXiv:1503.02137 [astro-ph] (2015).

9. "7Be Solar Neutrino Measurement with KamLAND," A. Gando, Y. Gando, H. Hanakago, H. Ikeda, K. Inoue, K. Ishidoshiro, H. Ishikawa, Y. Kishimoto, M. Koga, R. Matsuda, S. Matsuda, T. Mitsui, D. Motoki, K. Nakajima, K. Nakamura, A. Obata, A. Oki, Y. Oki, M. Otani, I. Shimizu, J. Shirai, A. Suzuki, K. Tamae, K. Ueshima, H. Watanabe, B. D. Xu, S. Yamada, Y. Yamauchi, H. Yoshida, A. Kozlov, Y. Takemoto, S. Yoshida, C. Grant, G. Keefer, D. W. McKee, A. Piepke, T. I. Banks, T. Bloxham, S. J. Freedman, B. K. Fujikawa, K. Han, L. Hsu, K. Ichimura, H. Murayama, T. O'Donnell, H. M. Steiner, L. A. Winslow, D. Dwyer, C. Mauger, R. D. McKeown, C. Zhang, B. E. Berger, C. E. Lane, J. Maricic, T. Miletic, J. G. Learned, M. Sakai, G. A. Horton-Smith, A. Tang, K. E. Downum, K. Tolich, Yu. Efremenko, Y. Kamyshkov, O. Perevozchikov, H. J. Karwowski, D. M. Markoff, W. Tornow, J. A. Detwiler, S. Enomoto, K. Heeger, and M. P. Decowski, submitted to Phys. Rev. C; arXiv:1405.6190 [hep-ex] (2014).

10. "Low-Energy Precision Tests of the Standard Model: A Snapshot," D. W. Hertzog*, Invited Review for Special Issue: "Particle Physics after the Higgs," Annalen der Physik (2015).†

11. "Transverse-rapidity $\mathbf{y_t}$ dependence of the nonjet azimuth quadrupole from 62 and 200 GeV Au-Au collisions," D. T. Kettler, D. J. Prindle, and T. A. Trainor*; submitted to Phys. Rev. C; arXiv:1504.02741.†

An * denotes a CENPA author who is the lead author of or major contributor to a publication.
A † denotes a publication describing work fully or partially supported by the DOE grant.

12. “Precision Muon Physics,” T. P. Gorringe and D. W. Hertzog*, Invited Review for Prog. Part. Nucl. Phys. (2015).†

13. “Measurement of the Formation Rate of Muonic Hydrogen Molecules,” V. A. Andreev, T. I. Banks, R. M. Carey, T. A. Case, S. M. Clayton, K. M. Crowe, J. Deutsch, J. Egger, S. J. Freedman, V. A. Ganzha, T. Gorringe, F. E. Gray, D. W. Hertzog, M. Hildebrandt, P. Kammel*, B. Kiburg, S. Knaack*, P. A. Kravtsov, A. G. Krivshich, B. Lauss, K. R. Lynch, E. M. Maev, O. E. Maev, F. Mulhauser, C. Petitjean, G. E. Petrov, R. Prieels, G. N. Schapkin, G. G. Semenchuk, M. A. Soroka, V. Tishchenko, A. A. Vasilyev, A. A. Vorobyov, M. E. Vznuzdaev, and P. Winter, accepted for publication in Phys. Rev. C; arXiv:1502.00913.†

11.5 Reports and white papers

1. “Muon (g-2) Technical Design Report,” J. Grange, V. Guarino, P. Winter, K. Wood, H. Zhao, R. M. Carey, D. Gastler, E. Hazen, N. Kinnaird, J. P. Miller, J. Mott, B. L. Roberts, J. Benante, J. Crnkovic, W. M. Morse, H. Sayed, V. Tishchenko, V. P. Druzhinin, B. I. Khazin, I. A. Koop, I. Logashenko, Y. M. Shatunov, E. Solodov, M. Korostelev, D. Newton, A. Wolski, R. Bjorkquist, N. Eggert, A. Frankenthal, L. Gibbons, S. Kim, A. Mikhailichenko, Y. Orlov, D. Rubin, D. Sweigart, D. Allspach, G. Annala, E. Barzi, K. Bourland, G. Brown, B. C. K. Casey, S. Chappa, M. E. Convery, B. Drendel, H. Friedsam, T. Gadfort, K. Hardin, S. Hawke, S. Hayes, W. Jaskierny, C. Johnstone, J. Johnstone, V. Kashikhin, C. Kendziora, B. Kiburg, A. Klebaner, I. Kourbanis, J. Kyle, N. Larson, A. Leveling, A. L. Lyon, D. Markley, D. McArthur, K. W. Merritt, N. Mokhov, J. P. Morgan, H. Nguyen, J-F. Ostiguy, A. Para, C. C. Polly M. Popovic, E. Ramberg, M. Rominsky, D. Schoo, R. Schultz, D. Still, A. K. Soha, S. Strigonov, G. Tassotto, D. Turrioni, E. Villegas, E. Voirin, G. Velev, D. Wolff, C. Worel, J-Y. Wu, R. Zifko, K. Jungmann, C. J. G. Onderwater, P. T. Debevec, S. Ganguly, M. Kasten, S. Leo, K. Pitts, C. Schlesier, M. Gaisser, S. Haciomeroglu, Y-I. Kim, S. Lee, M-J Lee, Y. K. Semertzidis, K. Giovanetti, V. A. Baranov, V. N. Duginov, N. V. Khomutov, V. A. Krylov, N. A. Kuchinskiy, V. P. Volnykh, C. Crawford, R. Fatemi, W. P. Gohn, T. P. Gorringe, W. Korsch, B. Plaster, A. Anastasi, D. Babusci, S. Dabagov, C. Ferrari, A. Fioretti, C. Gabbanini, D. Hampai, A. Palladino, G. Venanzoni, T. Bowcock, J. Carroll, B. King, S. Maxfield, K. McCormick, A. Smith, T. Teubner, M. Whitley, M. Wormald, R. Chislett, S. Kilani, M. Lancaster, E. Motuk, T. Stuttard, M. Warren, D. Flay, D. Kawall, Z. Meadows, T. Chupp, R. Raymond, A. Tewlsey-Booth, M. J. Syphers, D. Tarazona, C. Ankenbrandt, M. A. Cummings, R. P. Johnson, C. Yoshikawa, S. Catalonotti, R. Di Stefano, M. Iacovacci, S. Mastroianni, S. Chattopadhyay, M. Eads, M. Fortner, D. Hedin, N. Pohlman, A. de Gouvea, H. Schellman, L. Welty-Rieger, T. Itahashi, Y. Kuno, K. Yai, F. Azfar, S. Henry, G. D. Alkhazov, V. L. Golovtsov, P. V. Neustroev, L. N. Uvarov, A. A. Vasilyev, A. A. Vorobyov, M. B. Zhalov,

An * denotes a CENPA author who is the lead author of or major contributor to a publication.
A † denotes a publication describing work fully or partially supported by the DOE grant.

L. Cerrito, F. Gray, G. Di Sciascio, D. Moricciani, C. Fu, X. Ji, L. Li, H. Yang, D. Stöckinger, G. Cantatore, D. Cauz, M. Karuza, G. Pauletta, L. Santi, S. Baesler, M. Bychkov, E. Frlez, D. Pocanic, L. P. Alonzi*, M. Fertl, A. Fienberg, N. Froemming, A. Garcia*, D. W. Hertzog*, J. Kaspar*, P. Kammel, R. Osofsky, M. Smith, E. Swanson*, T. van Wechel, and K. Lynch; White paper; arXiv:1501.06858 (2015).†

2. "Fundamental symmetries, neutrinos, neutrons, and astrophysics: a White Paper on progress and prospects," A. Aprahamian, F. Cavanna, V. Cianciolo, V. Cirigliano, A. de Gôuvéa, D. J. Dean, J. A. Detwiler*, T. DeYoung, J. Engel, J. Erler, B. W. Filippone, N. Fomin, J. A. Formaggio, G. Fuller, D. Geesaman, W. C. Haxton, A. Hayes, D. W. Hertzog*, P. Huber, T. M. Ito, J. R. Klein, Yu. G. Kolomensky, K. S. Kumar, C. Y. Liu, J. C. Long, R. G. Milner, J. G. Morfín, U. Mosel, G. D. Orebi Gann, J. L. Orrell, A. Piepke, B. Plaster, A. Pocar, A. W. P. Poon, D. C. Radford, M. J. Ramsey-Musolf, D. G. Richards, A. Ritz, R. G. H. Robertson*, K. Scholberg, S. J. Seestrom, W. M. Snow, J. Singh, M. Thoennessen, S. E. Vigdor, D. L. Wark, J. F. Wilkerson, J. Wuertele, and A. Young; White paper on Fundamental Symmetries and Neutrinos in preparation for 2015 Nuclear Physics Long Range Plan.

3. "Muon g-2 storage ring starts a new life," D. W. Hertzog* and B. L. Roberts, CERN Courier, **54**, 9 (2014).†

11.6 Ph.D. degrees granted

A novel method for electron energy measurement: Cyclotron Radiation Emission Spectroscopy, Jared N. Kofron (March, 2015).†

An improved low-temperature RF-cavity search for dark-matter axions, Dmitry Lyapustin (March, 2015).

Rotating Torsion Balance Tests of the Weak Equivalence Principle, Todd A. Wagner (December, 2014).

An * denotes a CENPA author who is the lead author of or major contributor to a publication.
A † denotes a publication describing work fully or partially supported by the DOE grant.

FRONT ROW (L to R): Ana Malagon, Laura Bodine, Jens Gundlach, Christian Boutan, Brett Hamre, Alejandro García, Rachel Osofsky, Hannah LeTourneau, Yelena Bagdasarova, Nathan Froemming, Arnaud LeRedde, Martin Fertl

ROW TWO (L to R): Erik Shaw, Hans Bichsel, Peter Kammel, Charlie Hagedorn, Nomie Torres, John Cramer, Hamish Robertson, David Hertzog, John Amsbaugh, John Lee, Doug Will, Krishna Venkateswara, Eric Smith, Dmitry Lyapustin

STANDING (L to R): Julieta Gruszko, Richard Ottens, Cliff Plesha, Jonathan Leon, Gray Rybka, Will Terrano, Nicole Crisosto, Jim Sloan, Jim Elms, Ronaldo Ortez, Ran Hong, Erik Swanson, David Hyde, Gary Holman, Matthias Smith, David Peterson, Jarek Kaspar, Tim Van Wechel, Duncan Prindle, Cole Helling, Ian Guinn, Rachel Ryan, Frederik Wauters, Aaron Fienberg, Svenja Fleischer, Clara Cuesta, Matt Sternberg, Kim-Siang Khaw, Victoria Clarkson, Samuel Sexton, Derek Storm, Luke Kippenbrock